LABORATORY ANALYSES OF THE EFFECT OF THE PRE-EXISTING NOTCH ON THE DIRECTION OF SECONDARY CRACK PROPAGATION IN COASTAL SLOPES

by

Yunmo Zhao

B.S., Southwest Jiaotong University, 2016

Submitted to the Graduate Faculty of

Swanson School of Engineering in partial fulfillment

of the requirements for the degree of

Master of Science

University of Pittsburgh

2017

UNIVERSITY OF PITTSBURGH

SWANSON SCHOOL OF ENGINEERING

This thesis was presented

by

Yunmo Zhao

It was defended on

November 21, 2017

and approved by

Anthony T. Iannacchione, Ph.D., Associate Professor,

Departmental of Civil and Environmental Engineering

Calixto I.Garcia, Ph.D., Professor,

Departmental of Mechanical Engineering and Materials Science

Luis E. Vallejo, Ph.D., Professor,

Departmental of Civil and Environmental Engineering

Thesis Advisor: Luis E. Vallejo, Ph.D., Professor,

Departmental of Civil and Environmental Engineering

LABORATORY ANALYSES OF THE EFFECT OF THE PRE-EXISTING NOTCH ON THE DIRECTION OF SECONDARY CRACK PROPAGATION IN COASTAL SLOPES

Yunmo Zhao, M.S.

University of Pittsburgh, 2017

This research, carried out as series of laboratory experiments on prismatic clay samples, addresses the question of how different shape of openings and different angles of the initial notch in a simulated slope affect propagation of secondary cracks. The research resulted in the introduction of a novel experimental approach. To study the secondary crack propagation, experiments were performed on clay samples of two types: prismatic clay samples with openings of different shape and semi-prismatic clay samples with pre-existing notches with different open angles. These tests were used to simulate, respectively, underground tunnels and the damage zone around these openings and the development of secondary crack propagation from the notch in coastal slopes. The Mohr-coulomb failure criterion and Linear Elastic Fracture Mechanics (LEFM) were applied to understand the failure process of these clay samples undergoing uniaxial compression and direct shear. The result of the first part of the experiment, plus the use of LEFM theory, illustrated how the shape of the opening affects the maximum stress around the openings and the crack propagation in the damage zone. Furthermore, in order to predict the direction of the secondary crack propagation in notch samples, the laboratory experiments and theory derived from LEFM were used to study the propagation mechanism of toe notches in coastal slopes and their behavior. This

propagation mechanism of the notches in the slopes was predicted very well by the use of LEFM theory, therefore showing the usefulness of LEFM theory in solving geotechnical engineering problems.

TABLE OF CONTENTS

LIST OF TABLES

LIST OF FIGURES

PREFACE

I am so grateful to Professor Luis E. Vallejo for providing me a great opportunity to complete this research, his patience and wise suggestion really helps me finishing this experiment and also give me inspiration for the future career. Also, I would like to thank the other members of my MS committee, Dr. Calixto Grcia and Dr. Anthony Iannacchione.

I would like to thank my parents, sister and brother-in-law for supporting me study in University of Pittsburgh for almost two years.

1.0 INTRODUCTION

Approximately 50% of the world's population lives within 60 km of a coastal area, which provides it with both living space and required resources [1]. However, coastal erosion and coastal instability will threaten human's living space and environment. With such dramatic change underway, it is now necessary to understand the changes and processes that contribute such dramatic geological transformation in order to better manage engineering interventions that could minimize its negative effects [2]. One of the main types of coastal erosion is bluff erosion, which has been extensively researched by many academics. Collin and Sitar [3], for example, studied for five years the process by which bluffs composed of weakly lithified sediment underwent continuous erosion. They found that the failure caused by wave cation was difficult to observe and that the failure mechanisms changed depending on the different material strength of the bluffs. Río and Gracia [4] build a numerical model to evaluate the erosion of coastal bluffs on temperate coasts, understood as the potentially damaging consequences resulting from the cliff recession processes. Brooks and Boreham [5] similarly investigated the thresholds and mechanisms for retreat in soft rock cliffs in coastal areas. These researchers focused on this environment and type of erosion because of the huge loss to humans that clay bluff erosion can cause. Castedo, Murphy, Lawrence and Paredes [2] suggested that in order to explore the social and economic implications of land loss and the cliff erosion mechanisms, it is essential to first understand the erosion

processes involved, especially in cases where the shoreline responds in a non-linear fashion to the force due to variations in the local geology.

Clay bluff erosion and recession is caused by wave erosion at the toe of the bluff, on the lake, ashore or sea bottom. Toe erosion may trigger a different type of landslides [6]. The two types of failures that may be caused are shown in Fig.1.1

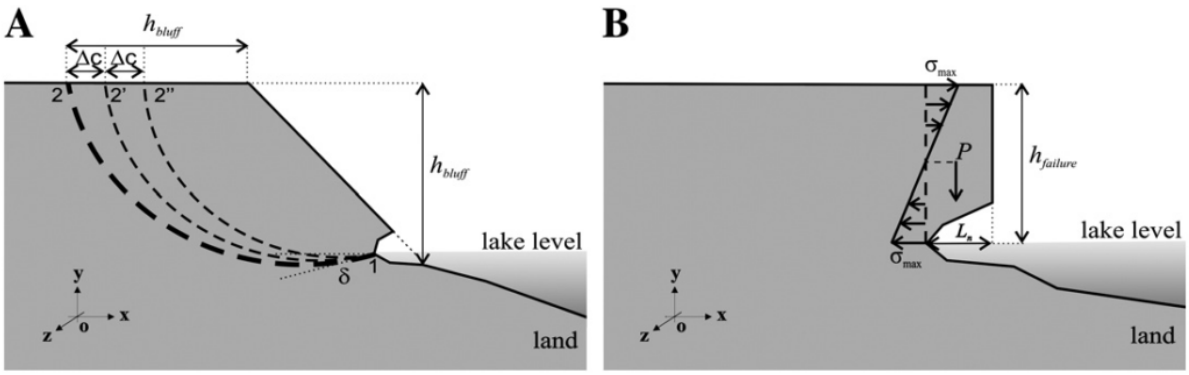

Figure 1.1. (a) circular failure (b) toe failure [6]

This study investigates toe failure of coastal slopes caused directly by wave action. In one type of toe failure, the lateral and vertical load induced by the earth pressure results in tensile failure in the slope, as shown in Fig.1.2. When the wave hits the face of the bluff, the normal and shear forces act on the toe region of the slope. As shown in Fig. 1.3, material from the slope is removed from the toe of the bluff by the wave action during this process. Of special importance is the fact that the initial angle of the notch affects the direction of the secondary crack propagation. Meanwhile, considering the difference between the nature earth pressure and the pressure applied in laboratory conditions for the loading history, we assume that the vertical earth pressure is constant since the normal stress, which is the same as the shear stress caused by gravity of the earth above the crack, will not change generally. Hence, the ratio of the shear and normal stress

induced by the earth's pressure would also be different in natural conditions. This study also investigates how variation in the ratio of normal to shear stress influences secondary crack propagation

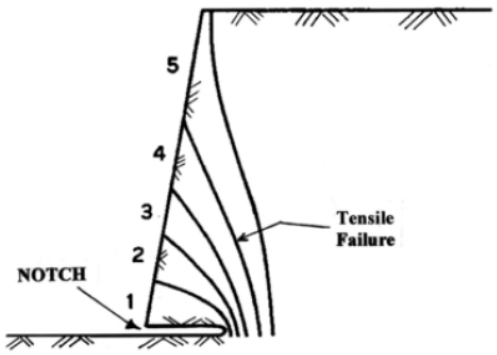

Figure 1.2 Progression of toe failures from an open toe notch [7]

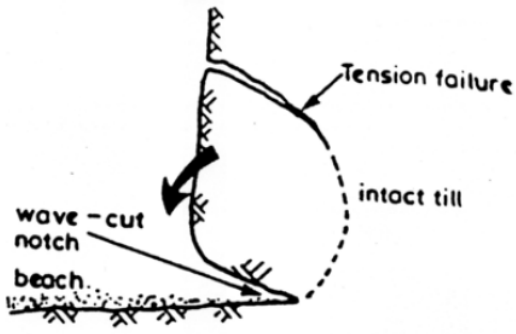

Figure 1.3 A wave induced notch and a notch induced failure in a coastal slope [8][9]

The problem of slope failure has been discussed widely. Some researchers use numerical analysis methods to investigate this problem. For example, Arnaldo, Camones, Vargas, Peluci, Figueiredo and Quadros [10] used Distinct Element Method (DEM) to analyze the process of crack propagation in slopes through modeling the failure of contact bonds between materials. Similarly, Jiang, Jiang, Crosta, Shi, Chen and Zhang [11] investigated the failure process and mechanisms of

jointed rock slopes by using the Distinct Element Method (DEM) and take an amount of numerical direct shear tests to help better understand the theory on both the macroscopic and microscopic levels. Also, Gu and Huang [12] used DEM to create a complex rock topple-rock slide failure mode to explain the failure mechanism of a landslide caused by toe failure. The Distinct Element Method (DEM) seems like the most popular tool for numerical analysis, but methods like the Finite Element Method (FEM) and other self-designed methods can still be applied successfully to study slope problems. For example, Li, Tang, Zhu, and Liang [13] created a micromechanical method that they called the Gravity Increase Method to study the process of crack propagation--using the Finite Element Method (FEM) as a basic stress analysis tool and elastic damage mechanics as their basic theory. Zhang, Cao and Meng [14] used the commercial software FLAC to numerically investigate the progressive failure of a jointed rock slope based on fracture mechanics and the strength reduction method (SRM). Finally, Ke, Kuo, Hsu, Liu and Chen [15] created, and applied, a numerical analysis method called the Single-domain Boundary Element Method to simulate the crack propagation path in two-dimensional cracked anisotropic materials. Some researchers have studied real-world slope cases. For example, a landslide that occurred in 1986 in at Senise (southern Italy) was interpreted using the Mohr–Coulomb plastic law and strain-softening behavior of the materials, proving that progressive failure had occurred due to deep openings carried out earlier at the toe of the slope [16].

However, the use of numerical analysis also has some shortcomings limits. For example, the numerical solution for the Finite Element Method (FEM) has a strong mesh dependence. This means that even for the same model, calculations will produce different results if the structure of the grid changes or if the type of cell is not selected properly, or if the cell shape is not good, the calculation results may be inaccurate. There are also problems with the Infinite Element Method.

It has a high parameter sensitivity, which means that the particular parameters selected strongly affect the results. Therefore, the results are sometimes highly random. Addressing this point, Mohr [16] proved that numerical procedures currently used are very often affected by a lack of convergence, and that the solution may depend strongly on the mesh adopted. In addition to these concerns, given the uncertainty of soil, numerical analysis will inevitably contain flaws.

Now we will focus on laboratory analysis methods used to explore the slope problem. Li, Peng, Zhang, and Qiu created a new experimental system to investigate the fracture process of sandstone specimens containing a pre-cut hole under coupled static and dynamic loads, and combined their results with fracture mechanism to explain this phenomenon [17]. The secondary crack propagation developed from the crack tip in soil when subjecting to a mixed-mode (Mode I and Mode II) type of loading by doing laboratory analysis was investigated [18]. The laboratory results provided by Vallejo [19] explained the result of secondary crack propagation in a clay sample with a pre-existing notch of 0°. Building on Vallejo's results, this research will improve the geotechnical knowledge of how secondary cracks would develop in the clay samples in which the pre-existing notch had different angles. A series of tests and theory were proposed to explore this question of how, in a clay sample, the initial angle of a pre-existing notch would affect the secondary crack propagation.

Also discussed in this paper is the question of how a crack propagates around a tunnel. Some researchers have investigated related problems such as the implications of including a damage zone around a circular opening. To investigate the implications of tunneling on secondary crack propagation, hybrid finite-discrete element (FDEM) analysis was used to understand the deformation and failure of the excavation damaged zone (EDZ)--located around the tunnel [20]. The damage zone around a circular opening is influenced by strong mechanical anisotropy induced

by the structure of the layered material. Consequently, a numerical approach based on principles of non-linear fracture mechanics and DEM was applied to investigate the process of failure process and the influence of in situ stress on resulting EDZ geometry [21]. Related laboratory experiments of hollow cylinders were performed to study how to reduce the excavation damaged zone (EDZ) around tunnels [22]. All of these researches focus on crack propagation around circular opening. This paper continues studying this research by specifically addressing how the shape of opening affects the crack propagation and then investigating this question with a series laboratory tests.

2.0 LABORATORY PROGRAM AND TESTING

2.1 PRISMATIC SAMPLES WITH OPENINGS OF DIFFERENT SHAPES

2.1.1 Materials used

The clay used in this experiment was Kaolinite clay obtained from China. The clay was soft, light tan in color, and was pliable enough to be shaped easily when wet. Kaolinite clay has a low shrink–swell capacity, and this type was choosen mainly because it is a very homogeneous material. This homogeneity was an outstanding advantage in the current laboratory research since it enabled crack propagation to be studied in samples without the adverse effect of heterogeneities [19]. The Kaolinite clay used had a LL=58%, a PL=28% and a G_s=2.65.

2.1.2 Equipment used

Transparent glass boxes were created in order to form clay cubes of two different sizes for the compressing and shearing tests. The dimensions of the inside of the boxes (the size of the resulting cubes) were 7.62◊7.62◊2.54 cm and 12.7◊10.16◊2.54 cm, respectively. The boxes are shown in Fig.2.1, below. The silce glass in bottom is detachable, so when the clay sample is fixed well, it can be moved out from the box easily.

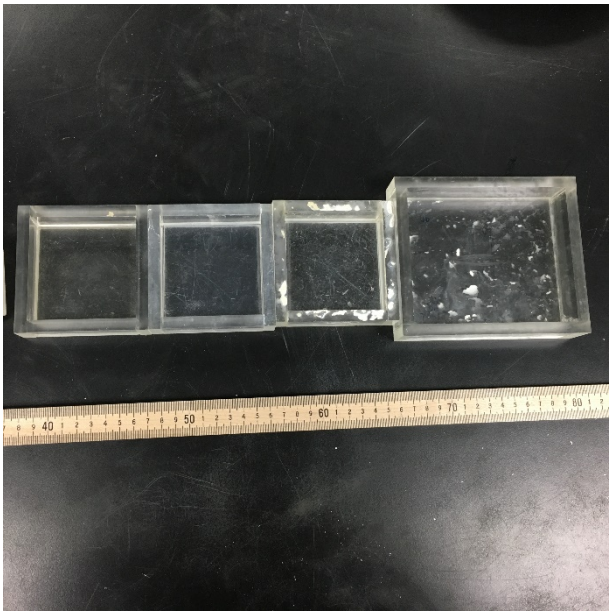

Figure 2.1 Designed boxes

Special bits were used to create openings of various shapes in the clay cubes. These bits are shown in Fig.2.2. When the sharp end of each bit was drilled into the clay cube, a hole of the corresponding shape was formed. Then, the handle shown on the far right of the figure was used to remove the bit.

Figure 2.2 Special bits

The testing system consisted of 4 components: a compressive stress loading device, a compressive and shearing stress loading device, a displacement meter, and a pressure gauge. Fig.2.3 below shows the compressive stress loading device, comprised of a rigid frame, a rigid indenter, a rocker arm, two glass blocks, an displacement meter, and an pressure gauge. The rocker arm is for slowly adding the load, which increased the pressure. The two glass blocks on the top and bottom of the prismatic clay sample created a constant degree of pressure and were placed in the center of the rigid indenter to ensure accurate analysis of the force. Fig.2.4 shows the compressive and shearing stress loading device, which was comprised of two square steel frames, rocker arms for adding vertical and horizontal pressure, two glass blocks, a vertical pressure gauge, a horizontal pressure guage, and a horizontal displacement meter.

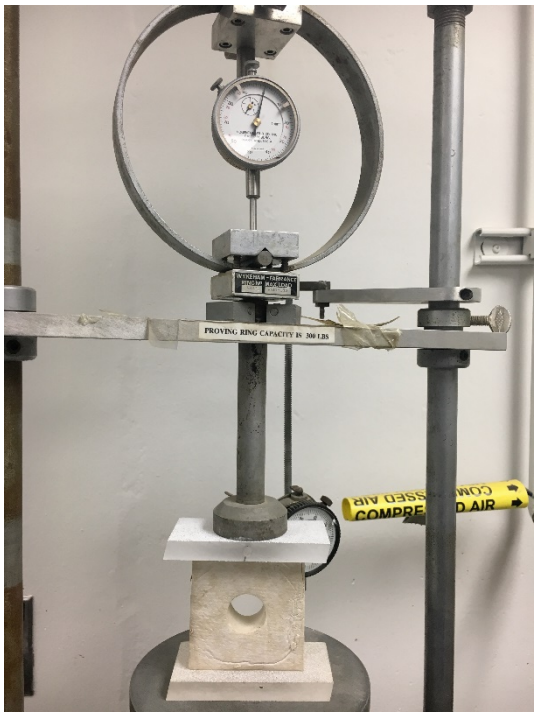

Figure 2.3 Compressive stress loading device

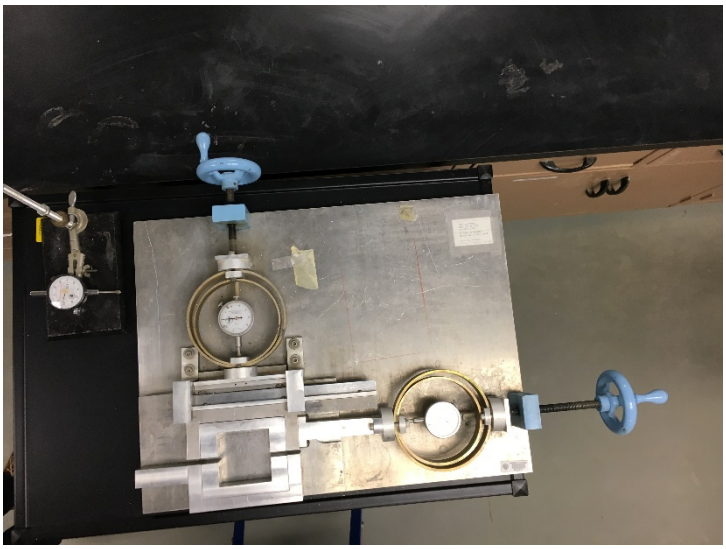

Figure 2.4 Compressive and shearing stress loading device

2.1.3 Preparation of samples

First, the clay was placed into a used laboratory metallic contaniner, and mixed by hand with distilled water at room temperature for about twenty minutes until the texture was nearly uniform. Then this viscous clay was carefully placed into the designed boxes, which were completely filled to create prismatic clay samples with the dimensions specified above. Once the boxes were completely full, the top surface of the cube was modified by a sharp knife. Then compressive force was applied by steel blocks that was placed on the top of the box to fix the shape and allow the cube to drain.

Once formed, the samples were allowed to dry in the laboratory for 24 hours, and then a flat-bottomed hole 25.4 mm deep was dug vertically with special bits on these samples after removing the sample out of bits, then another two days of drying allows the samples to solid

completely. Fig.2.5, below, shows the different shapes of the holes cut into the prismatic clay samples uesd in this study. Table 1, which follows this figure, lists the size of each of the openings.

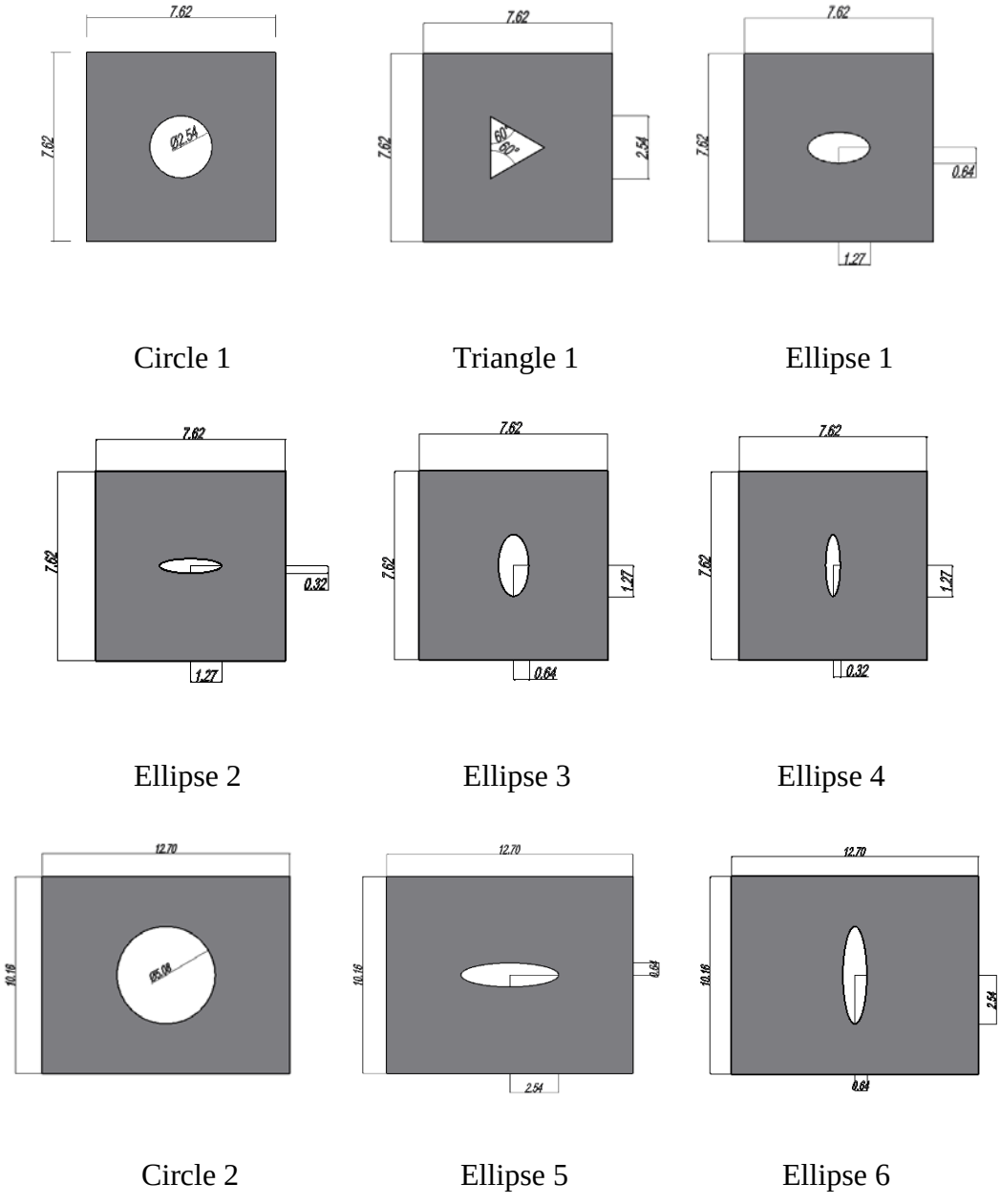

Figure 2.5 Shape of openings

Table 2.1 Shape and size of openings

Shape		H/W	Size(cm)	
Circle			Diameter,D	
	Circle 1	1	2.54	
	Circle 2	1	5.08	
Triangle			Length,L	
	Triangle 1	-	2.54	
Ellipse			Major axis,a	Minor axis,b
	Ellipse 1	0.5	1.27	0.635
	Ellipse 2	0.25	1.27	0.318
	Ellipse 3	2	1.27	0.635
	Ellipse 4	4	1.27	0.318
	Ellipse 5	0.25	2.54	0.635
	Ellipse 6	4	2.54	0.635

The samples with different shape openings represent the model various shapes of tunnels, and in this experiment, analogous to underground stresses that tunnels commonly experience. In order to be able to compare and analyze the greatest number of situations possible, the cubes were grouped into 5 different combinations. one of which is shown in Fig.2.6.

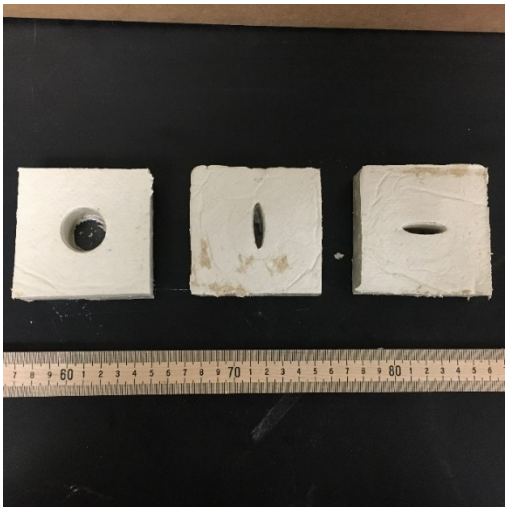

Figure 2.6 One group of clay cubes

2.1.4 Testing

2.1.4.1 Testing under compression

In the first compressive experiment, shown in Fig.2.7 below, the sample was put into the compressive loading device and the two glass blocks were placed on the top and bottom, respectively. Next, two persons standing in front and beside the sample, respectively, positioned the sample to confirm that it was directly in front of the middle of the rigid indenter. Next, the rocker arm was slowly rotated until the indenter almost came in contact with the glass block. Then, the displacement meter and pressure gauge were calibrated, and the test began, with the pressure on the sample being increased manually by the rocker arm. To guarantee the precision of the results, pressure was increased as slowly as possible. The values of the displacement meter and pressure gauge were recorded every ten scales of the dial plate until a final crack developed through the opening of the sample. This crack signaled the failure of the sample and, once it appeared, the test was over. Finally, the values from the displacement meter and pressure gauge were transformed into standard form for later analysis of results.

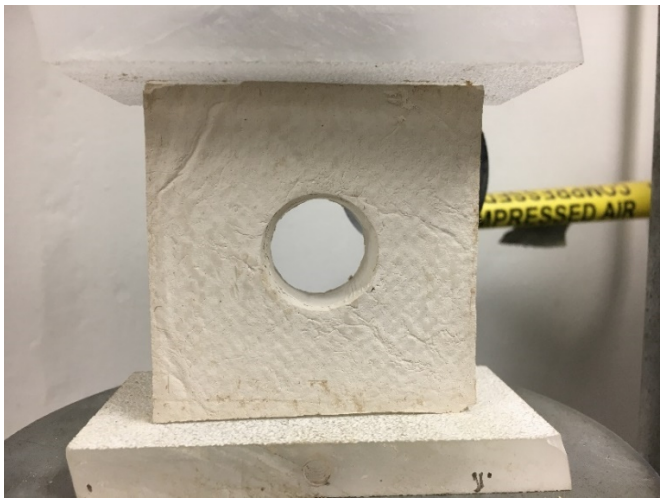

Figure 2.7 The first sample of compressive experiment

Other analogous experiments completed using the same process are shown in Fig.2.8.

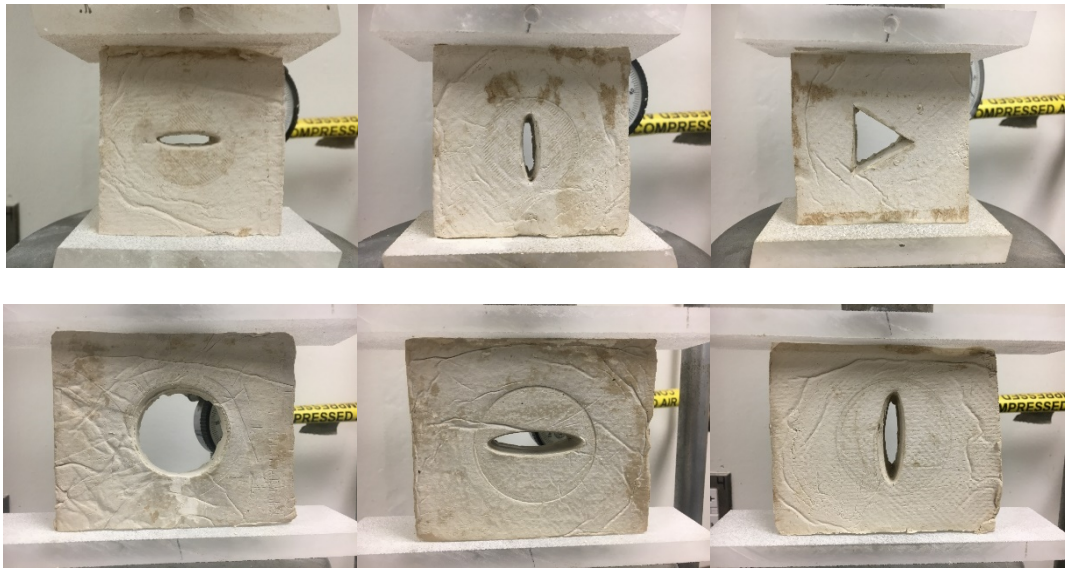

Figure 2.8 Other samples of compressive experiment

2.1.4.2 Testing under direct shear

In the first direct shear experiment the sample was placed in the compressive and shearing stress loading device. This sample can be seen in Fig.2.9. Once the sample was fit into the steel frame, its position was adjusted to confirm that it was touching the top and bottom sides of the frame and was nearly in contact with the right side of the frame. During this test, the desired compressive pressure was first applied on the top of the specimen, and then the lateral shear force was added. During the test, to ensure the pressure applied on the top of specimen was constant, one person was holding and regulating the rocker arm through the test. The values of the displacement meter and pressure gauge were recorded every ten scales of the dial plate during the process until a final crack occurred through the opening of the sample. As with the shear experiments, this crack signaled the failure of the sample, and, once it appeared, the test was over. Finally, the values from

the displacement meter and pressure gauge were transformed into standard form for later analysis of results.

Other analogous experiments done using the same process are shown in Fig.2.10.

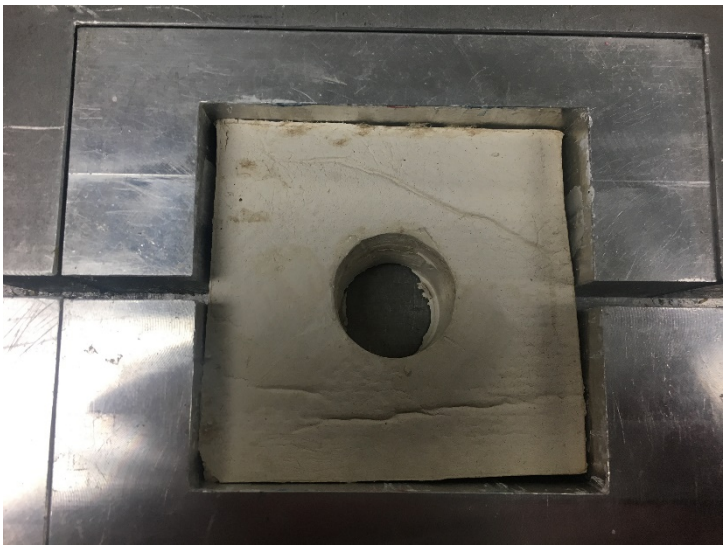

Figure 2.9 The first sample of compressive and shearing experiment

Figure 2.10 Other samples of compressive and shearing experiment

2.2 SAMPLES SIMULATING VERTICAL SLOPES WITH A NOTCH

2.2.1 Material used

The material used in this part is still Kaolinite clay, the property and advantage of the clay is mentioned in the last section.

2.2.2 Equipment used

Transparent glass boxes were used in order to form clay cubes in dimensions of the inside of the boxes (the size of the resulting cubes) of 7.62◊7.62◊2.54 cm, the boxes are shown in Fig.2.1.

Special bits were used to create openings and notches of various shapes in the clay cubes. These bits are shown in Fig.2.11. When the sharp end of each bit was drilled into the clay cube, a hole of the corresponding shape was formed. Then, the handle shown on the far right of the figure was used to remove the bit.

Figure 2.11 Special bits

The testing system consisted of 3 components: a compressive and shearing stress loading device, a displacement meter, and a pressure gauge. Fig.2.4 shows the compressive and shearing stress loading device, which was comprised of two square steel frames, rocker arms for adding vertical and horizontal pressure, two glass blocks, a vertical pressure gauge, a horizontal pressure gauge, and a horizontal displacement meter. The rocker arm is for slowly adding the load, which increased the pressure. The two glass blocks on the top and bottom of the prismatic clay samples created a constant degree of pressure and were placed in the center of the rigid indenter to ensure accurate analysis of the force.

2.2.3 Preparations o samples

First, the clay was placed into a used laboratory metallic contaniner, and mixed by hand with distilled water at room temperature for about twenty minutes until the texture was nearly uniform. Then this viscous clay was carefully placed into the designed boxes, which were completely filled to create prismatic clay samples samples with the dimensions specified above. Once the boxes were completely full, the top surface of the cube was modified by a sharp knife. Then compressive force was applied by steel blocks that was placed on the top of the box to fix the shape and allow the cube to drain.

Once formed, the samples were allowed to dry in the laboratory for 24 hours, and then a quarter of the cube were cut after removing the sample out of bits. Another two days of drying allows the samples to solid completely. Fig.2.12, below, shows the different initial angle of the notches cut into the semi-prismatic clay samples uesd in this study.

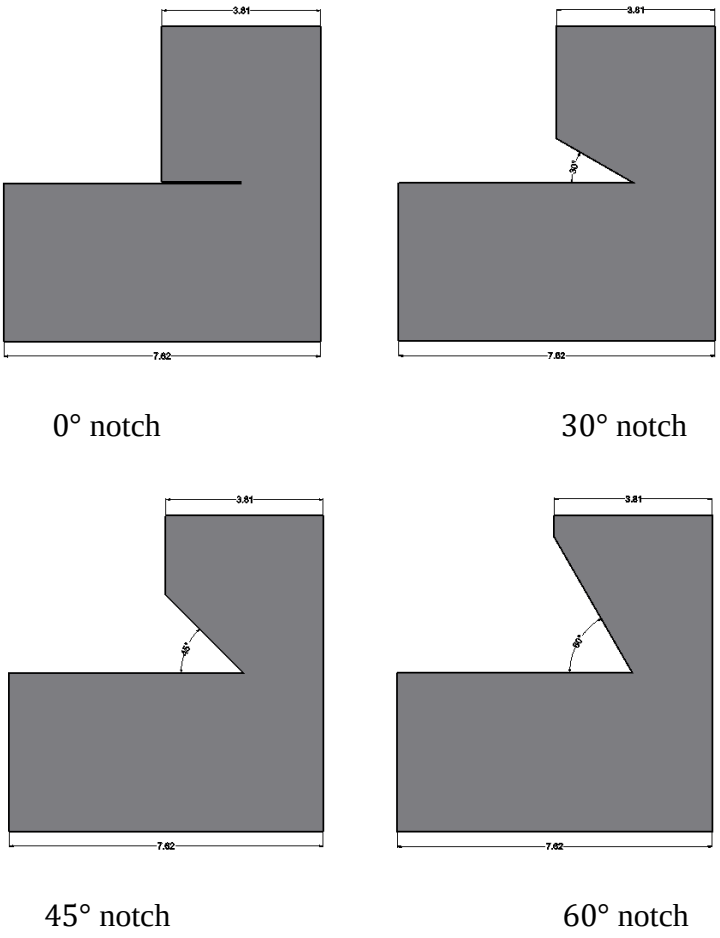

Figure 2.12 samples of notches of different initial angle

The samples were finished by groups, one of the group is shown in Fig.2.13.

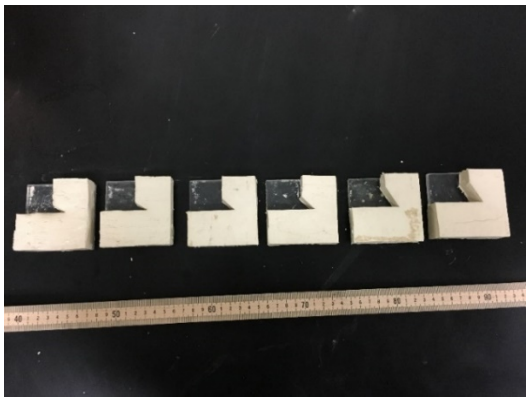

Figure 2.13 one group of the sample

2.2.4 Testing

In the direct shear experiment the sample was placed in the compressive and shearing stress loading device. This sample can be seen in Fig.2.14. Once the sample was fit into the steel frame, it was positioned to came in touch with the top and bottom sides of the frame and was nearly in contact with the right side of the frame. After calibrating the displacement meter and pressure gauge, the test began, the designed compressive pressure was first applied on the top of the specimen, and then the lateral shear force was added. During the test, to ensure the pressure applied on the top of specimen was constant, one person was holding and regulating the rocker arm through the test. The values of the displacement meter and pressure gauge were recorded every ten scales of the dial plate during the process until a final crack occurred through the notch of the sample. As in this shear experiments, this crack represented the failure of the sample, and, once it appeared, the test was over. Finally, the values from the displacement meter and pressure gauge were transformed into standard form for later analysis of results.

Some samples were applied pressure in a different way, which would be applied the lateral pressure first and then applied compressive pressure. The rest procedure was the same.

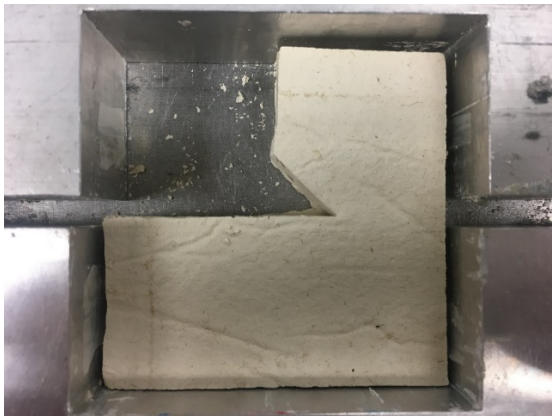

Figure 2.14 one sample of compressive and shearing experiment

Other analogous experiments done using the same process are shown in Fig.2.15

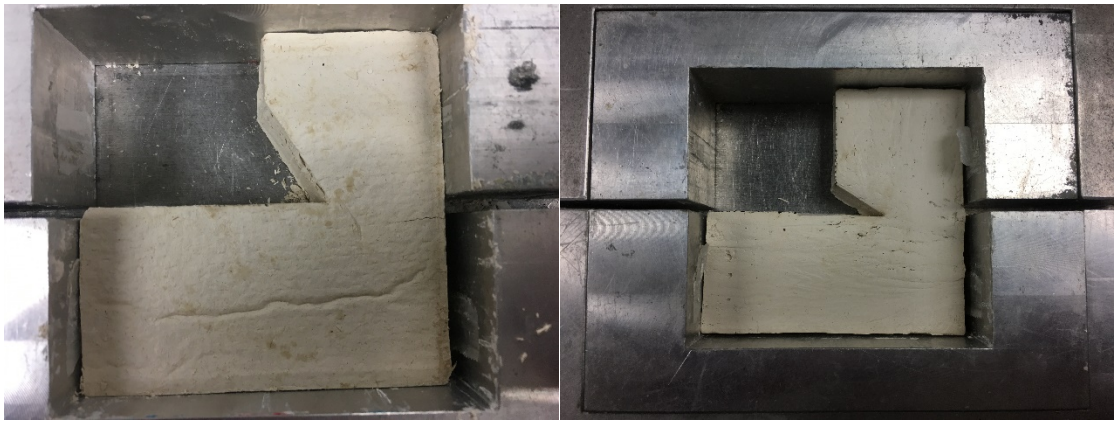

Figure 2.15 other samples of compressive and shearing experiment

3.0 THEORETICAL ANALYSIS

3.1 LINEAR ELASTIC FRACTURE MECHANICS

Linear elastic fracture mechanics (LEFM) is generally seen as the most important basic theory of fracture. Griffith [23][24] first worked on this theory while doing research on the strength of glass, and his initial theory was subsequently complemented by major researchers in the field such as Irwin [25][26] and Rice [27].

LEFM is an extraordinarily delicate and complex theory that applies to sharp cracks in elastic bodies. LEFM assumes that the material being modeled is isotropic and linearly elastic, these presumptions based on the assumption that the stress field near the crack tip can be calculated using current theory regarding elasticity. When the stresses near a crack tip exceed the material fracture toughness, the crack will grow. In Linear Elastic Fracture Mechanics, most formulas are derived for either plane stresses or plane strains; these are associated with the three basic modes of loadings on a cracked body: opening, sliding, and tearing. Again, LEFM is valid only when the inelastic deformation is small compared to the size of the crack, what is called small-scale yielding. In cases where large zones of plastic deformation develop before the crack grows, linear elastic fracture mechanics (LEFM) does not apply.

In this chapter, a number of studies of LEFM will be discussed, especially cases in which LEFM was used to explain geotechnical engineering problems using. First, fundamental features

will be discussed in order to demonstrate how cracks and crack development have been characterized in theory prior to the use of LEFM. Secondly, we will compare results of current laboratory experiments with earlier theoretical results.

3.2 FRACTURE MECHANICS APPROACH

Before introducing linear fracture mechanics as related to specific geotechnical engineering models, it is necessary to first review Griffith's laboratory work on the tensile strength of glass [23]. Some specific characteristics had an obvious influence on the tensile strength of the material, as was mentioned by Griffith. And in addition to the natural properties of the material, some other factors also affected the variability in tensile strength of the material. In cases where the material molded contained some certain flaws, the common design approach based on the criteria of material's strength would not be applicable anymore since the stress, which is infinitely high concentrating at the tip of the sharp crack no matter how small the load, applying on the model, is. Therefore, the fracture mechanics approach could be used when the model has some certain flaws.

Griffith's hypothesis assumes that surfaces of solid model are characterized by surface tension analogous to that found in liquids. His theory is based on balancing the reduction of potential energy that occurs during fracture with the increase in surface energy caused by the creation of new free surfaces when a crack grows. In other words, crack development occurs only when the input energy rate exceeds the dissipated plastic necessary for crack development. The associated energy balance equation is written as:

$$\frac{\partial W}{\partial a} = \frac{\partial U_s^e}{\partial a} + \frac{\partial U_s^p}{\partial a} + \frac{\partial U_\Gamma}{\partial a} \tag{3.1}$$

in which W represents the work done by the external force, U_s^e and U_s^p indicate the elastic and plastic parts of the total strain energy separately, and U_Γ indicates the surface tension energy.

Eq. (3.1) can be rewritten to reflect the potential energy $\Pi = U_s^e - W$, that is,

$$-\frac{\partial \Pi}{\partial a} = \frac{\partial U_s^p}{\partial a} + \frac{\partial U_\Gamma}{\partial a} \tag{3.2}$$

This equation shows that the rate of release of the potential energy is equal to the rate of dissipation of the energy in plastic deformation and crack propagation, thus creating a stability criterion for the crack and normal states. Furthermore, the rate of energy input is independent of the load application pattern and this rate is related to the rate of releasing strain energy when the crack propagates in a unit length, as has been proven by Irwin [26].

The plastic term U_s^p is not used in the case of brittle materials, and in this case the energy balance equation is rewritten as:

$$\frac{\partial U_\Gamma}{\partial a} + \frac{\partial \Pi}{\partial a} = 0 \tag{3.3}$$

The stability of crack growth can be evaluated by simply considering the second derivative of $(\Pi + U_\Gamma)$; the state of the crack propagation will depend on whether the energy state at equilibrium is equivalent to its maximum or minimum value, determining alone whether the state is stable or unstable. The fracture propagation criterion equation is shown as:

$$\frac{\partial^2(\Pi + U_\Gamma)}{\partial a^2} = \begin{cases} < 0 & \text{unstable fracture} \\ > 0 & \text{stable fracture} \\ = 0 & \text{neutral equilibrium} \end{cases} \tag{3.4}$$

The strain energy release rate $\mathcal{G}$ can be expressed as

$$\mathcal{G} = -\frac{\partial \Pi}{\partial a} = 2\gamma_s \tag{3.5}$$

Due to the existence of two crack surfaces, the surface energy γ_s should be doubled.

Substituting Eq. (3.5) in Eq. (3.3), the equation of energy balance can now be rewritten as:

$$\mathcal{G} - \frac{\partial U_\Gamma}{\partial a} = 0 \tag{3.6}$$

Consider a through thickness crack of length 2a, subjected to a uniform tensile stress σ, at infinity as shown in Fig 3.1, below. Crack propagation occurs when the released elastic strain energy is at least equal to the energy required to generate a new crack. The equation is shown as:

$$\Pi = 4\int_0^a \sigma u_y(x)dx = \frac{\pi\sigma^2 a^2}{2E'} \quad \Longrightarrow \quad \mathcal{G} = \frac{\pi a\sigma^2}{E'} \tag{3.7}$$

where E', an important parameter in fracture mechanics, is given by

$$E' = \begin{cases} E & \text{Plane stress} \\ \dfrac{E}{1-\upsilon^2} & \text{Plane strain} \end{cases} \tag{3.8}$$

in which E represents Young's modulus and υ represents the Poisson's ratio.

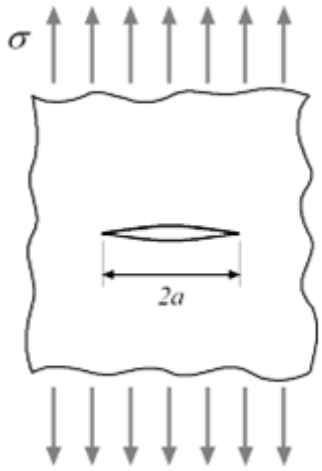

Figure 3.1 Infinite plate with central crack of length 2a, subjected to a uniaxial stress state [28]

Substituting Eq. 3.5 in Eq. 3.5, the relationship between the critical stress and the surface energy can be described as:

$$\sigma_{cr} = \sqrt{\frac{2E'\gamma_s}{\pi a}} \tag{3.9}$$

In general, Griffith proposed that a brittle material contains a number of micro-cracks which causes the stress to increase in localized regions having only a nominal stress well below the theoretical value. When one of the cracks spreads into a brittle fracture, it produces an increase in the surface energy of the sides of the crack. The source of the increased surface energy is the elastic strain energy, which is released as the crack spreads. Griffith's criteria for propagation of cracks include these terms as: a crack will propagate when the decrease in elastic energy is at least equal to the energy required to create the new crack surface. This criterion is useful in determining the tensile stress, which will cause a critical sized crack to propagate as a brittle fracture. And this theory provides the energy balance criterion, which allows us to determine whether the crack propagation is stable or unstable by using LEFM, and this is helpful in analyzing the crack propagation and characterizing the fracture extension rate.

3.3 STRESS INTENSITY FACTOR AND ENERGY RELEASE RATE

Although Griffith established an energy balance criterion to determine whether the crack propagation is stable or not, no general term can be used to describe the stress state at the crack tip. Irwin [25] found that all the stress equations contain the expression as $\sigma_{cr}\sqrt{\pi a}$, which can be used to describe the stress state of crack tip comprehensively by combining σ_{cr} and a. When σ_c, the critical value of stress at which crack extension starts, is reached:

$$K_{\mathrm{IC}} = \sigma_{cr}\sqrt{\pi a} \tag{3.10}$$

Combining Eq. 3.5, Eq. 3.9, and Eq. 3.10, Irwin discovered an important relationship between stress intensity factor K_{I} and energy release rate $\mathcal{G}$ as:

$$K_{\mathrm{I}} = \sqrt{E'\mathcal{G}} \tag{3.11}$$

A crack propagation can be extremely complicated; however, it can be described by combining three basic crack models of loading conditions. These basic crack opening models are shown in Fig 3.2, below:

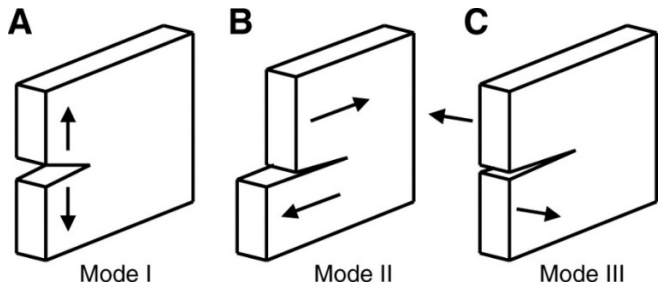

Figure 3.2 Sketches of crack opening modes: (a) Mode **I** or pure opening mode; (b) Mode **II** or in-plane shear mode; (c) Mode **III** or anti-plane shear mode [29]

- Mode I, The applied tensile stress is perpendicular to the crack surface and is also perpendicular to the front line of crack propagation. Under the action of external force, the crack extends along the direction of the original crack cracking.
- Mode II, The external shear stress is parallel to the crack surface, but perpendicular to the crack front line. Under the action of external force, the crack spreads along the direction of the original crack at a certain angle.
- Mode III, The external shear stress is parallel to the crack surface and parallel to the front line of crack propagation. So that the crack surface staggered. Under the action of external force, the crack spreads along the direction of the original crack.

The stress intensity factor (K) is highly used in the field of fracture mechanics. It predicts stress intensity near the tip of a crack caused by a remote load or residual stresses. The magnitude of K depends on: the sample geometry, the size and location of the crack, the magnitude of its load, and the distribution of the load. The stress intensity factor is a single-parameter characterization of the crack tip stress field. The stress intensity factor is fundamental and very useful in all of fracture mechanics, not only in LEFM.

3.4 STRESS CONCENTRATION AND DISTRIBUTION AROUND HOLES

The theoretical study of stress concentrations and distribution around openings were first investigated by Kirsch [30], who established a linear elastic solution for stresses around a circular opening on a finite plate under uniaxial compression, investigated in the first test of this study for specified loading condition. Beginning with this initial solution, a more theoretical analysis of different loading conditions with different shapes openings is now further investigated. The solutions of stress concentrations and distribution around the circle hole under different loading conditions are obtained in this study. Relatedly, Jaeger and Cook provided the solutions for the stress distribution around ellipse opening, which was expressed relative to elliptical curvilinear coordinates.

3.4.1 Circular opening

Kirsch [30] originally investigated the solution for the stress state of circular openings under uniaxial tension. σ_∞ represents the remote stress, a represents the radius of the circular opening, r

represents the radial coordinate, θ denotes the angle from the line aligning with the remote loading direction counterclockwise; the stress around the circular opening in Fig 3.3, can be described in equations as:

$$\sigma_{rr} = \frac{P}{2}\left\{\left[1-\left(\frac{a}{r}\right)^2\right]+\left[1-4\left(\frac{a}{r}\right)^2+3\left(\frac{a}{r}\right)^4\right]\cos 2\theta\right\}$$

$$\sigma_{\theta\theta} = \frac{P}{2}\left\{\left[1+\left(\frac{a}{r}\right)^2\right]+\left[1+3\left(\frac{a}{r}\right)^4\right]\cos 2\theta\right\} \quad (3.12)$$

$$\tau_{r\theta} = -\frac{P}{2}\left[1+2\left(\frac{a}{r}\right)^2-3\left(\frac{a}{r}\right)^4\right]\sin 2\theta$$

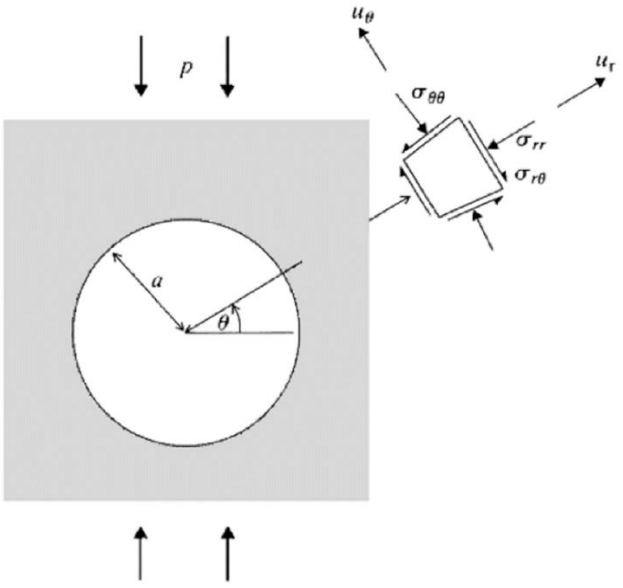

Figure 3.3 Stress analysis around the circular opening under uniaxial stress field [31]

When both vertical stress and horizontal stress are applied simultaneously, the vertical stress is p and the horizontal stress can be indicated as Kp. This is shown in Fig 3.4. Therefore, the solution for this stress state of circular opening under biaxial tension is shown as:

$$\sigma_{rr} = \frac{P}{2}\left\{(1+K)\left[1-\left(\frac{a}{r}\right)^2\right]+(1-K)\left[1-4\left(\frac{a}{r}\right)^2+3\left(\frac{a}{r}\right)^4\right]\cos 2\theta\right\} \quad (3.13)$$

$$\sigma_{\theta\theta} = \frac{P}{2}\left\{(1+K)\left[1+\left(\frac{a}{r}\right)^2\right] + (1-K)\left[1+3\left(\frac{a}{r}\right)^4\right]\cos 2\theta\right\}$$

$$\tau_{r\theta} = -\frac{P}{2}(1-K)\left[1+2\left(\frac{a}{r}\right)^2 - 3\left(\frac{a}{r}\right)^4\right]\sin 2\theta$$

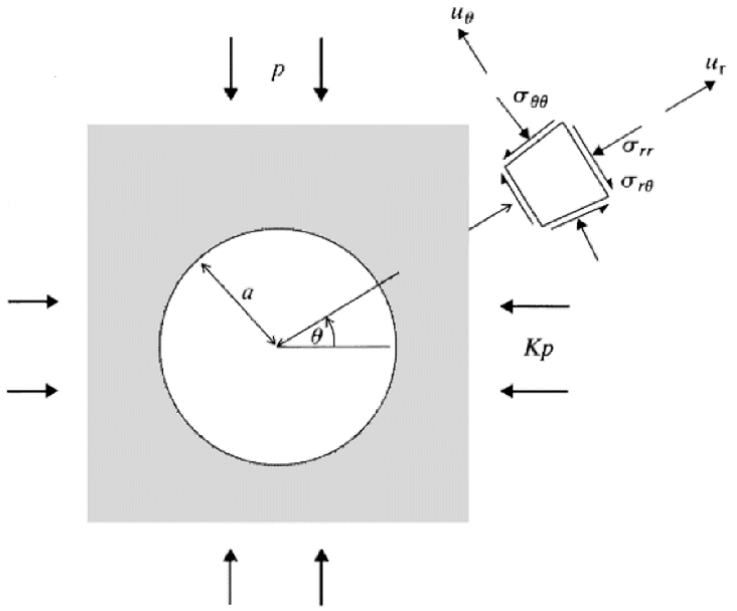

Figure 3.4 Stress analysis around the circular opening under biaxial compression field [31]

Substituting $r = a$ in Eq. 3.13, the stress on the opening boundary can be derived as:

$$\sigma_{\theta\theta} = p[(1+K) + 2(1-K)\cos 2\theta]$$

$$\sigma_{rr} = 0 \qquad (3.14)$$

$$\sigma_{r\theta} = 0$$

In Eq. 3.14, Brady & Brown 0 explained that the opening boundary is traction free with the imposed condition. This equation also defines the state of stress related to the co-ordinate angle θ on the boundary of a circular opening under biaxial stress field. Due to the traction boundary free of the circular opening boundary, only tangential stress $\sigma_{\theta\theta}$ is non-zero component in this

equation. When $K < 1$, the maximum and minimum boundary stresses occur at the side wall ($\theta = 0$) and crown ($\theta = \pi/2$) of the opening and stress are shown below:

$$\begin{aligned} &\text{at point A: } \theta = 0,\ \sigma_{\theta\theta,A} = \sigma_A = p(3 - K) \\ &\text{at point B: } \theta = \tfrac{\pi}{2},\ \sigma_{\theta\theta,B} = \sigma_B = p(3K - 1) \end{aligned} \tag{3.15}$$

When the $K = 0$, this expression also indicates and the maximum and minimum stresses under biaxial tress field as:

$$\sigma_A = 3p, \sigma_B = -p \tag{3.16}$$

The upper and lower limits for the stress concentration of circular opening is indicated by these values. This shows that the side wall stress is lower than $3p$ and crown stress is larger than $-p$ when $K > 1$

For the second case of the circular opening above, the equation derived above of the biaxial stress field can be transferred using Mohr's Circle. The resulting stresses are shown as:

$$\begin{aligned} p = \sigma_1 &= \frac{\sigma_y + \sigma_x}{2} + \sqrt{\left(\frac{\sigma_y - \sigma_x}{2}\right)^2 + {\tau_{xy}}^2} \\ Kp = \sigma_3 &= \frac{\sigma_y + \sigma_x}{2} - \sqrt{\left(\frac{\sigma_y - \sigma_x}{2}\right)^2 + {\tau_{xy}}^2} \end{aligned} \tag{3.17}$$

3.4.2 Elliptical opening

Solutions for the stress distribution in this case are cited from Poulos and Davis [32] and Jaeger and Cook [33]. Elliptical curvilinear co-ordinates are applied, in the two cases, to express the solutions. Heok, E., and J. W. Bray [34] provided a set of formulae that make it simpler to calculate the state of stress for an elliptical opening. The problem geometry is shown in Fig.3.5. The lateral

stress Kp is parallel to the direction of global x axis, and the local x_1 axis for the opening is determined by an axis of the ellipse. The width, W, of the ellipse is measured in the direction of x_1 axis, and the height, H, in the direction of the local z_1 axis. The angle between local and global axes is expressed as β. The position of the elliptical opening in the biaxial stress field is depicted by the angle between the local and global axes. The boundary stress of any point in the boundary surface, shown in Figure 3.5, can be define as:

$$\sigma = \frac{p}{2q}\{(1+K)[(1+q^2)+(1-q^2)cos2(\theta-\beta)] - (1-K)[(1+q)^2\cos 2\theta + (1-q)^2\cos 2\beta]\} \tag{3.18}$$

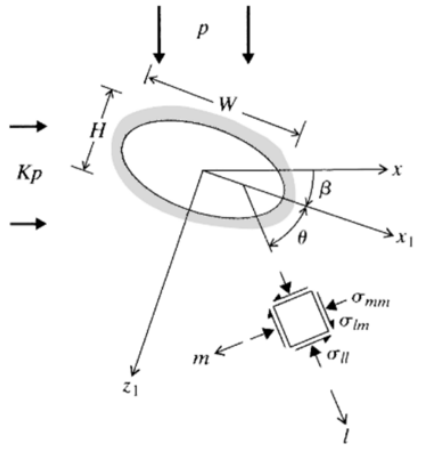

Figure 3.5 Stress analysis around the inclined elliptical opening under biaxial compression field [31]

where p denotes the vertical force, K denotes the ratio between the vertical and lateral stress, $q = W/H$, which is the ratio between width and height of the elliptical opening, θ denotes the angle between the selected point and the local x_1 axis in counter clockwise, $\theta = \arctan[(\frac{e+1}{e-1})^2 \frac{z_1}{x_1}]$.

For the case above, when the local x_1 axis is parallel to the global x axis, as is shown in Fig 3.6, the solution can be written as:

$$\sigma = \frac{p}{2q}\{(1+K)[(1+q^2)+(1-q^2)cos2\theta] - (1-K)[(1+q)^2\cos 2\theta + (1-q)^2]\} \tag{3.19}$$

boundary stresses occurring at the side wall ($\theta = 0$) and crown ($\theta = \pi/2$) of the ellipse opening are depicted as:

$$\sigma_A = p(1-K+2q)$$
$$\sigma_B = p(K-1+2K/q) \tag{3.20}$$

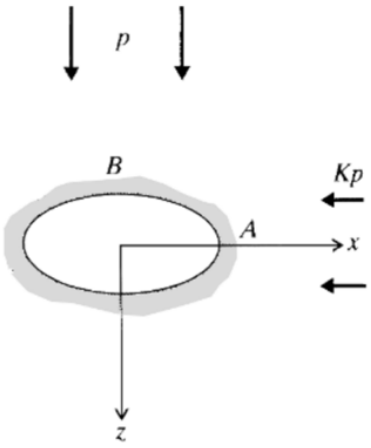

Figure 3.6 Stress analysis around a horizontal elliptical opening under biaxial compression field [31]

3.5 STRESS FILED AT A CRACK TIP

First developed by Erdogan and Sih [35], the maximum tangential stress criterion of LEFM provides solutions to demonstrate the stress field around a crack tip. Afterwards, Vallejo [36] used this theory to identify, in a laboratory experiment, the direction of the secondary crack propagation of a clay sample with a pre-existing crack tip.

Due to this criterion, r represents the distance from the crack tip, θ represents the angle between radius r and the direction of local x' axis, $\sigma_{\theta\theta}$ represents the tangential stress, σ_{rr} denotes the radial stress, and $\tau_{r\theta}$ represents the shear stress. Stresses around a crack tip [37], as shown in Fig.3.7, can be written as:

$$\sigma_{\theta\theta} = \frac{1}{\sqrt{2\pi r}} cos\frac{\theta}{2}\left[K_{\mathrm{I}} cos^2\frac{\theta}{2} - \frac{3}{2}K_{\mathrm{II}} sin\theta\right]$$

$$\sigma_{rr} = \frac{1}{\sqrt{2\pi r}} cos\frac{\theta}{2}\left[K_{\mathrm{I}}(1 + sin^2\frac{\theta}{2}) + \frac{3}{2}K_{\mathrm{II}} sin\theta - 2K_{\mathrm{II}} tan\frac{\theta}{2}\right] \tag{3.21}$$

$$\tau_{r\theta} = \frac{1}{\sqrt{2\pi r}} cos\frac{\theta}{2}[K_{\mathrm{I}} sin\theta + K_{\mathrm{II}}(3cos\theta - 1)]$$

where K_{I} and K_{II} are stress intensity factors under loading in Mode I and Mode II are given as:

$$K_{\mathrm{I}} = 1.1215\ \sigma_n(\pi c)^{1/2}$$

$$K_{\mathrm{II}} = 1.1215\ \tau\ (\pi c)^{1/2} \tag{3.22}$$

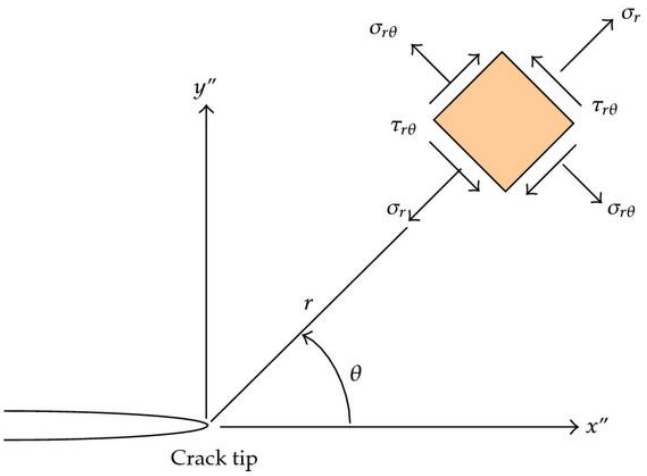

Figure 3.7 Crack tip stresses and system of reference [38]

where σ_n is the normal stress on the plane of the crack opening, τ is the shear stress on the plane of crack opening, and c is half of the length of the entire crack, in this case, just the length of the opening crack in Fig.3.7, which is considered one half of the whole crack.

The hypothesis that crack extension takes place when $\sigma_{\theta\theta}$ reaches its maximum value is demonstrated by Vallejo [19]. In other words, the crack develops from the crack tip and along the radial direction, which is perpendicular to the direction of maximum tangential stress $\sigma_{\theta\theta}$. Therefore, when θ reaches a certain value α, crack propagation takes place, and this angle should satisfy:

$$\frac{d\sigma_{\theta\theta}}{d\theta} = 0 \quad at \quad \theta = \alpha_t \tag{3.23}$$

$$\frac{d^2\sigma_{\theta\theta}}{d^2\theta} < 0 \quad at \quad \theta = \alpha \tag{3.24}$$

Combining Eq.3.21 and Eq.3.22 into Eq.3.23, the solution for the direction of crack propagation can be obtained as:

$$K_{\mathrm{I}} sin\alpha + K_{\mathrm{II}}(3cos\alpha - 1) = 0 \tag{3.25}$$

This equation is only for the case with the opening crack. For a closed crack, the stress intensity factor for Mode I equals zero, and Eq. 3.25 can be derived as ($K_{\mathrm{II}} \neq 0$):

$$3\cos\alpha - 1 = 0 \tag{3.26}$$

From Eq.3.26, the theoretical value of the angle of secondary crack propagation, α_t, with open crack, can be calculated and is found to be equal to 70.5°.

LEFM is efficient dealing with stress analysis around a crack tip in brittle material. Meanwhile, we can use LEFM to predict the direction of secondary crack propagation through the maximum tangential fracture criterion.

3.6 STRESS FILED AT A CRACK TIP WITH DIFFERENT INITIAL ANGLE

Theoretical solutions provided by Erdogan and Sih [35] are applicable for the simplest model, a model with a notch of 0°. However, for cases in which the notches have different initial angles, the solution should be further explored. When the σ_n presented the normal stress on the notch of 0°, the τ presented the shear stress on the notch of 0°, and the σ_n' and τ' presented the normal stress and shear stress on the notch of an initial angle β, the solution can be derived as

$$\begin{aligned} \sigma_n' &= \sigma_{n2} + \tau_1 \\ &= \sigma_n \cos\beta + \tau \sin\beta \\ \tau' &= \tau_2 - \sigma_{n1} \\ &= \tau \cos\beta - \sigma_n \sin\beta \end{aligned} \tag{3.27}$$

In the Eq.3.27, the σ_n can be broken down to σ_{n2} and σ_{n1}, which are parallel and perpendicular to the notch surface, respectively, and τ can be broken down to τ_1 and τ_2, which are perpendicular and parallel to the notch surface, respectively, as shown in Fig.3.8.

t' presented the ratio of the shear stress, $\tau'$and normal stress, σ_n'. In a notch of an initial angle β, it can be presented as:

$$t' = \frac{\tau'}{\sigma_n'} = \frac{\tau \cos\beta - \sigma_n \sin\beta}{\sigma_n \cos\beta + \tau \sin\beta} \tag{3.28}$$

where t presented the ratio of the shear stress, τ and normal stress, σ_n. $t = \tau/\sigma$.

the solution for the direction of crack propagation in a notch of an initial angle β can be obtained as:

$$\sin\alpha + t'(3\cos\alpha - 1) = 0 \tag{3.29}$$

where

$$t' = \frac{t - \tan\beta}{1 + t\tan\beta} \tag{3.30}$$

As the equation above shows, if β increases, t' decreases as well. Based on Eq.3.29, a graph showing the relationship between t' and the theoretical value of the angle of secondary crack propagation, α_t, can be obtained. This graph shows that when t' decreases the α_t increases as well. This indicates that when there is a larger initial angle, β of a notch with the same t will cause a larger angle of the secondary crack propagation, α_t, as well.

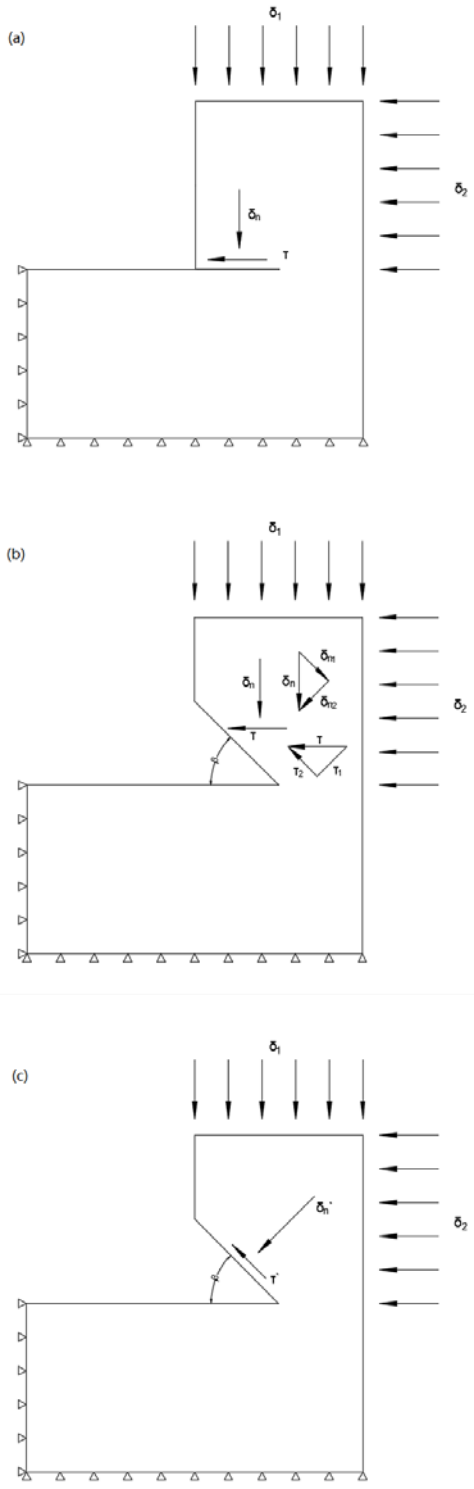

Figure 3.8 Loading transformation from the normal notch to the notch with an initial angle $\boldsymbol{\beta}$

(a) normal and shear stress acting on the normal notch; (b) load resolution of the normal and shear stress; (c) resulted normal and shear stress on a notch with an angle

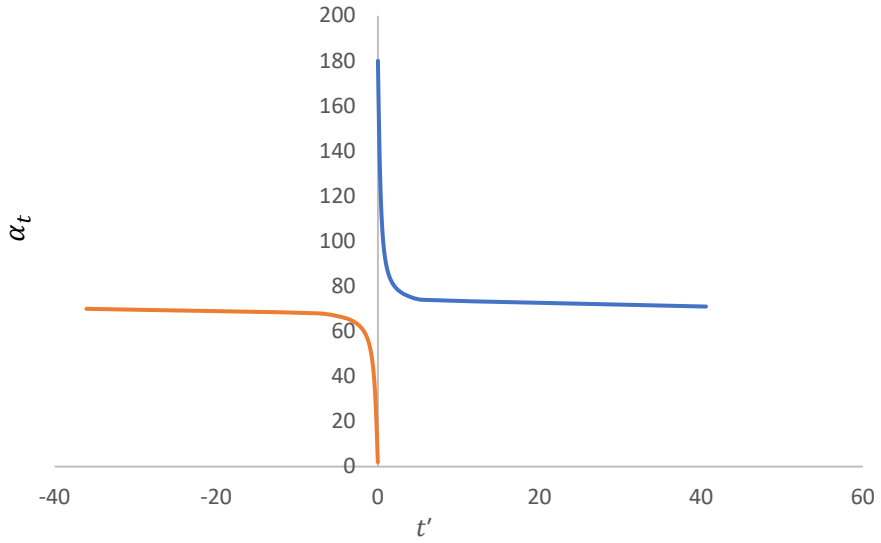

Figure 3.9 the relationship between t' and α_t

4.0 ANALYSIS OF RESULTS

4.1 ANALYSIS OF LABORATORY RESULTS

This section analyzes the data for the maximum normal stress, σ_{max} and for the angle of the crack, α derived from the laboratory procedures descried earlier. Because the prismatic samples have different shape openings, in order to analyze the results of all samples, they have been categorized into several groups for comparison. In this chapter, we focus on the maximum of normal stress, σ_{max} and the angle of the crack, α. The σ_{max} and α of the samples were compared in order to detect possible patterns in how σ_{max} and α differ between and among the groups of samples with different types openings.

4.1.1 Analysis of prismatic samples

4.1.1.1 Description of each sample

The first group

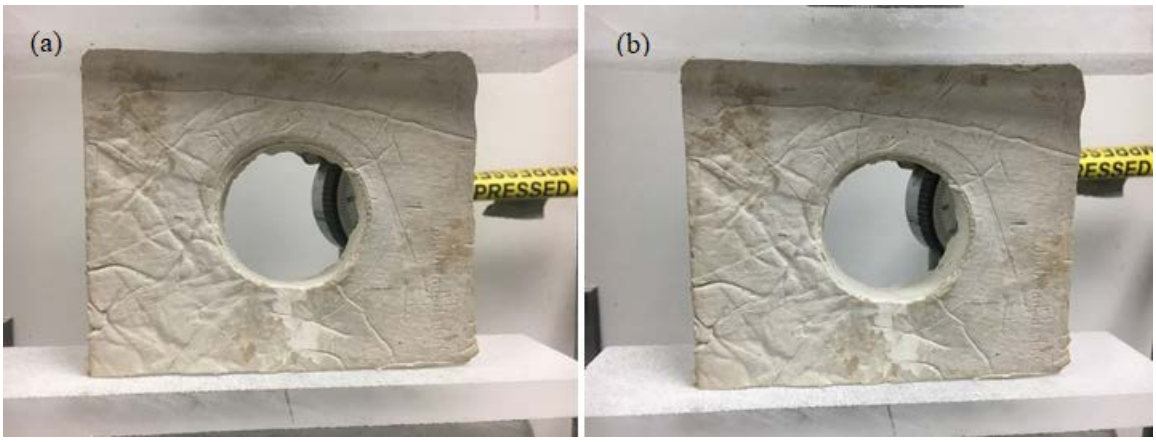

Figure 4.1 (a) the state of installation of circle 2, and (b) the state of failure of circle 2

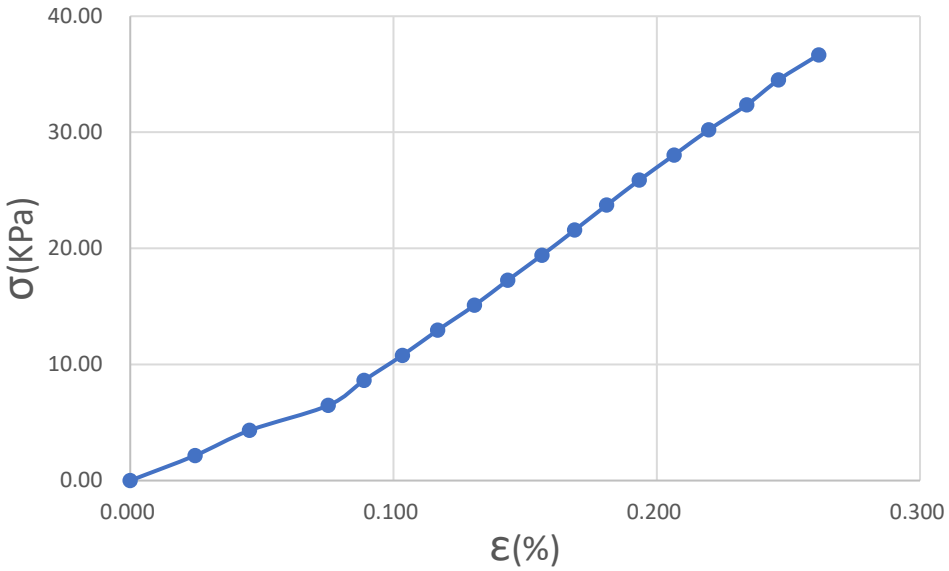

Figure 4.2 Stress-strain curve

As the figure shows, σ_{max} is 36.67KPa and the final strain is approximately 0.262%. An upward-moving main crack developed in the top of the opening and continued through it; the angle α_t was 81°.

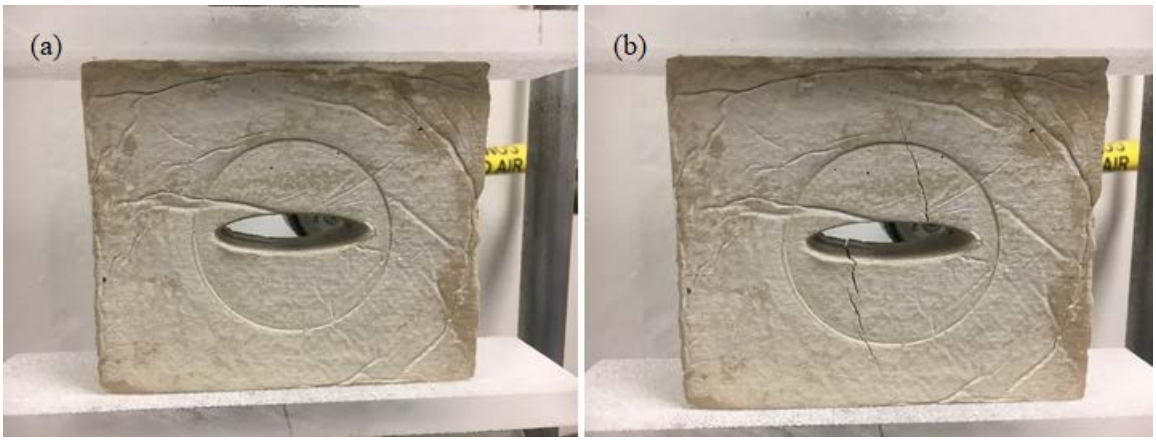

Figure 4.3 (a) the state of installation of ellipse 5 (b) the state of failure of ellipse 5

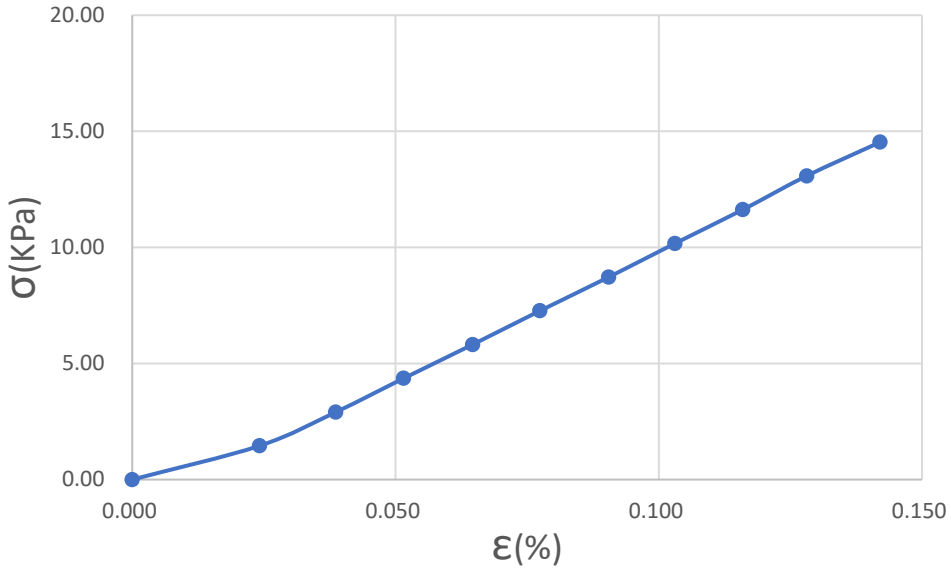

Figure 4.4 Stress-strain curve

As the figure shows, the σ_{max} is about 14.532KPa and the final strain is around 0.142%. Two main cracks developed through the opening, and they were antisymmetric. The crack angle on the top of the opening α_t was 104°, the angle on the bottom side of the opening α_b was 110°.

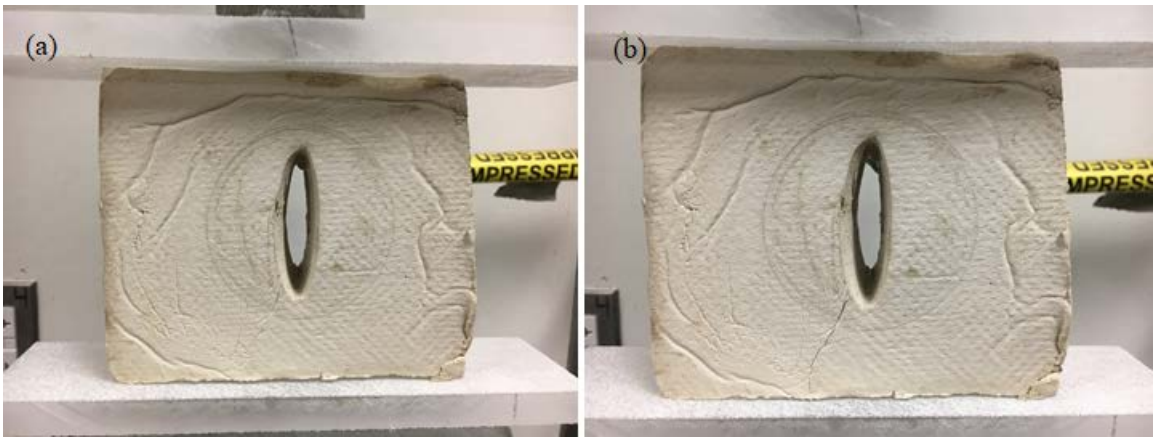

Figure 4.5 (a) the state of installation of ellipse 6, and (b) the state of failure of ellipse 6

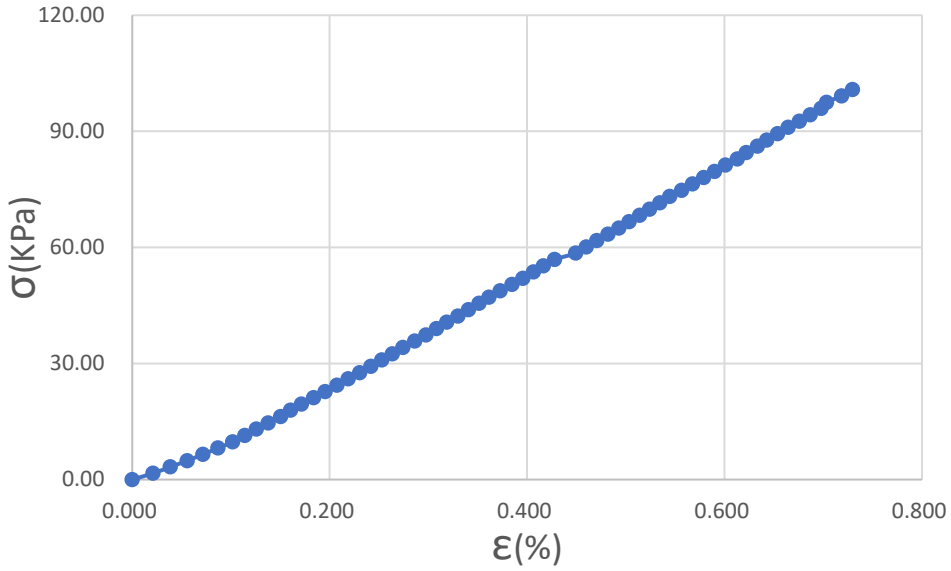

Figure 4.6 Stress-strain curve

As this figure shows, the σ_{max} is about 100.74KPa and the final strain is approximately 0.729%. A main crack developed towards the lower left portion of the bottom and through the opening, and its angle α_t was 60°.

The second group

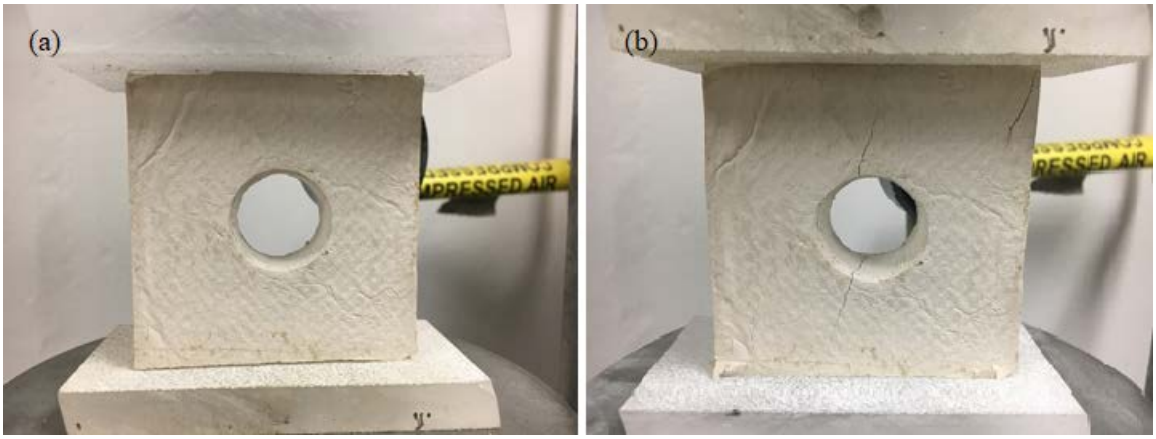

Figure 4.7 (a) the state of installation of circle 1, and (b) the state of failure of circle 1

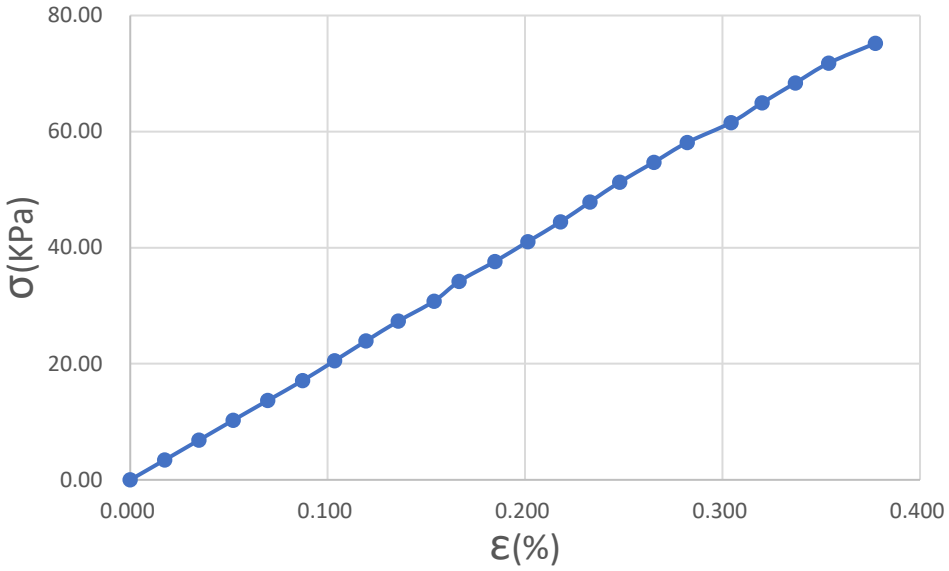

Figure 4.8 Stress-strain curve

As the figure[] shows, the σ_{max} is 75.224KPa and the final strain is 0.377%. In this sample, two antisymmetric cracks developed through the opening. The crack angle on the top of the opening α_t was 76°, and the angle on the bottom of the opening α_b was 70°.

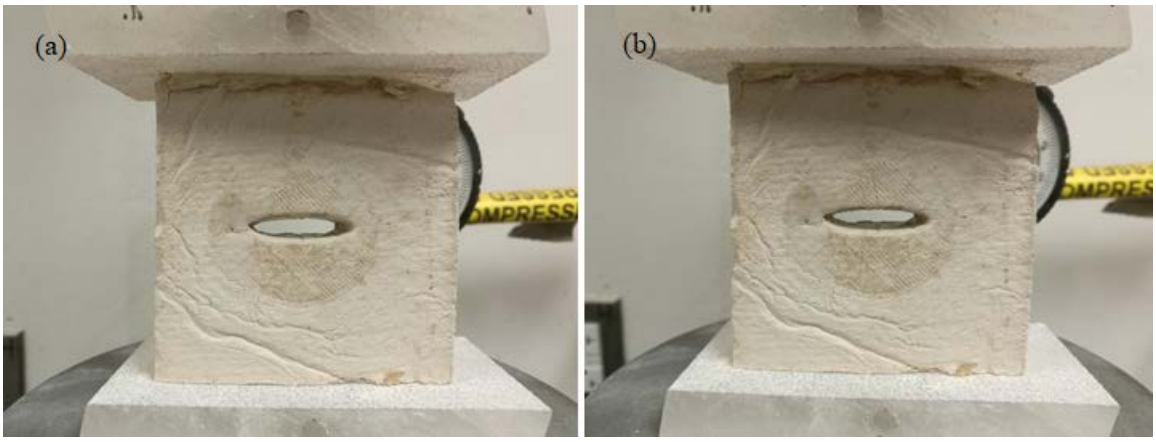

Figure 4.9 (a) the state of installation of ellipse 2, and (b) the state of failure of ellipse 2

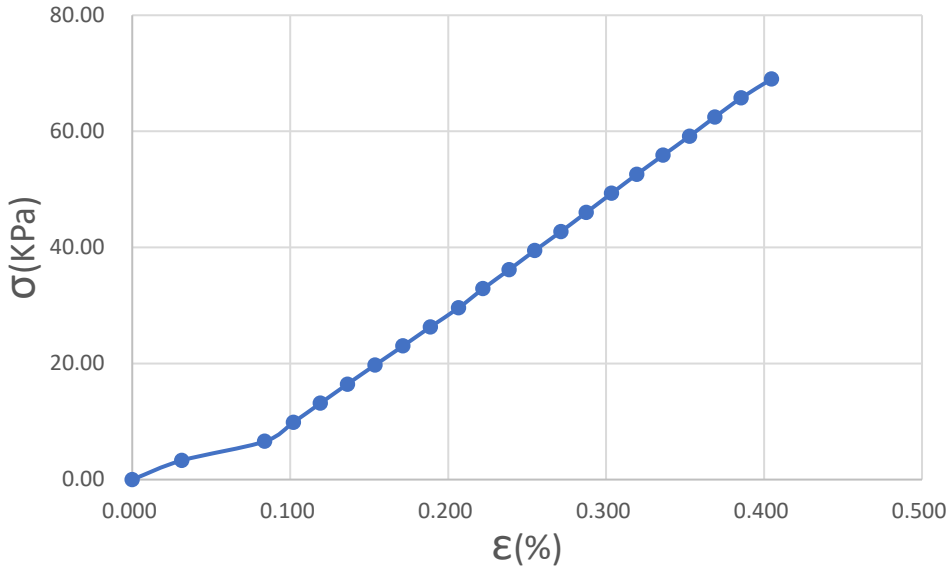

Figure 4.10 Stress-strain curve

As the figure above shows, the σ_{max} is 69.015KPa and the final strain is 0.405%. In this sample, two main cracks developed through the opening: the direction of the top one was towards the upper left, and the direction of the bottom one was towards the lower left. The crack angle on the angle above the opening α_t was 96°, the angle below the opening α_b was 86°.

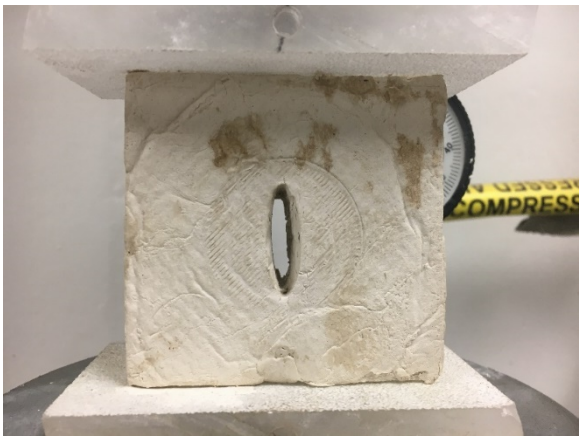

Figure 4.11 the state of installation of ellipse 4

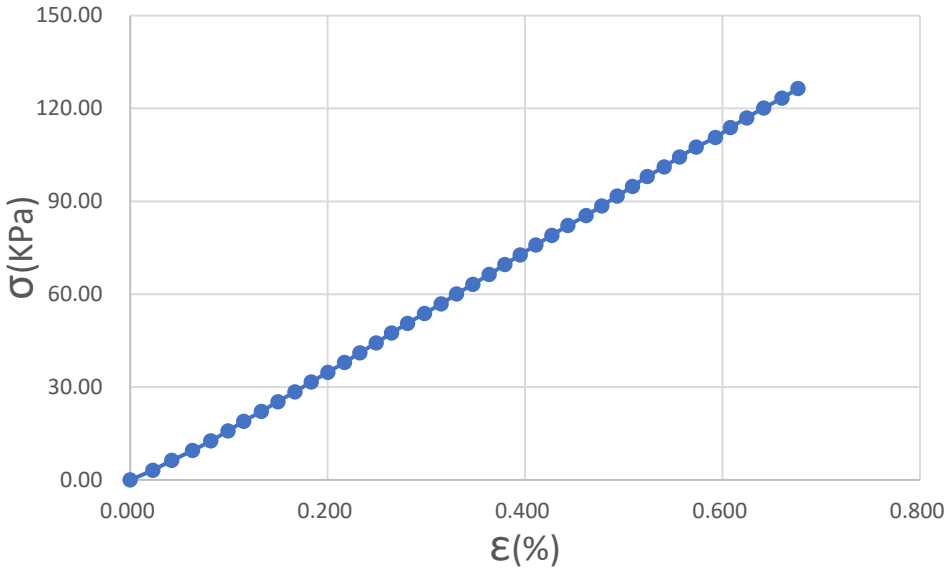

Figure 4.12 Stress-strain curve

During the test of ellipse 4, the sample suddenly failed and broke. Therefore, the figure of the crack could not be photographed in this situation. As the figure shows that the σ_{max} is 126.462KPa and the final strain is 0.676%.

The third group

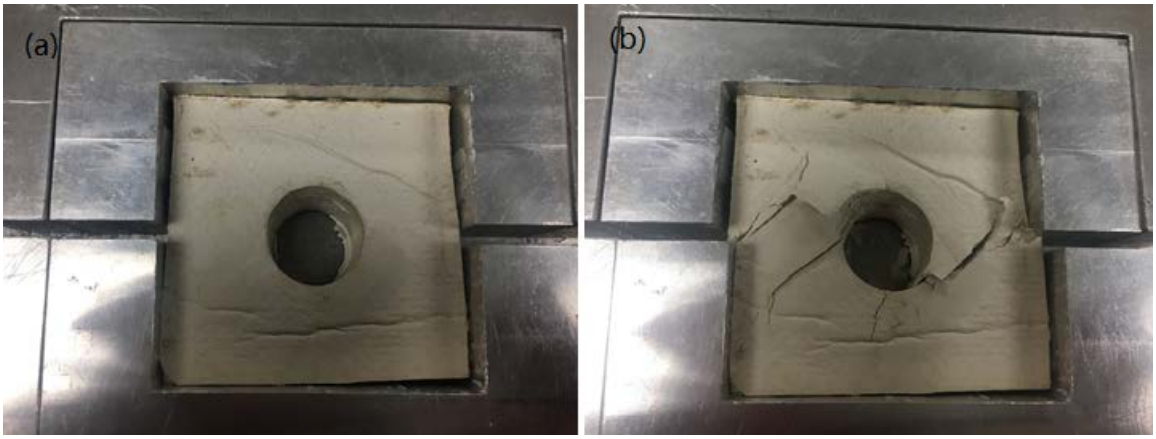

Figure 4.13 (a) the state of installation of circle 1, and (b) the state of failure of circle 1

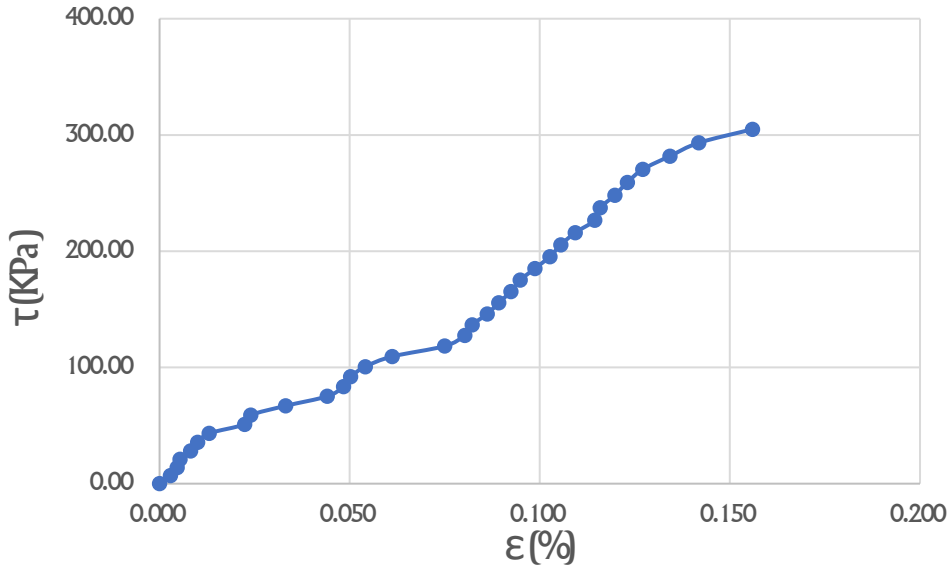

Figure 4.14 Stress-strain curve

In this figure above, the τ_{max} is 304.895KPa, and the final strain is 0.156%. Two main cracks developed on the left and right sides of the opening, respectively. The right one developed in the direction of the lower-left corner, and the left one developed towards the upper right section of sample. The crack angle on the right of the opening α_t was 36°, and the crack angle on the left side of the opening α_b was 41°.

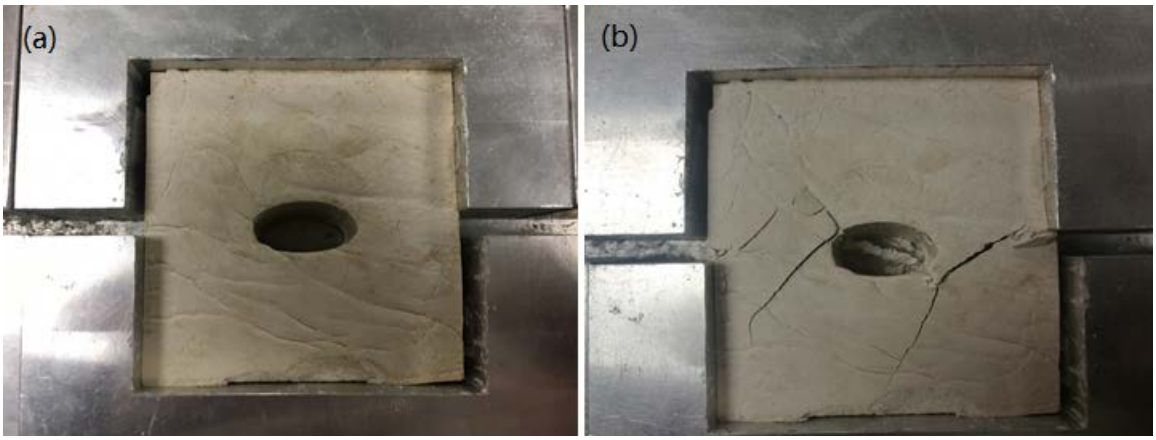

Figure 4.15 (a) the state of installation of ellipse 1, and (b) the state of failure of ellipse 1

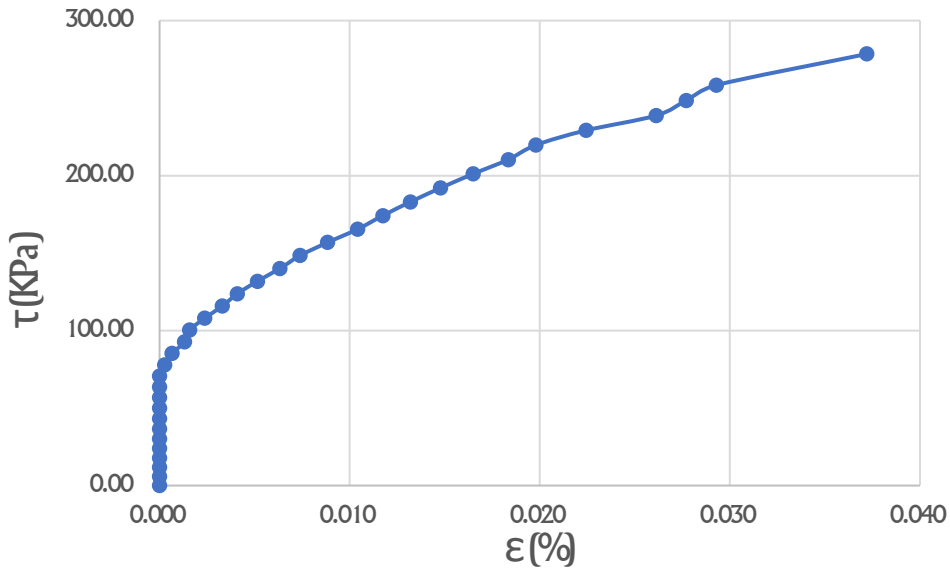

Figure 4.16 Stress-strain curve

In the figure above, the τ_{max} is 278.473KPa, and the final strain is 0.037%. Two main cracks developed, on the left and right side of the opening, respectively, with the right one developing toward the lower left and the left one developing towards the upper right. The crack angle on the right side of the opening α_t was 45°, and the crack angle on the left side of the opening α_b was 51°. These unusual results could have been caused by the uneven surface of both side of the prismatic clay sample.

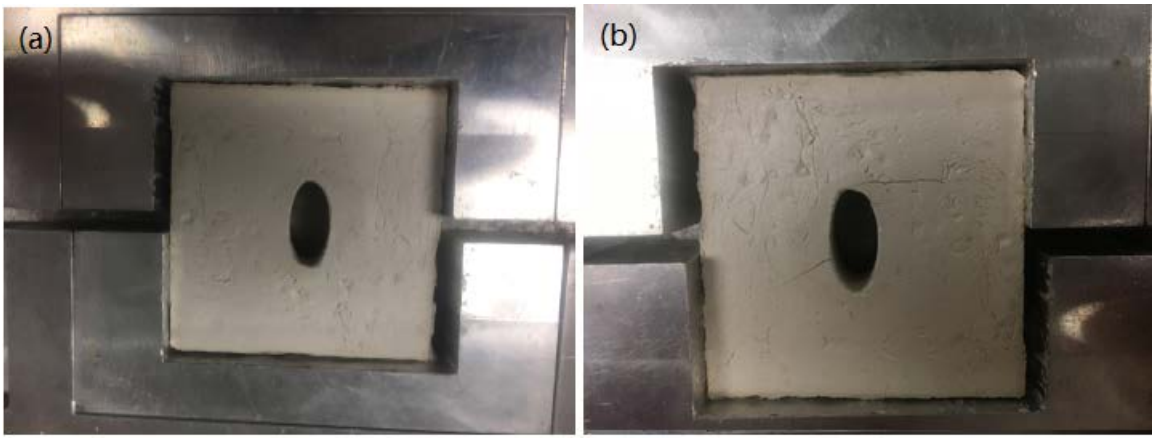

Figure 4.17 (a) the state of installation of ellipse 3, and (b) the state of failure of ellipse 3

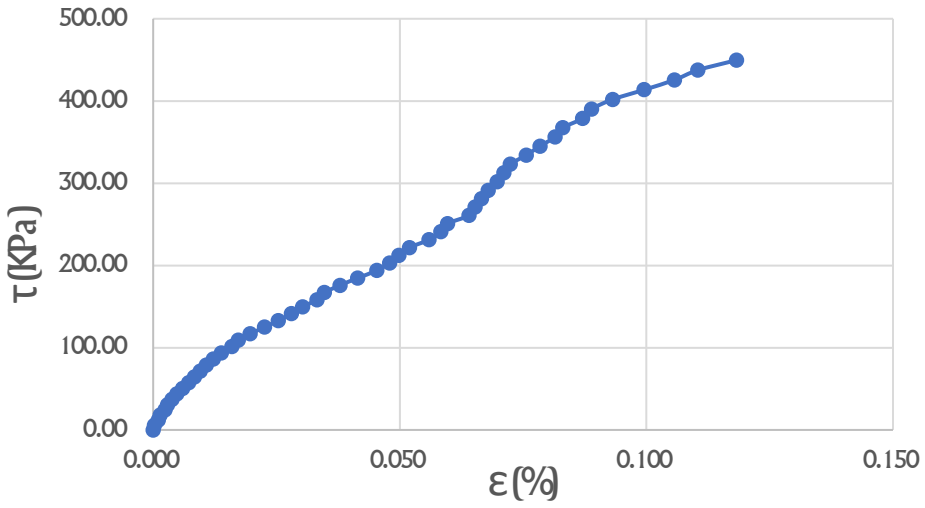

Figure 4.18 Stress-strain curve

In this figure, the τ_{max} is 449.716KPa and the final strain is 0.118%. Two main cracks developed on the left and right side of the opening, the right one developing towards lower left, and the other one developing towards upper right. The crack angle on the right side of the opening α_t was 29°, and the crack angle on the left side of the opening α_b was 9°.

The fourth group

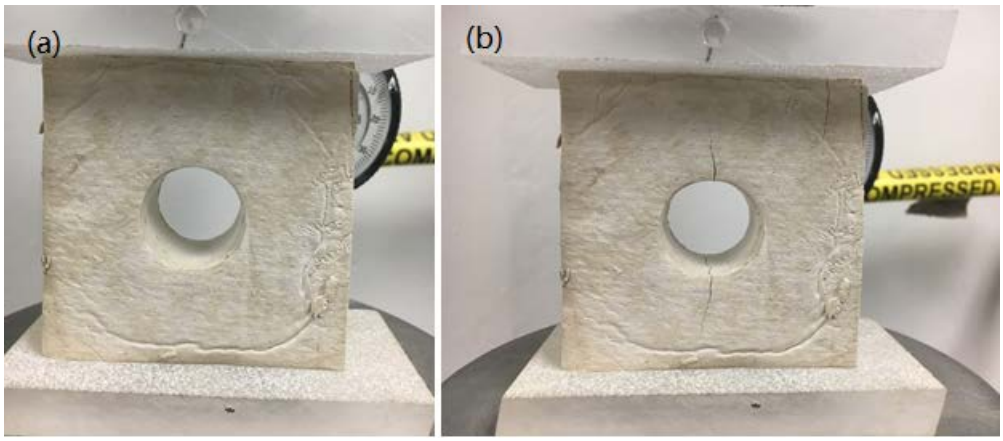

Figure 4.19 (a) the state of installation of circle 1, and (b) the state of failure of circle 1

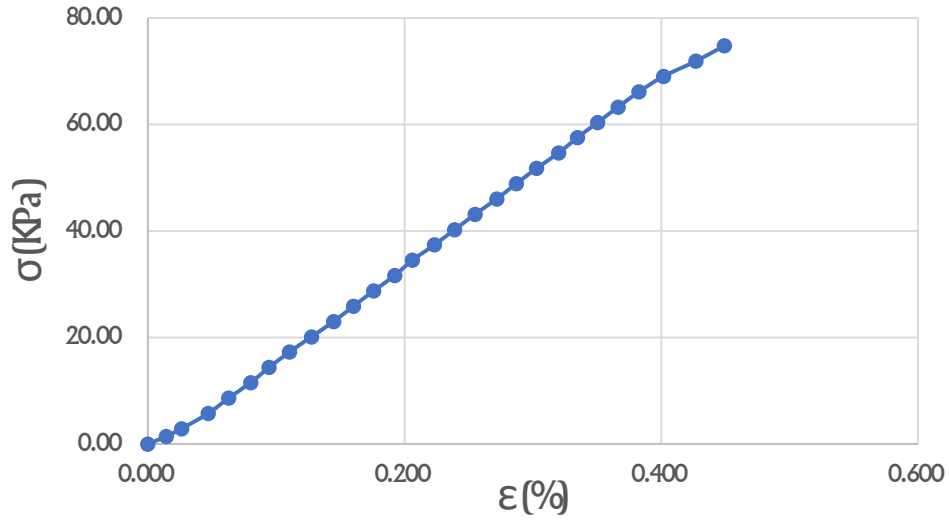

Figure 4.20 Stress-strain curve

As the figure above shows, the σ_{max} is 74.778KPa and the final strain is 0.499%. Two main cracks developed through the opening. The direction of the top one was towards upper left and the direction of the other one was towards lower left. The crack angle on the top of the opening α_t was 96°, and the crack angle on the bottom side of the opening α_b was 77°.

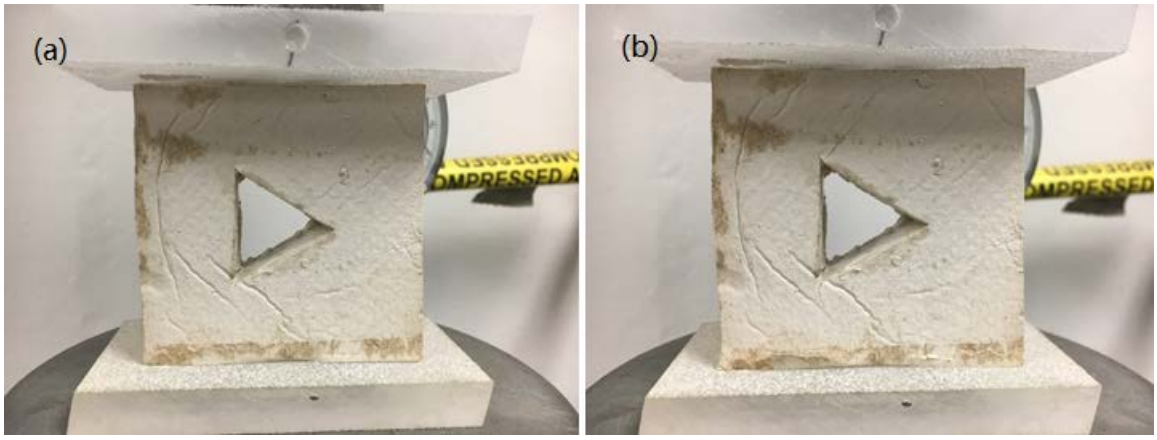

Figure 4.21 (a) the state of installation of triangle 1, and (b) the state of failure of triangle 1

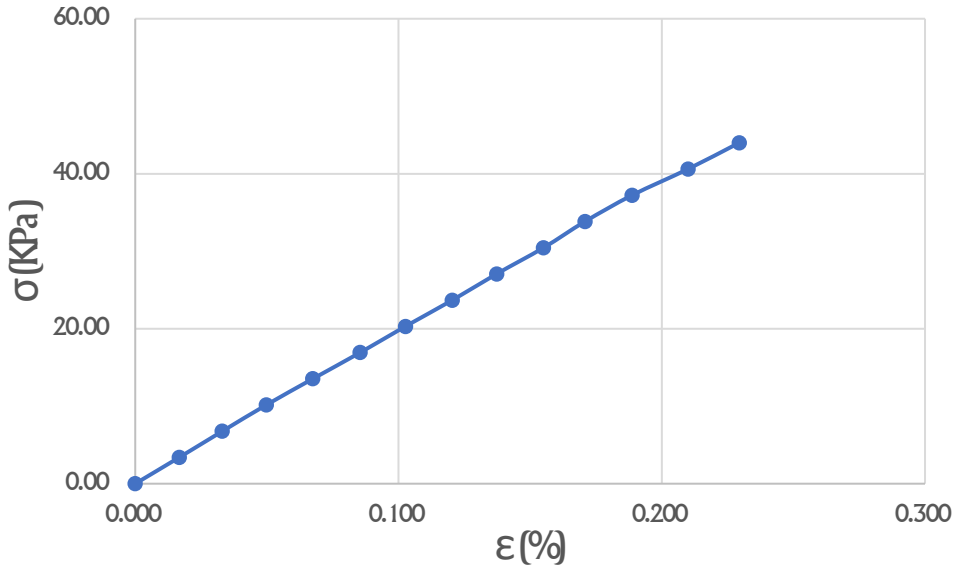

Figure 4.22 Stress-strain curve

In this figure, the σ_{max} is 43.987KPa, and the final strain is 0.229%. Two main cracks developed on the top and bottom toe of the triangle, the top one towards the upper right and the other crack towards the bottom right. The crack angle on the top of the opening α_t was 52°, and the crack angle on the bottom side of the opening α_b was 110°.

4.1.1.2 Analysis of samples by groups

Group #1

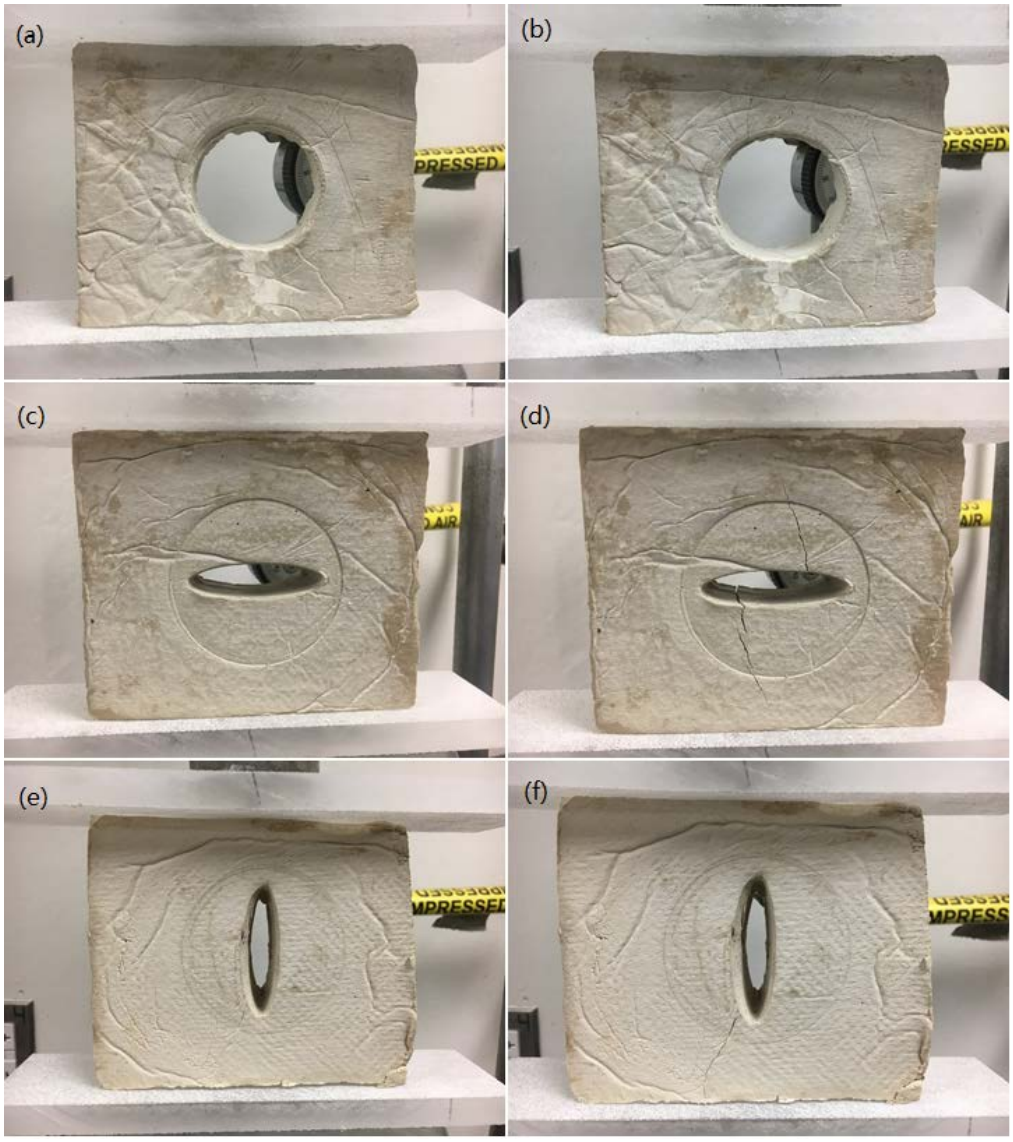

Figure 4.23 (a) the state of installation of circle 2, (b) the state of failure of circle 2 (c) the state of installation of ellipse 5, (d) the state of failure of ellipse 5, (e) the state of installation of ellipse 6, and (f) the state of failure of ellipse 6

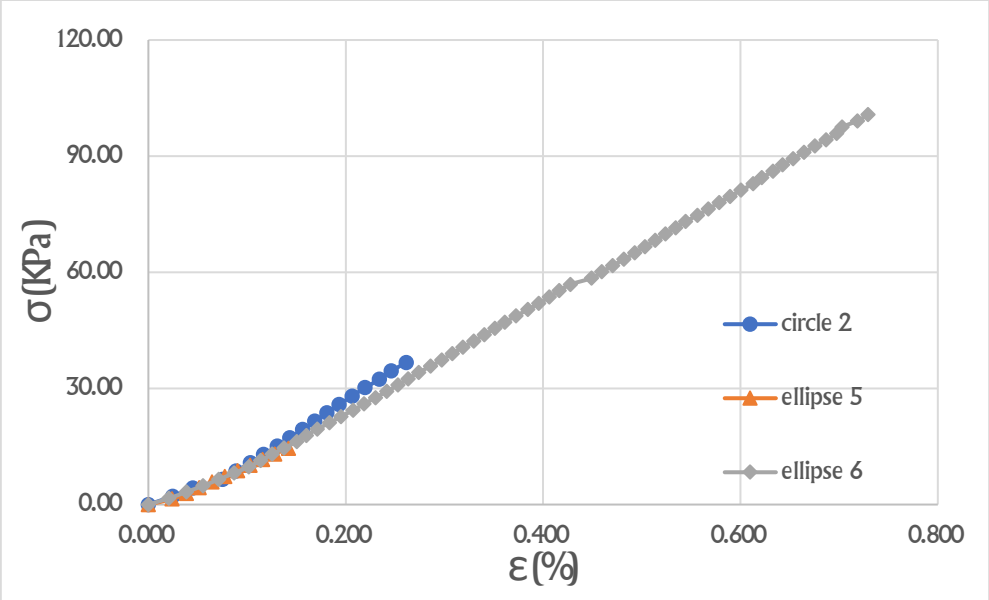

Figure 4.24 Stress-strain curve

In this figure, the σ_{max} of ellipse 5, circle 2 and ellipse 6 are 14.532KPa, 36.670Kpa and 100.744Kpa, respectively; the final strains ε_f are 0.142%, 0.262%, 0.729%, respectively. The differences in the σ_{max} and ε_f are significant: ellipse 5 had the lowest σ_{max} and ε_f, but ellipse 6 had the highest σ_{max} and ε_f. The ratio of height and width of the ellipse H/W of ellipse 5, circle 2 and ellipse 6 is 0.25, 1 and 4, respectively. These results show that when the H/W of the ellipse openings with the same major axis increases, the σ_{max} and ε_f of the clay samples increases as well. This indicates that the sample is more sustainable when its ellipse is the same major axis but with a higher H/W. In this case, the crack angle α_{b1} of ellipse 6 was 60° and it was located under the opening. The crack angle α_{t2} of the circle 1 was 81° and it was located above the opening. In ellipse 5, the crack angle on the top of the opening α_{t3} was 104°, and the angle on the bottom side of the opening α_{b3} is 110°. From these data, it can be concluded that the crack angle α of a crack

that starts at the opening will decrease as the H/W of the ellipse increases. The average water content was 11.8%, and the LEFM method applied well in this experiment.

Group #2

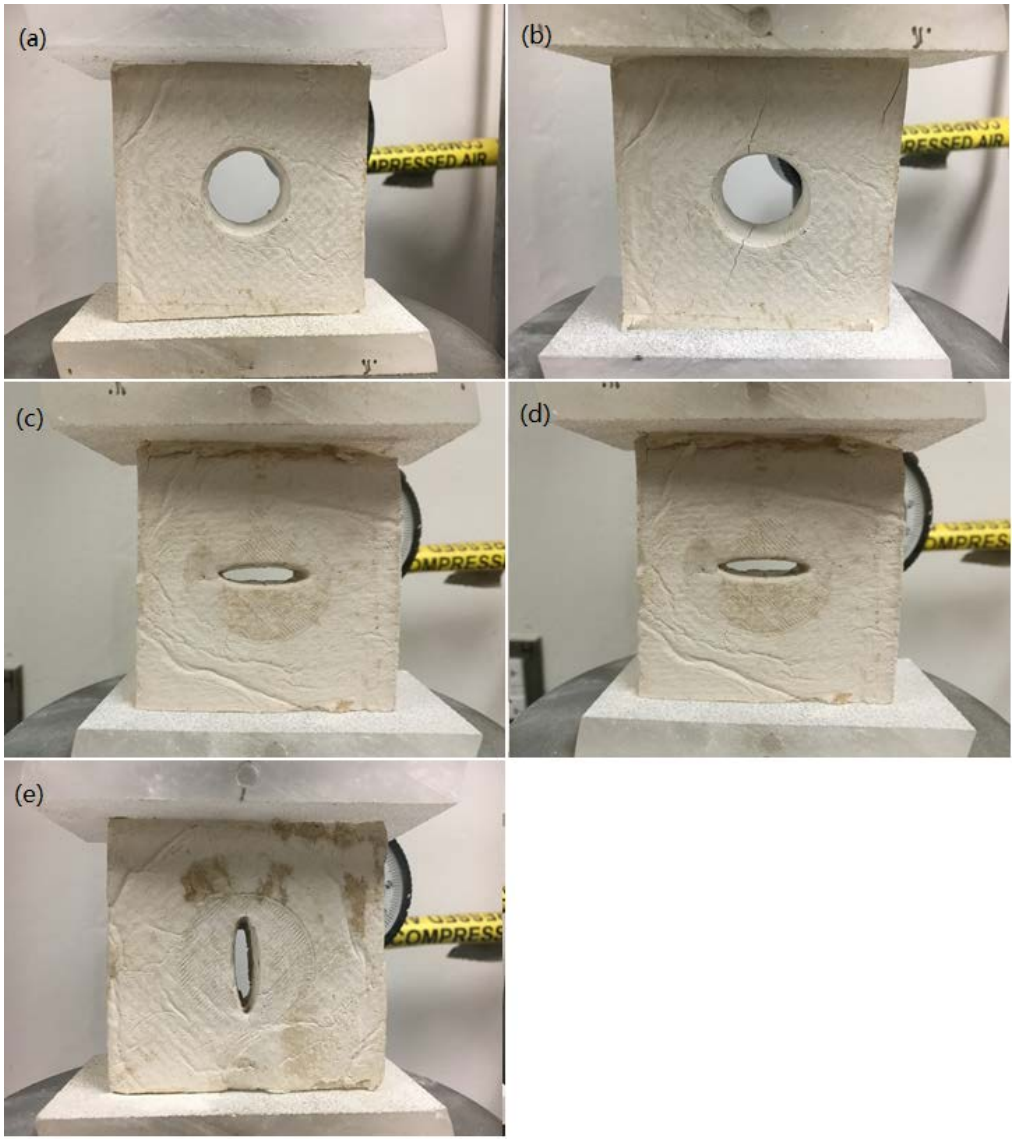

Figure 4.25 (a) the state of installation of circle 1, (b) the state of failure of circle 1, (c) the state of installation of ellipse 2, (d) the state of failure ellipse 2, (e) the state of installation of ellipse 4, and (f) the state of failure of ellipse 4

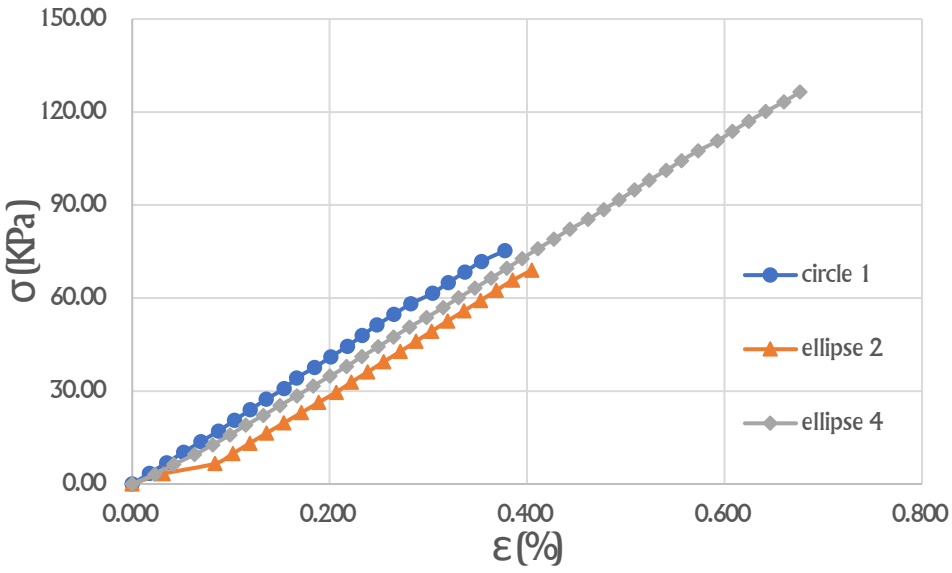

Figure 4.26 Stress-strain curve

As the figure above shows, the σ_{max} of ellipse 2, circle 1 and ellipse 4 in this test are 69.015KPa, 75.224Kpa and 126.462Kpa, respectively; the final strains ε_f are 0.405%, 0.377%, 0.676%, respectively. The differences in the σ_{max} are significant; the lowest σ_{max} occurred with the opening of ellipse 2, and the highest σ_{max} was found with the opening of ellipse 4. The height to width ration H/W of ellipse 2, circle 1 and ellipse 4 was 0.25, 1 and 4, respectively. These results indicate that when the H/W of the ellipse openings with the same major axis increases, the σ_{max} and ε_f of the clay samples increases as well. This shows that the sample is more sustainable when its ellipse is the same major axis but with a higher H/W. With the sample for circle 1, there were two cracks, the crack angle on the top of the opening α_{t1} was 76°, and the angle on the bottom side of the opening α_{b1} was 70°. With sample labeled ellipse 2, there were also two cracks, the crack angle on the top of the opening α_{t2} was 96°, and the angle under the opening α_{b2} was 80°. Due to the absence of data about ellipse 4, this trend of the crack angle is not very obvious; however, based on earlier tests, the assumption is that as the H/W of the ellipse opening increases, the angle

of the crack decreases. The average water content was 5.8%, and the LEFM method applied well in this experiment.

Group #3

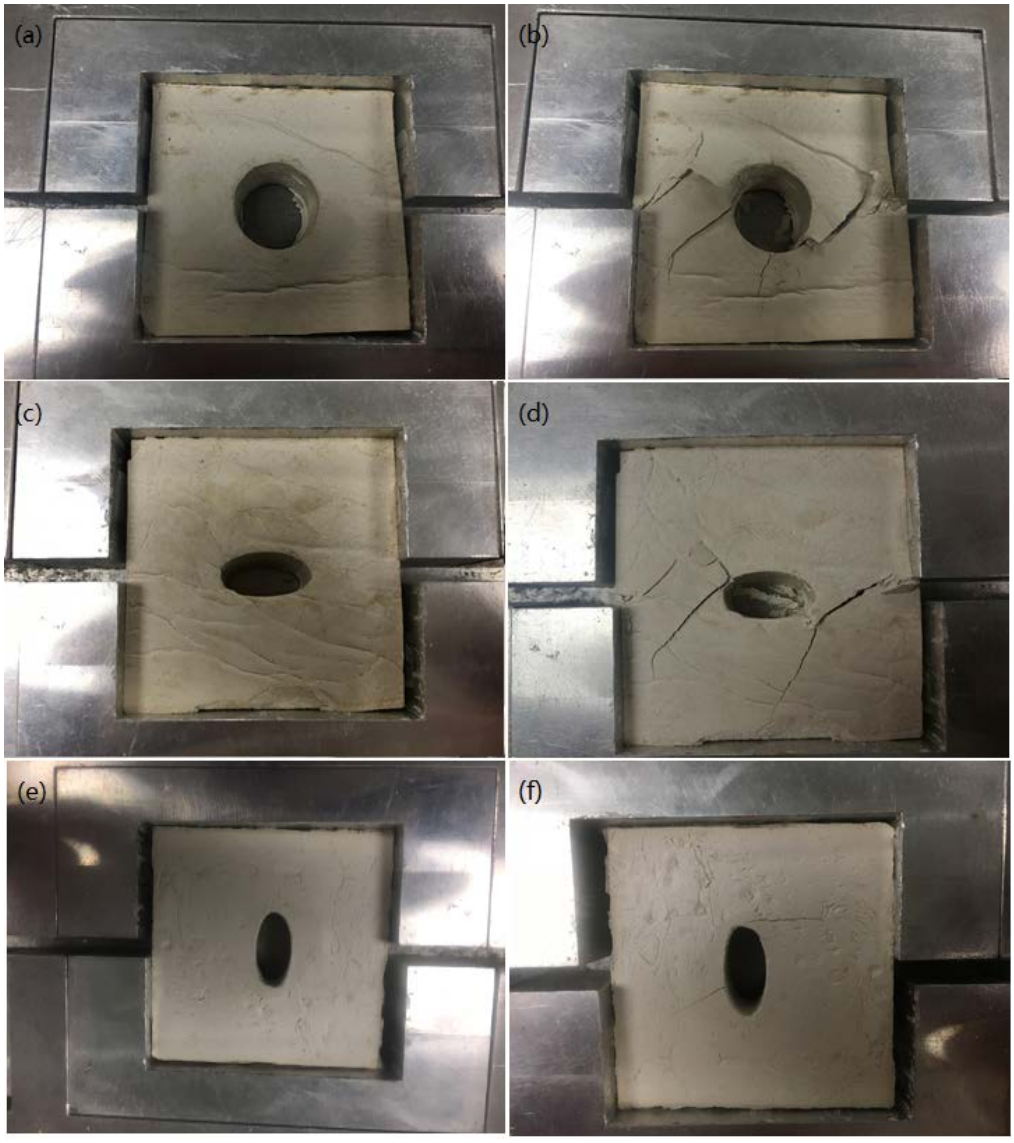

Figure 4.27 (a) the state of installation of circle 1, (b) the state of failure of circle 1, (c) the state of installation of ellipse 1, (d) the state of failure of ellipse 1, (e) the state of installation of ellipse 3, and (f) the state of failure of ellipse 3

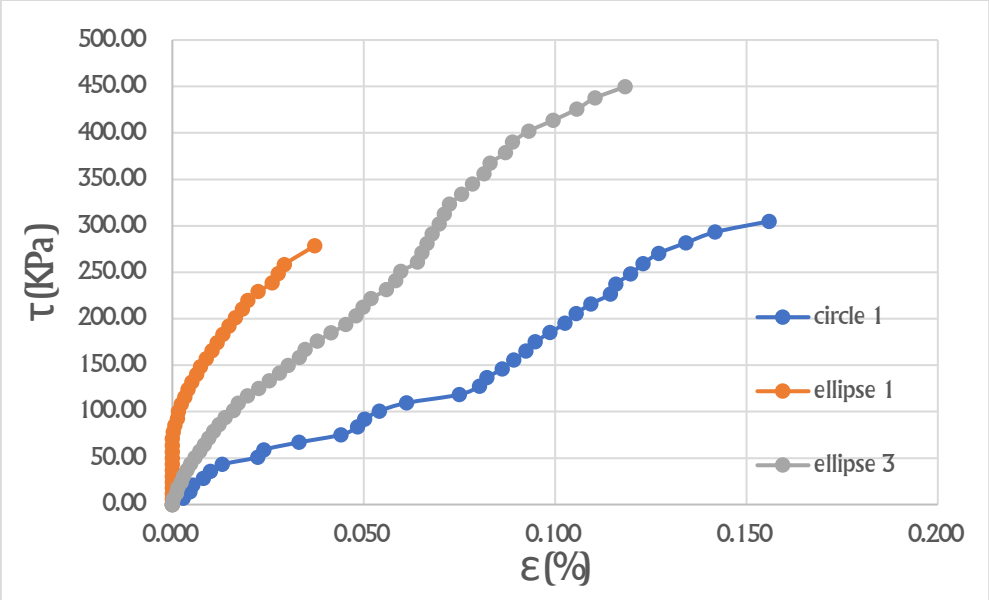

Figure 4.28 Stress-strain curve

In this figure, the τ_{max} of ellipse 1, circle 1 and ellipse 3 in this test are 278.473KPa, 304.895Kpa and 449.716Kpa, respectively, and the final strains ε_f are 0.037%, 0.156%, and 0.118%, respectively. These results show that ellipse 1 has the lowest τ_{max} and ellipse 3 has the highest τ_{max}. The ratios of height and width H/W of ellipse 1, circle 1 and ellipse 3 is 0.5, 1 and 2, respectively. From these results, it can be concluded that when the H/W of the ellipse openings with the same major axis increases, the τ_{max} of the clay samples will increase as well. This means that a sample can better withstand shear stress when the ellipse has a higher H/W. In the case of ellipse 1, two cracks developed beside it, the angle of the crack on the right of the opening α_r was 45°, and the angle of the crack on the left side of the opening α_l was 51°. In circle 1, the crack angle on the right of the opening α_{r2} was 36°, and the angle on the left side of the opening α_{l2} was 41°. In ellipse 3, the crack angle on the right of the opening α_{r3} was 29°, the angle on the left side of the opening α_{l3} was 9°. Which shows that the crack angle will decrease as the H/W of the

ellipse opening increases. The average water content was 7.9%, although in Fig.4.28 the lines were not very straight, the LEFM method still applied in this experiment

Group #4

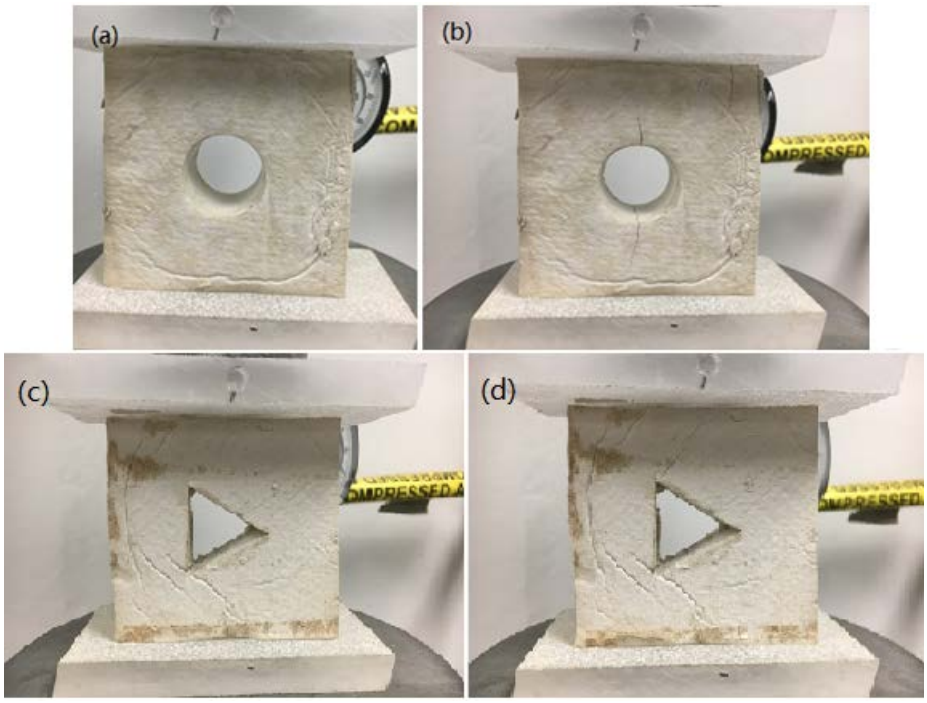

Figure 4.29 (a) the state of installation of circle 1, (b) the state of failure of circle 1, (c) the state of installation of triangle 1, and (d) the state of failure of triangle 1

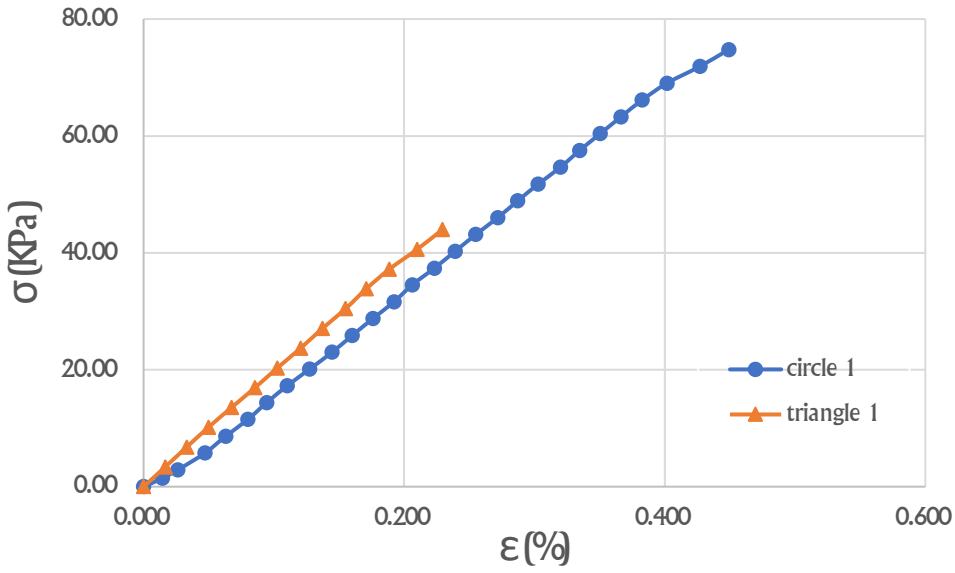

Figure 4.30 Stress-strain curve

In the figure above, the σ_{max} of triangle 1 and circle 1 in this test are 43.987KPa, 74.778Kpa, respectively, and the final strains ε_f are 0.229%, 0.499%, respectively. The differences in the σ_{max} are obvious: the σ_{max} of circle 1 is larger than the σ_{max} of triangle 1. These results suggest that samples with a circular opening are firmer than samples with a triangle opening. When the opening is circular, the secondary cracks developing from the opening tend to be parallel, but when the opening is triangular, the secondary cracks that develop tend to be symmetric. The average water content was 9.9%, and s the LEFM method applied well in this experiment.

4.1.2 Analysis of samples simulating vertical slopes with a notch

In this section., following the process introduced in third section, data regarding the maximum of normal stress σ_{max} and the angle of the secondary crack α in samples was collected. In order to analyze the results of these samples, the results are grouped into several sets to enable easier

comparison. After comparing the maximum of normal stress σ_{max} and the angles of the secondary crack α for samples with different angles of notch, we can discern trends in how the angle of the notch effects the angle of the secondary crack.

During the test, the angle of the secondary crack propagation is defined as the angle between the final crack propagation and the crack plane. The whole crack expansion phase can be divided into three parts: the crack initiation, the crack growth, and the crack propagation. For initial crack opening, β is 30°, 45° and 60°, respectively. In these cases, variety of the crack plane is taken into consideration. For the standard notch with 0°opening, the crack plane is considered horizontal; furthermore, when the initial crack has an angle of β, then the crack plane is defined as the angular bisector of the two crack faces. Hence, the final crack propagation angle, α should be the initial secondary crack propagation angle, α_i plus $\beta/2$.

4.1.2.1 Description of each sample

The first group

Figure 4.31 (a) the state of installation, and (b) the state of failure

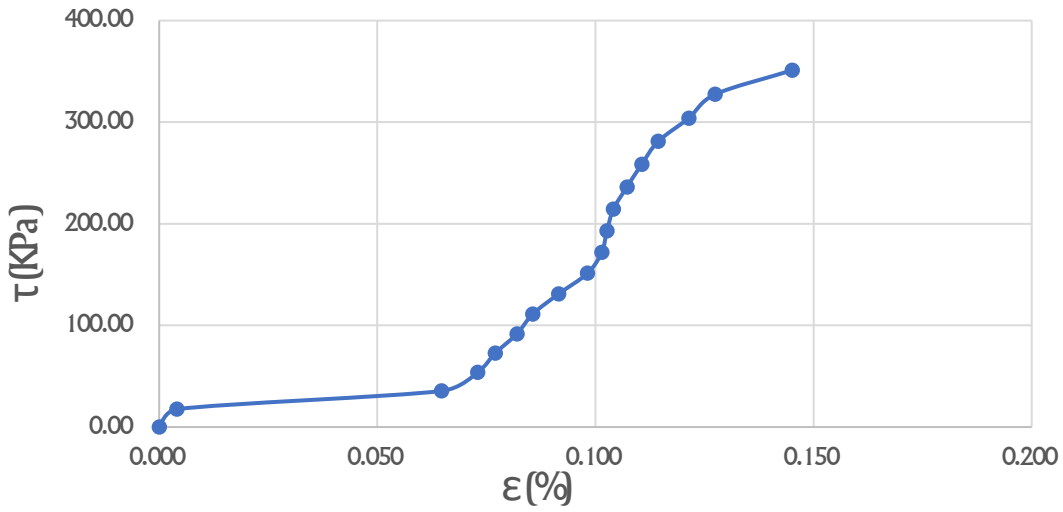

Figure 4.32 Stress-strain curve

In this figure, the τ_{max} is 351.145KPa, σ is 154.059Kpa and the final strain is 0.145%. This sample had a notch of 30°. A crack developed in the toe of the sample and other two cracks occurred in the bottom area of the semi-prismatic clay samples. The toe crack, the research object, developed towards the upper right, and had a crack angle α_T of 87°. In this test, the reason that the toe crack, rather than two other cracks, was taken into consideration was that with coastal slope, in natural conditions, the right side and bottom side of the slope are generally considered as infinite regions, therefore, the toe crack is supposed to be the main crack that causes the failure of a slope.

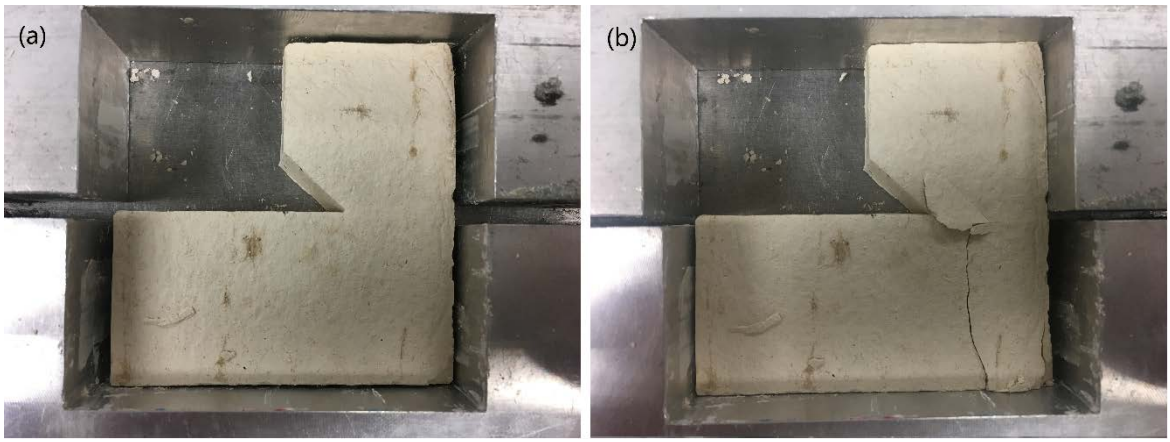

Figure 4.33 (a) the state of installation, and (b) the state of failure

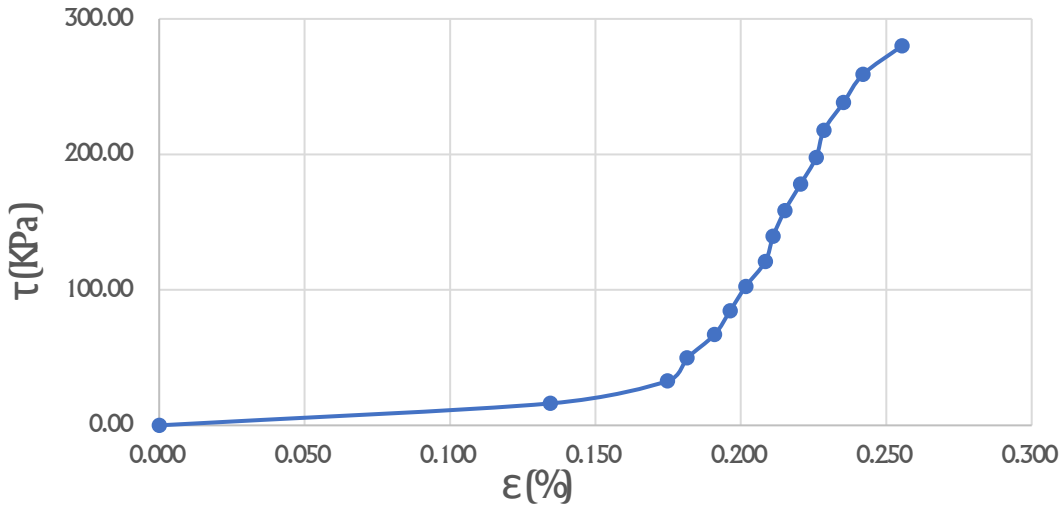

Figure 4.34 Stress-strain curve

In this figure, the τ_{max} is 280.154KPa, σ is 149.440Kpa and the final strain is 0.255%. This sample had a notch of 45°. A crack developed in the toe of the sample towards the upper right section, and the crack angle α_T was 135°. Although other two cracks developed in the lower section of the toe, they were ignored for reasons mentioned before: in nature conditions, the toe crack is supposed to be the main crack that causes the failure.

Figure 4.35 (a) the state of installation, and (b) the state of failure

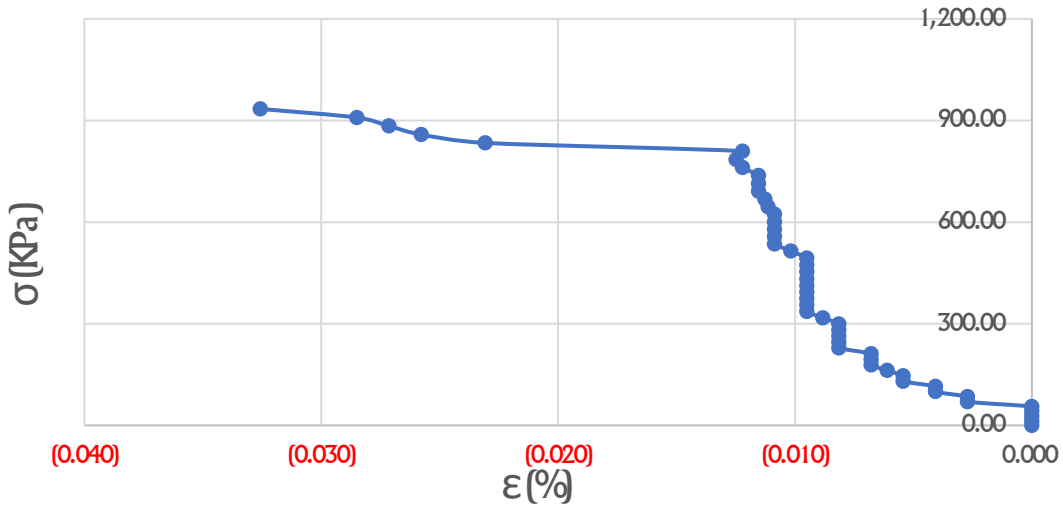

Figure 4.36 Stress-strain curve

In this figure, the σ_{max} is 934.288KPa, τ is 15.984KPa and the final strain is -0.033%. This sample had a notch of 45°. A crack developed in the toe of the sample and moved towards the left upper; the crack angle α_T was 86°. Although other two cracks developed in the lower right of the toe, they were ignored for reasons mentioned earlier. The reason why the data in this test was abnormal is that the displacement that was measured in this test was horizontal displacement, but

the force added is vertical pressure, so the vertical pressure had little effect on the horizontal displacement.

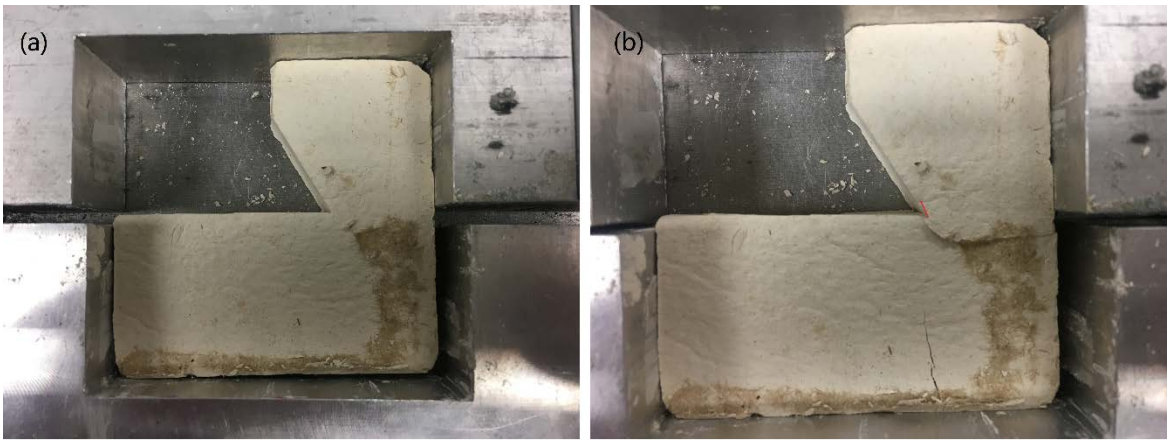

Figure 4.37 (a) the state of installation, and (b) the state of failure

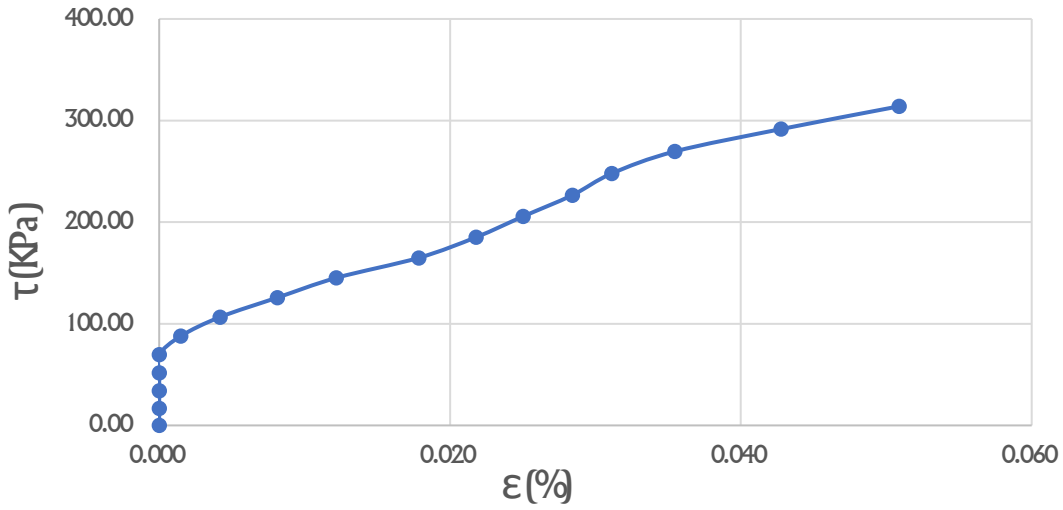

Figure 4.38 Stress-strain curve

In this figure, the τ_{max} is 314.020KPa, σ is 156.256Kpa and the final strain is 0.051%. This sample had a notch of 60°. A crack developed in the toe of the sample and other two cracks occurred in the right and bottom area of the sample. The toe crack, which was the research object,

developed in the upper right section. The crack angle α_T was 144°. The reason why the other two cracks were not considered is described in the first example.

Figure 4.39 (a) the state of installation, and (b) the state of failure

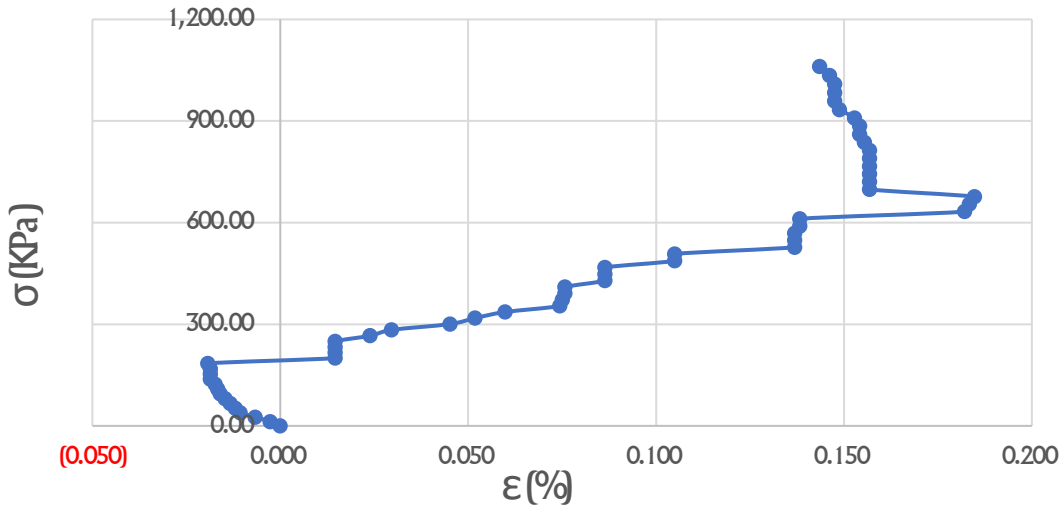

Figure 4.40 Stress-strain curve

In this figure, the σ_{max} is 1060.727KPa, τ is 15.464KPa and the final strain is 0.144%. This sample had a notch of 60°. There was a crack developing in the toe of the sample, and it moved towards the upper left; the crack angle α_T was 94°. Although other two cracks developed, in the

lower right part of the sample, they were ignored for reasons described before. And why the abnormal data occurred was mentioned before.

The second group

Figure 4.41 (a) the state of installation, and (b) the state of failure

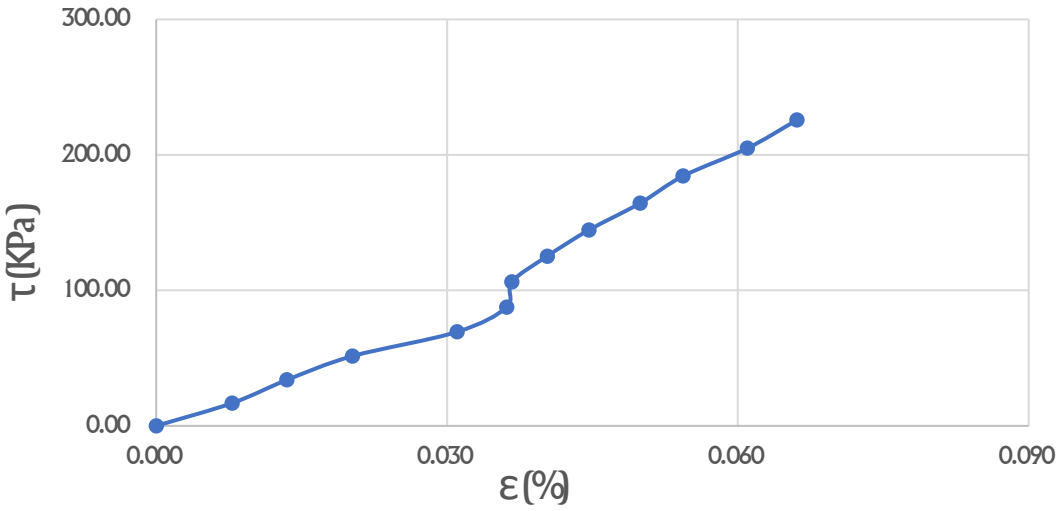

Figure 4.42 Stress-strain curve

As the figure shows, the τ_{max} is 225.694KPa, σ is 152.745Kpa and the final strain is 0.067%. This sample had a notch of 30°. Two cracks developed in the toe of this sample, one towards the upper left and one horizontal. The right upper crack was the focus of research, and the crack angle α_T was 116°. The reason for not considering the other cracks was described above.

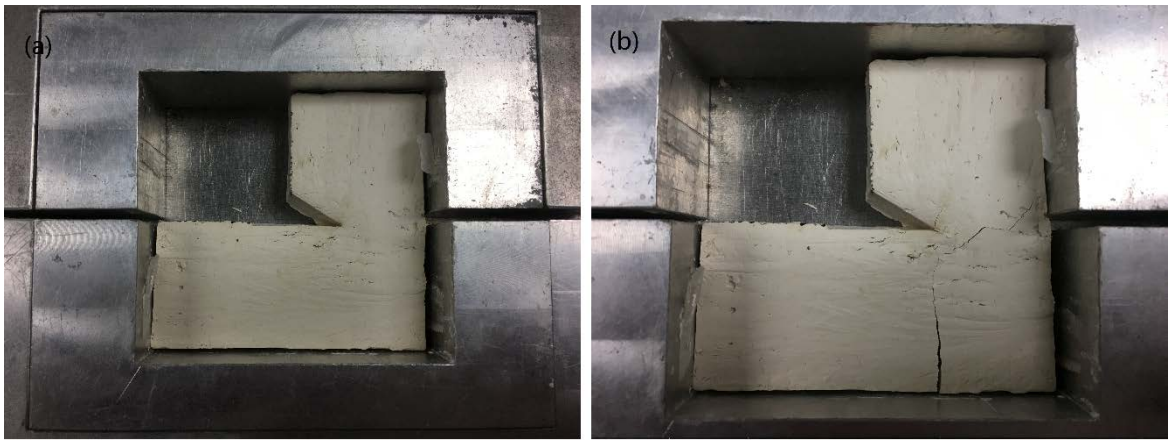

Figure 4.43 (a) the state of installation, and (b) the state of failure

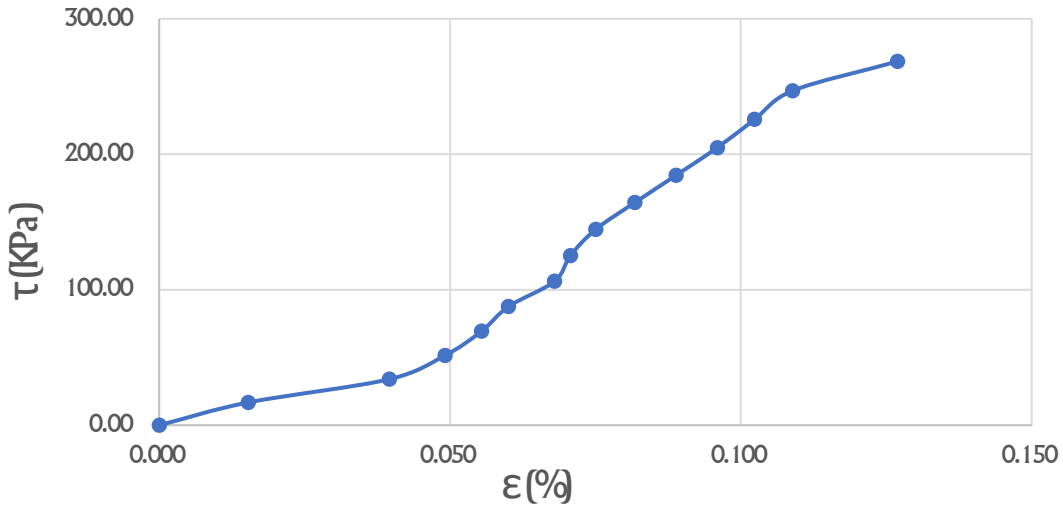

Figure 4.44 Stress-strain curve

In this figure, τ_{max} is 268.463KPa, σ is 147.693Kpa and the final strain is 0.127%. This sample had a notch of 30°. A crack developed in the toe of the sample and moved towards the left upper; the crack angle α_T was 113°. Although two other cracks developed in the lower right part of the sample, they were not considered for reasons described before.

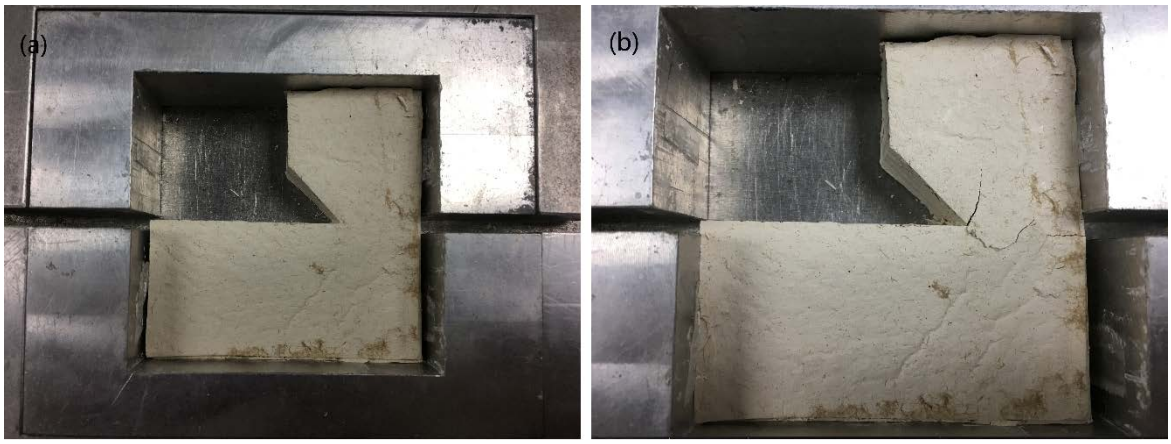

Figure 4.45 (a) the state of installation, and (b) the state of failure

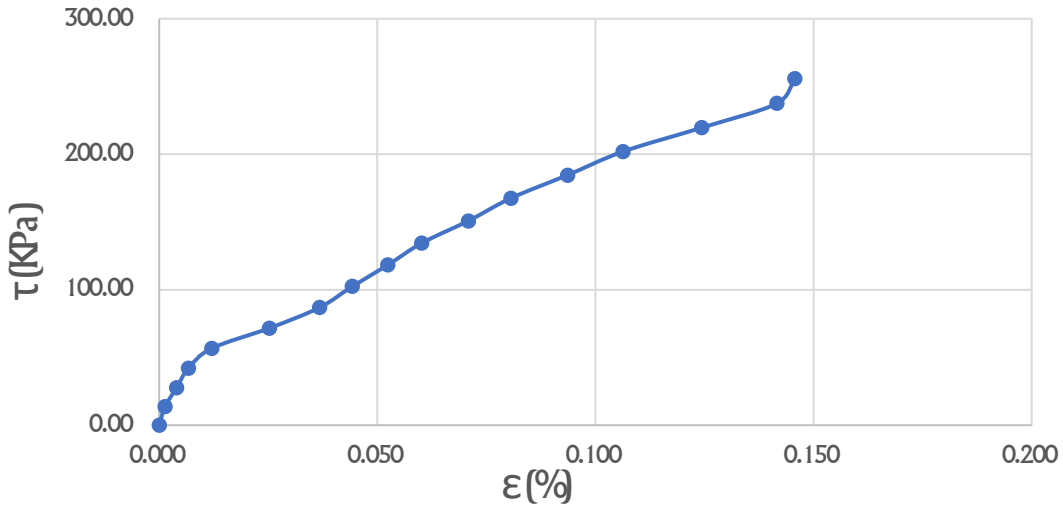

Figure 4.46 Stress-strain curve

In this figure, the τ_{max} is 255.755KPa, σ is 130.393Kpa and the final strain is 0.146%. This sample had a notch of 45°. A crack developed in the notch of the sample and moved in an upper-right direction; the crack angle α_T was 81°. Another crack developing in the right side of the toe but was not considered for reasons mentioned before.

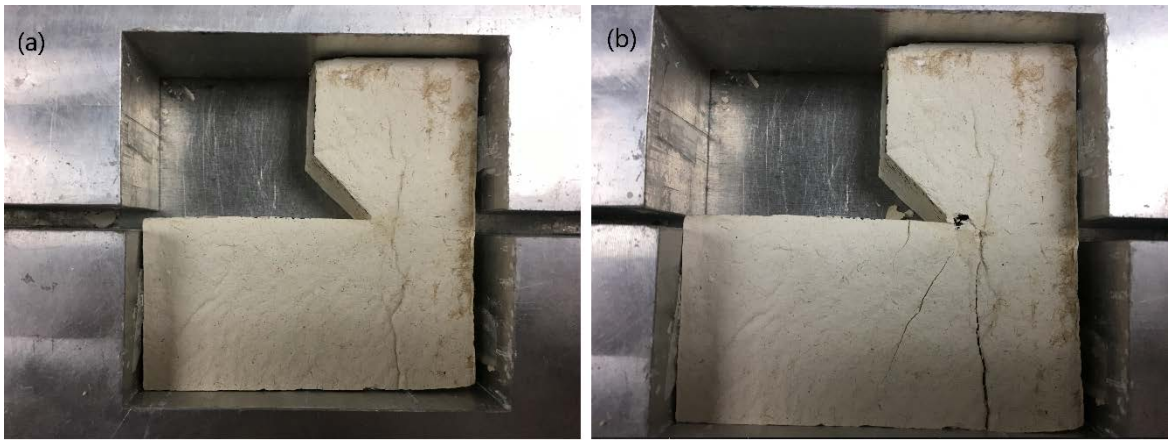

Figure 4.47 (a) the state of installation, and (b) the state of failure

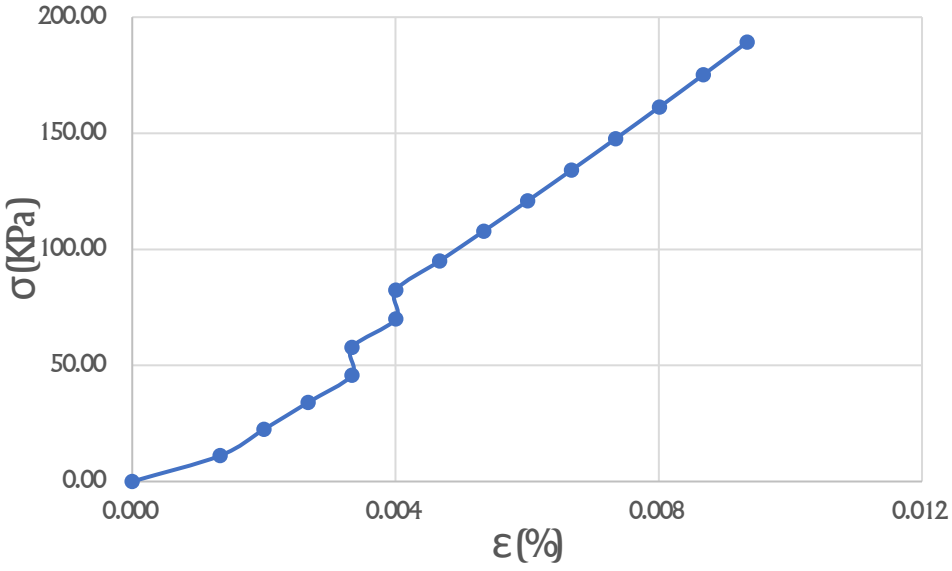

Figure 4.48 Stress-strain curve

In this figure, the σ_{max} is 189.292KPa, τ is 13.366KPa and the final strain is 0.009%. This sample had a notch of 45°. A crack developed in the toe of the sample and moved towards right upper; the crack angle α_T is 88°. Although other two cracks developed at the lower right part of the sample, they were not considered for reasons mentioned before. The reason why the strain was abnormally small may have been caused by the unevenness of the surface between the sample and the steel frame.

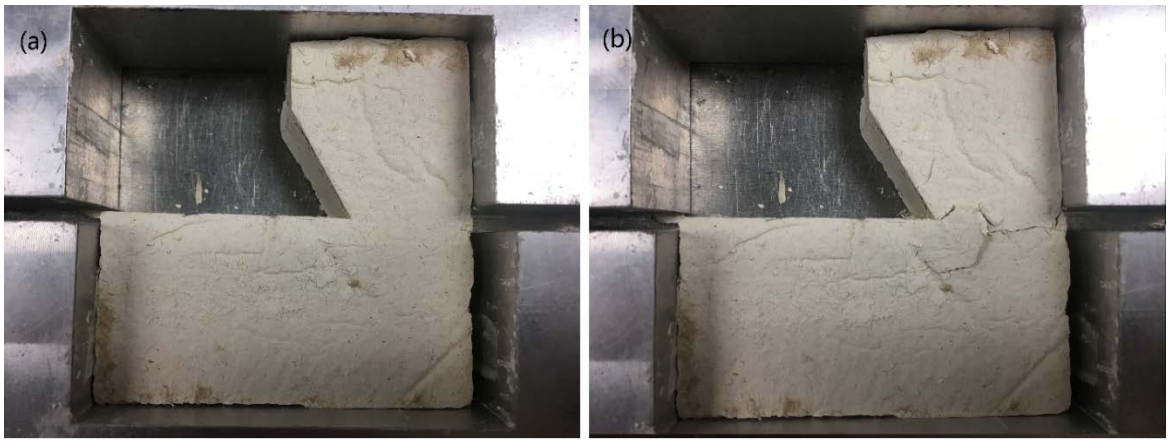

Figure 4.49 (a) the state of installation, and (b) the state of failure

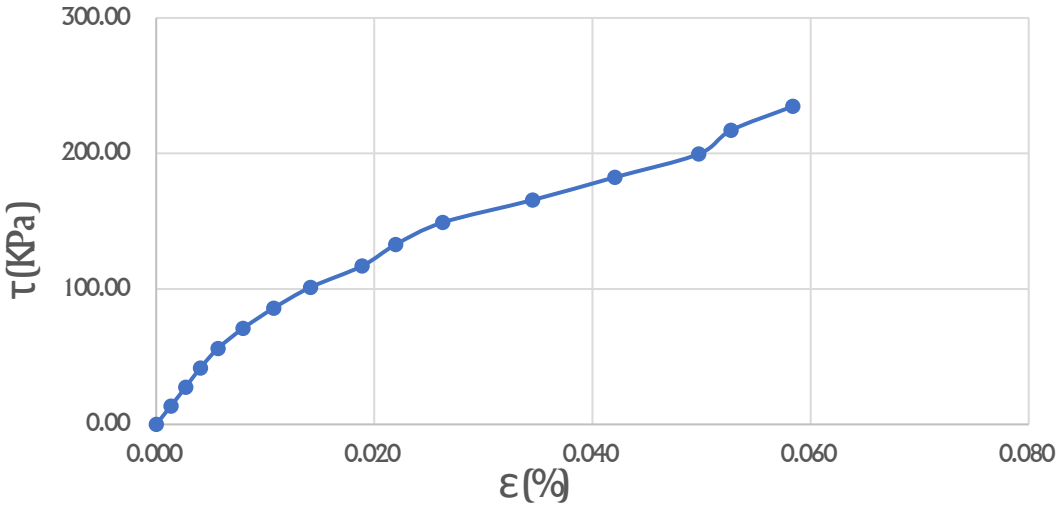

Figure 4.50 Stress-strain curve

In this figure, the τ_{max} is 234.694KPa, σ is 124.150Kpa and the final strain is 0.058%. This sample had a notch of 60°. A crack developed in the notch of the sample and moved towards upper right; the crack angle α_T was 72°. Another crack developed on the right side of the toe but was not considered for reasons mentioned before.

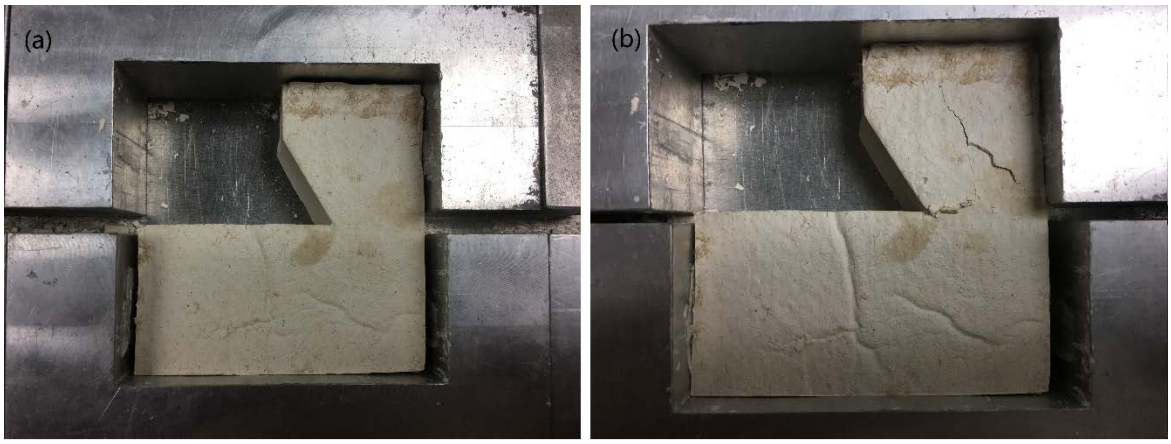

Figure 4.51 (a) the state of installation, and (b) the state of failure

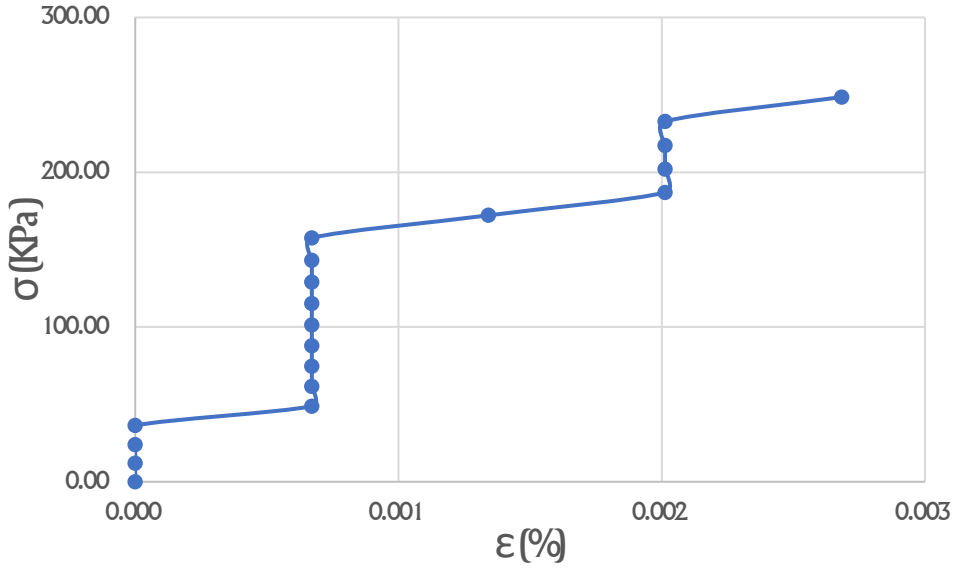

Figure 4.52 Stress-strain curve

In this figure, the σ_{max} is 248.545KPa, τ is 12.843Kpa and the final strain is 0.003%. This sample had a notch of 60°. A crack developed in the toe of the sample and moved towards right upper, the crack angle α_T is 79°. Although another crack developed at the right side of the notch, the reason that it was not considered is mentioned before. And the reason why the strain is abnormally small is also described earlier.

The third group

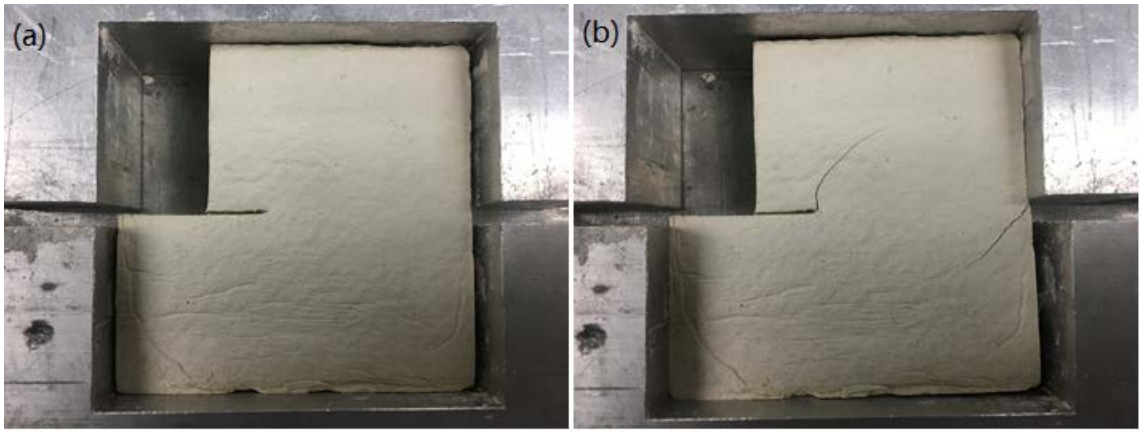

Figure 4.53 (a) the state of installation, and (b) the state of failure

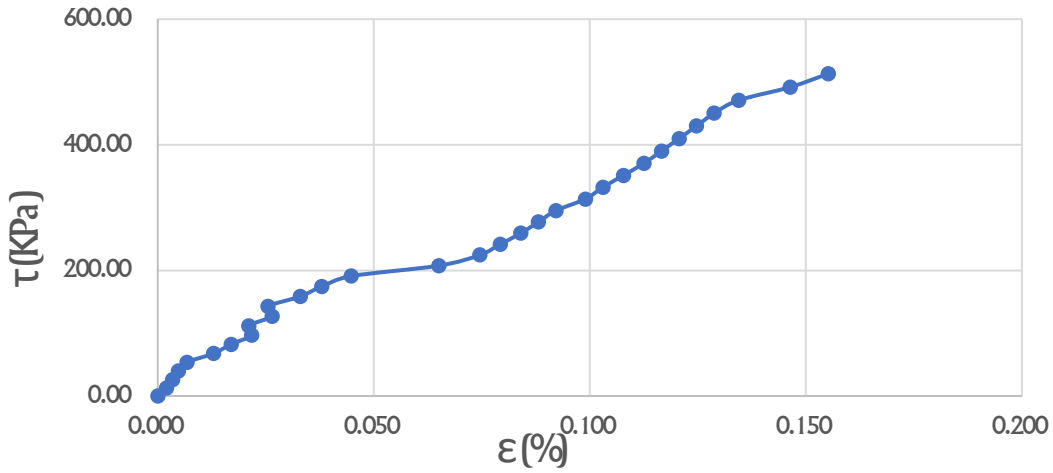

Figure 4.54 Stress-strain curve

In this figure, the τ_{max} is 513.049KPa, σ is 81.654Kpa and the final strain is 0.155%. This sample had a notch with 0° and a crack developed from it towards right upper and the crack angle α_T is 89°. Other cracks on the edge of sample were caused by the edge effect.

Figure 4.55 (a) the state of installation, and (b) the state of failure

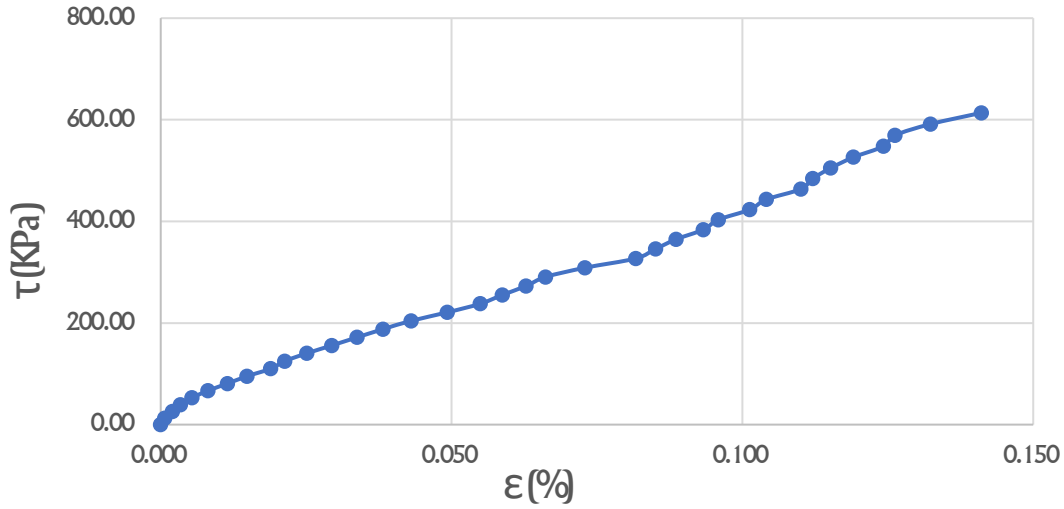

Figure 4.56 Stress-strain curve

In this figure, the τ_{max} is 613.806KPa, σ is 79.901Kpa and the final strain is 0.141%. This sample had a notch of 30° from which a crack developed to the upper right; the crack angle α_T

was 78°. Although another crack developed at the right side of the notch, the reason that it was not considered is mentioned before.

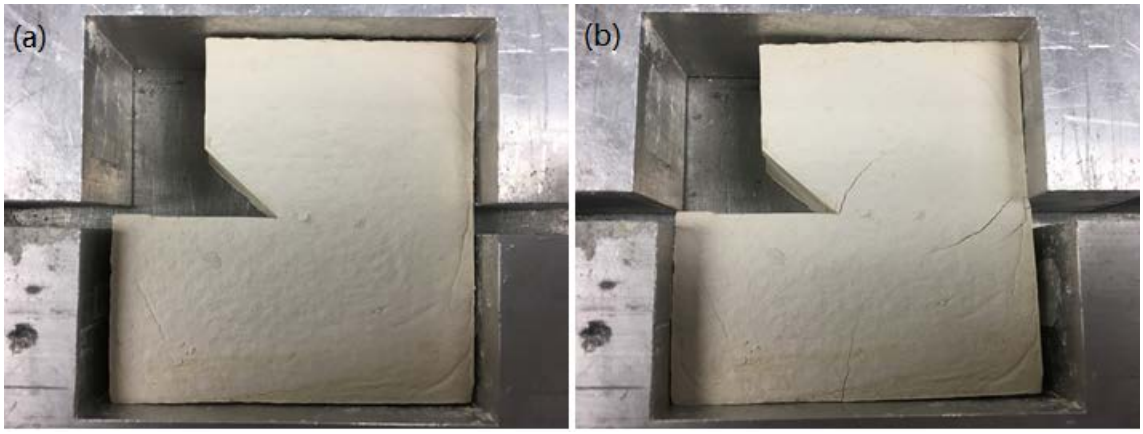

Figure 4.57 (a) the state of installation, and (b) the state of failure

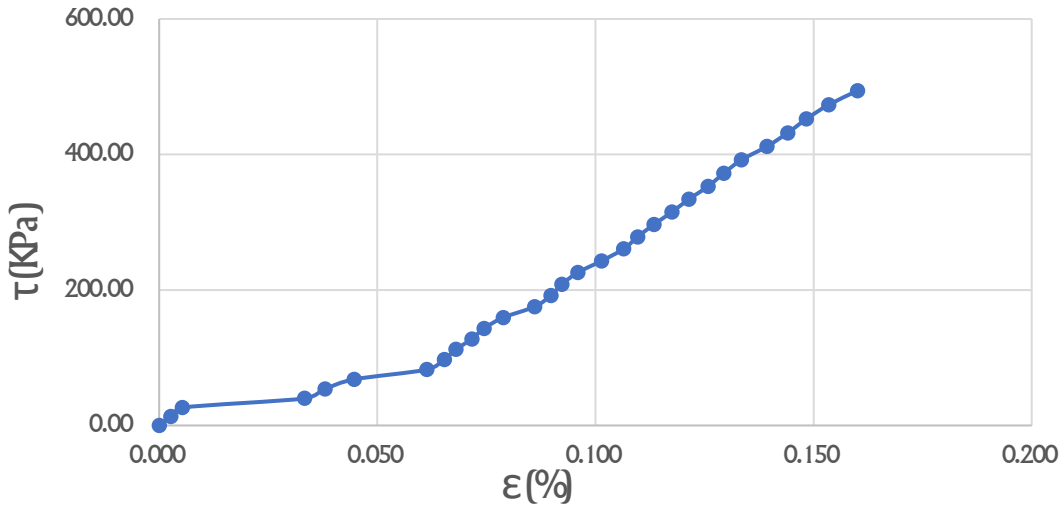

Figure 4.58 Stress-strain curve

In this figure, the τ_{max} is 494.299KPa, σ is 81.071Kpa and the final strain is 0.160%. This sample had a notch of 45° from which a crack developed towards upper right; the crack angle α_T was 93°. Other cracks on the edge of sample were caused by the edge effect.

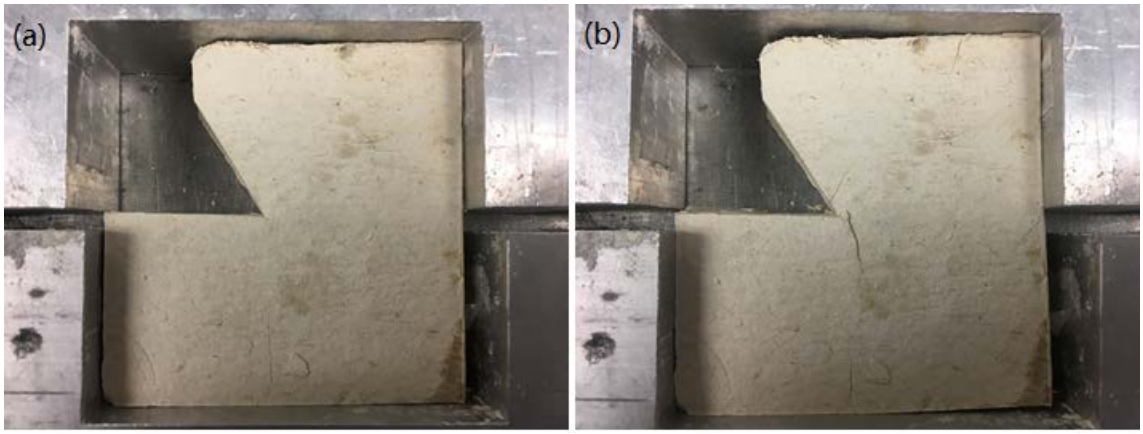

Figure 4.59 (a) the state of installation, and (b) the state of failure

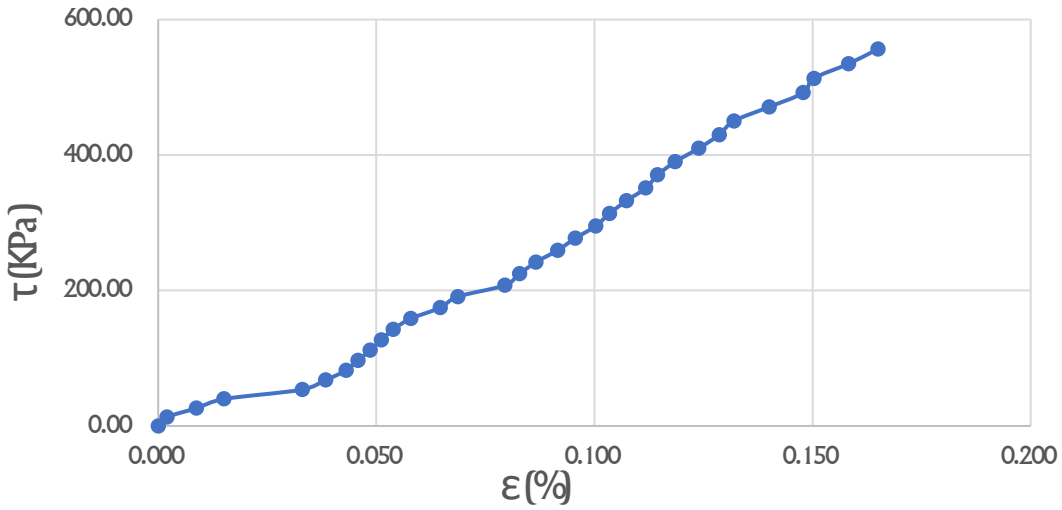

Figure 4.60 Stress-strain curve

In this figure, the τ_{max} is 556.358KPa, σ is 78.128Kpa and the final strain is 0.165%. This sample had a notch of 60° from which a crack developed towards upper right; the crack angle α_T was 103°. Another crack developing in the right side of the toe but was not considered for reasons mentioned before.

4.1.2.2 Comparing in groups

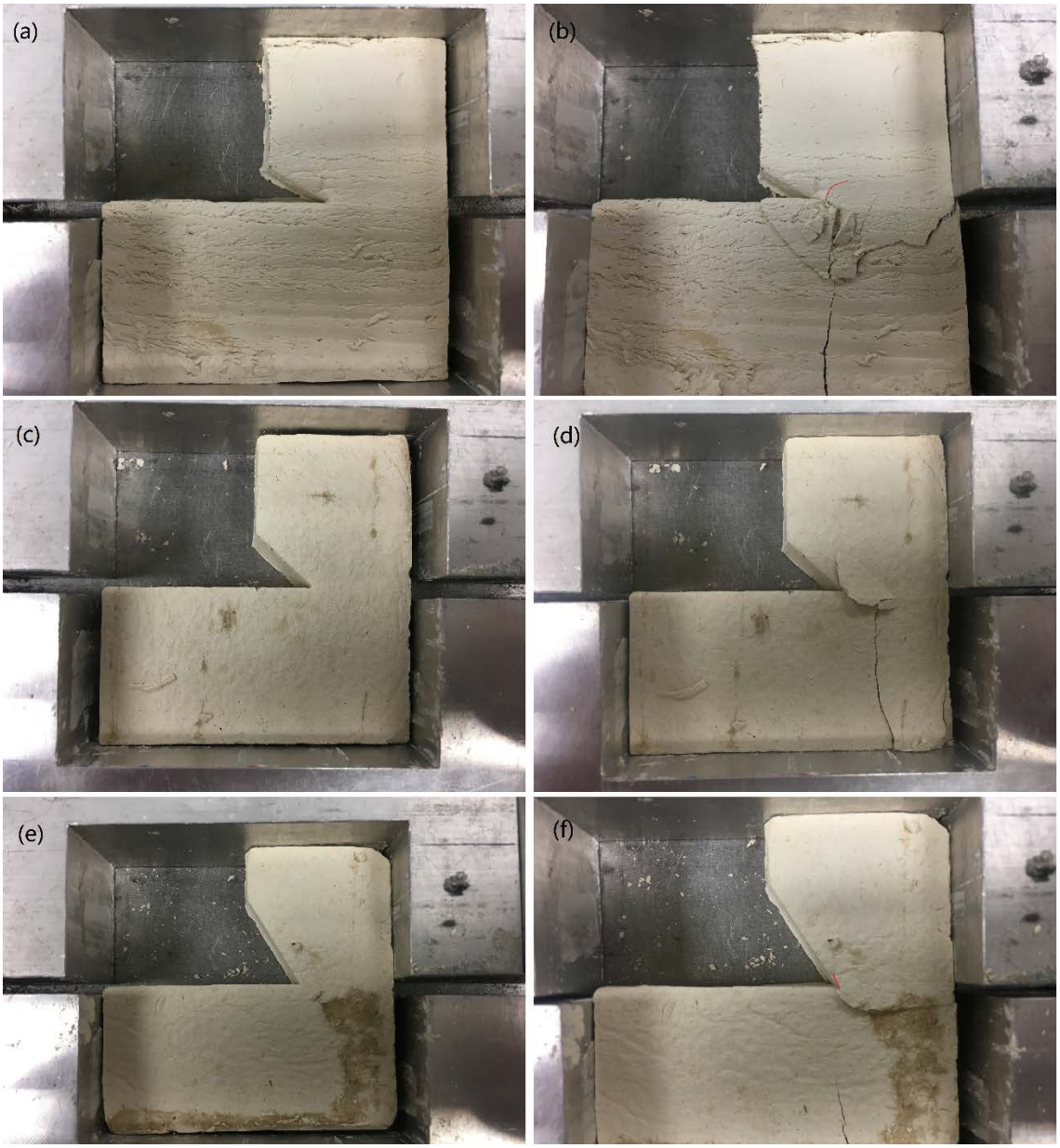

Figure 4.61 (a) the state of installation of notch of **30°**, (b) the state of failure of notch of **30°**, (c) the state of installation of notch of **45°**, (b) the state of failure of notch of **45°**, (e) the state of installation of notch of **60°**, and (f) the state of failure of notch of **60°**

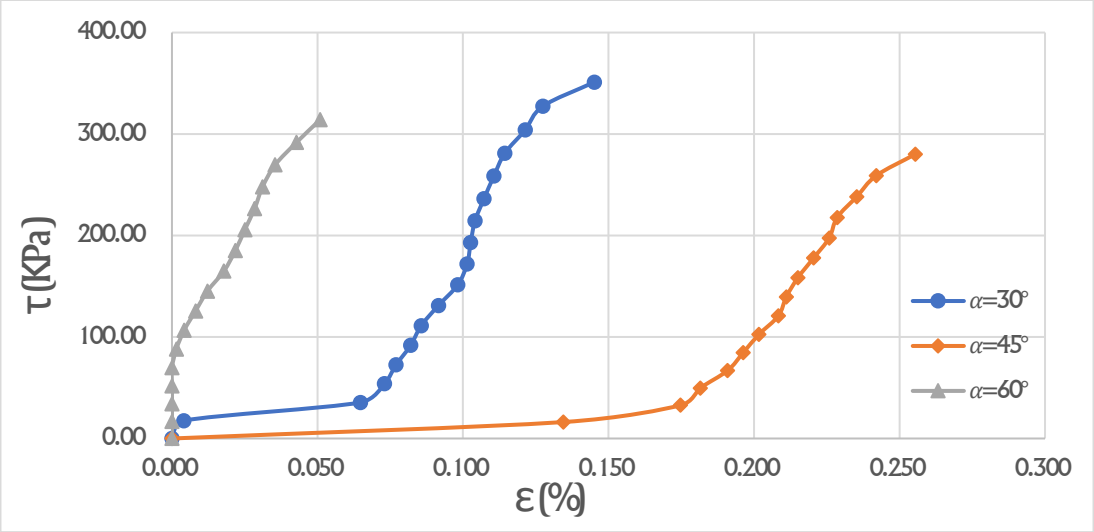

Figure 4.62 Stress-strain curve

In this figure, the τ_{max} of the notch of 30°, 45° and 60° in this test are 351.145KPa, 280.154Kpa and 314.020Kpa, respectively, the σ are 154.059KPa, 149.440Kpa and 156.256Kpa, respectively, and the final strains ε_f are 0.145%, 0.255%, 0.051%, respectively. These results show no obvious change in the rend of τ_{max} and ε_f. The sample with a notch of 30° had a crack in the toe that moved towards upper right and a crack angle α_{r1} of 87°. The sample with a notch of 45° had a crack in the toe that moved towards the upper right and the crack angle α_{r2} was 135°. The sample with a notch of 60° had a crack in the toe with a crack angle α_{r3} of 144°. These data show that when the angle of the notch increases, the angle of the secondary crack developing from the toe of the notch increases.

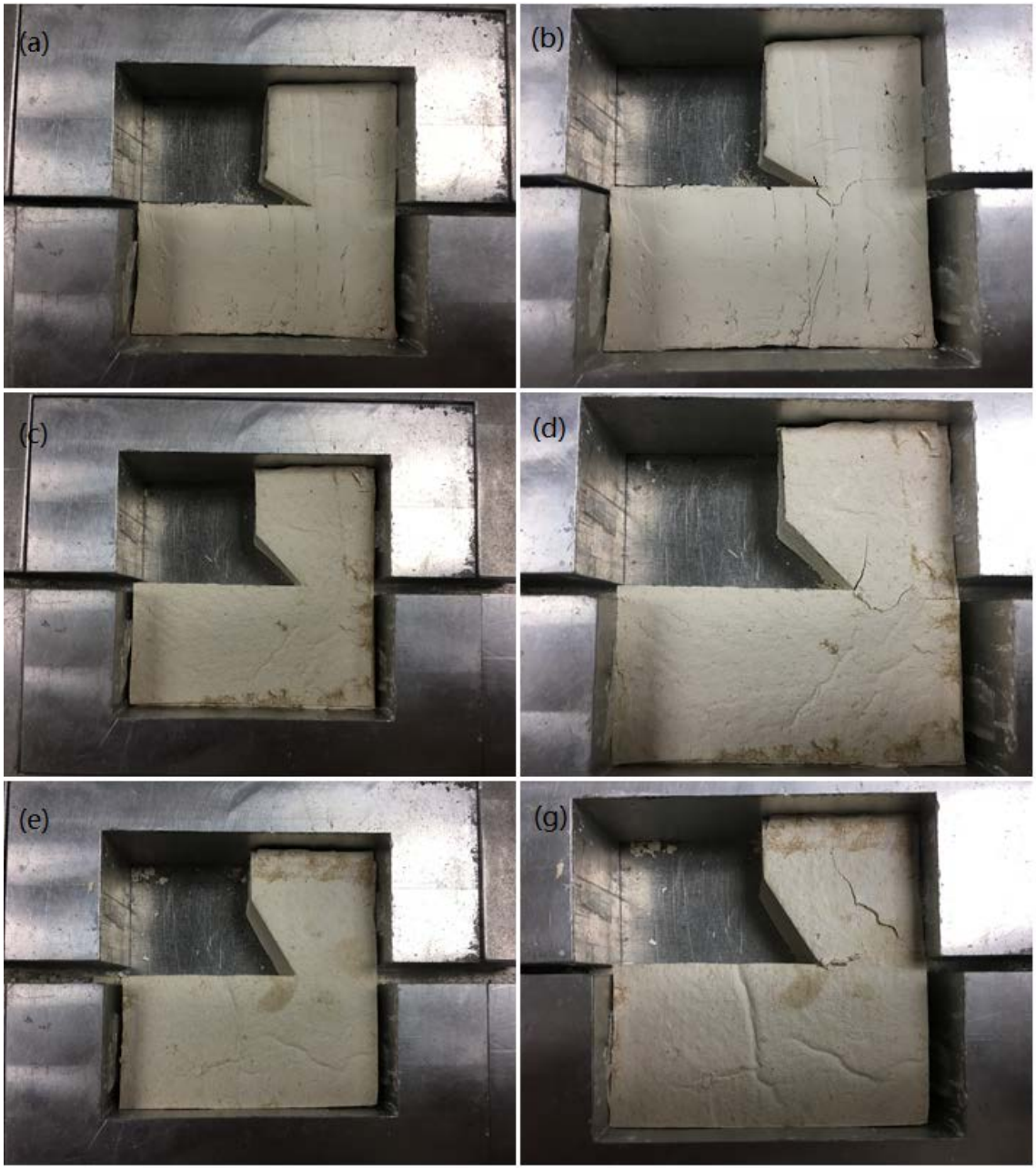

Figure 4.63 (a) the state of installation of notch of **30°**, (b) the state of failure of notch of **30°**, (c) the state of installation of notch of **45°**, (b) the state of failure of notch of **45°**, (e) the state of installation of notch of **60°**, and (f) the state of failure of notch of **60°**

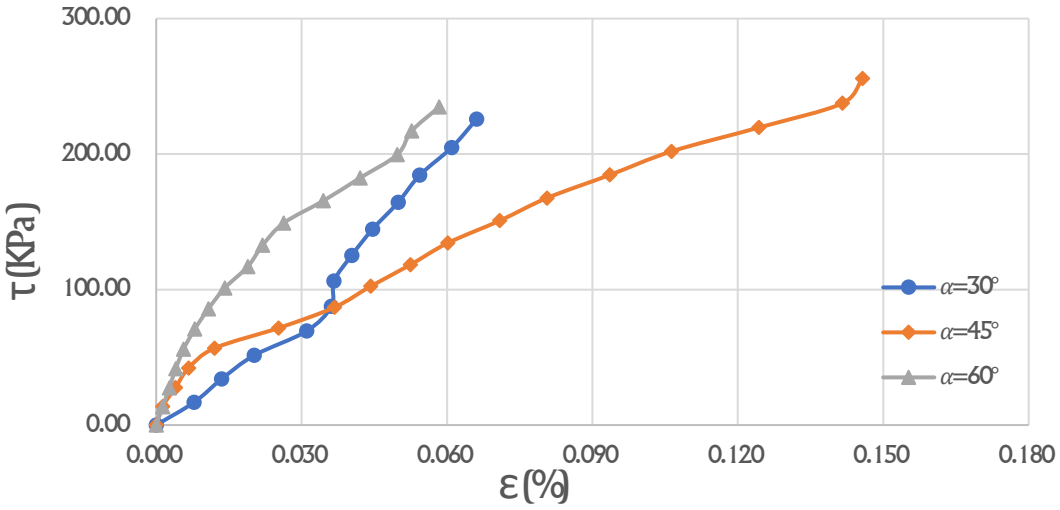

Figure 4.64 Stress-strain curve

In this figure, the τ_{max} of notch of 30°, 45° and 60° are 225.694KPa, 255.755Kpa and 234.694Kpa, respectively, the σ are 154.059KPa, 149.440Kpa and 156.256Kpa, respectively, and the final strains ε_f are 0.066%, 0.146%, 0.058%, respectively. These results show no obvious change in the trend of τ_{max} and ε_f. The sample with a notch of 30° had a crack in the toe that moved towards upper right with a crack angle α_{r1} of 116°. The sample with a notch of 45° had a crack in the toe that moved towards upper right with a crack angle α_{r2} of 81°. The sample with a notch of 60° had a crack in the toe with a crack angle α_{r3} of 72°. Based on these results, it can be concluded that the angle of the secondary crack developing from the toe of the notch decreases when the angle of the notch increases.

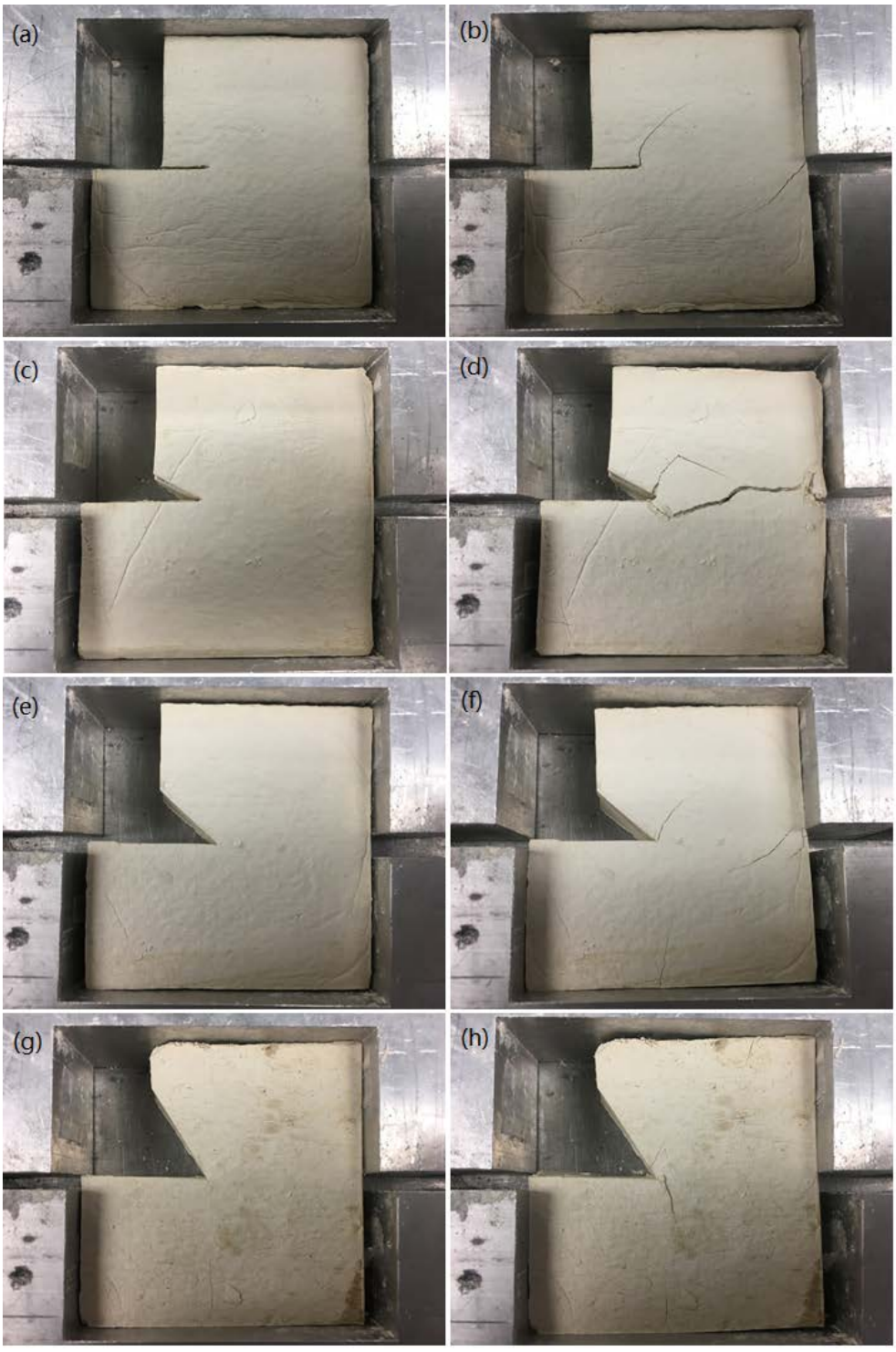

Figure 4.65 (a) the state of installation of notch of **0°**, (b) the state of failure of notch of **0°**, (c) the state of installation of notch of **30°**, (d) the state of failure of notch of **30°**, (e) the state of installation of notch of **45°**, (f) the state of failure of notch of **45°**, (g) the state of installation of notch of **60°**, and (h) the state of failure of notch of **60°**

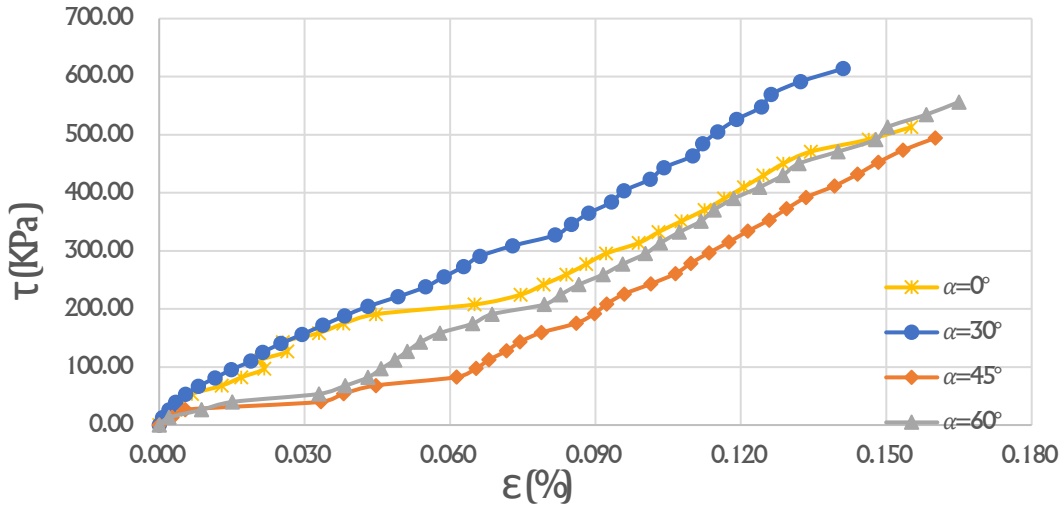

Figure 4.66 Stress-strain curve

In this figure, the τ_{max} of notch of 0°, 30°, 45° and 60° are 513.049Kpa, 613.806KPa, 494.299Kpa and 556.358Kpa, respectively, the σ are 81.654KPa, 79.901Kpa, 81.071Kpa and 78.128Kpa, respectively, and the final strains ε_f are 0.155%, 0.141%, 0.160%, 0.165%, respectively. These results show no obvious change of trend of τ_{max} and ε_f. The sample with a notch of 0° had a crack in the toe that moved towards upper right with a crack angle α_{r1} of 89°. The sample with a notch of 30° had a crack in the toe that moved towards upper right and a crack angle α_{r2} of 78°. The sample with a notch of 45° had a crack in the toe with a crack angle α_{r3} of 93°. The sample with a notch of 60° had a crack in the toe with a crack angle α_{r4} of 103°. This test shows that when the angle of the notch increases from 0° to 60°, the angle of the secondary crack increases.

4.2 COMPARING LABORATORY RESULTS WITH THEORETICAL RESULTS

According to the data that have been collected above, the initial angle, β, the original normal stress, σ_n, the original shear stress, τ, and the ratio between σ_n and τ, t, have been obtained. Therefore, the normal stress after transaction, σ_n', the shear stress after transaction, τ', the ration between σ_n' and τ', t', and the theoretical value of the angle of secondary crack propagation, α_t can be calculated by Eq.3.28, Eq.3.29 and Eq.3.30.

The graphs that shows the comparison between the angle of secondary crack propagation, α obtained in the test and the theoretical value, α_t are shown below.

The first group

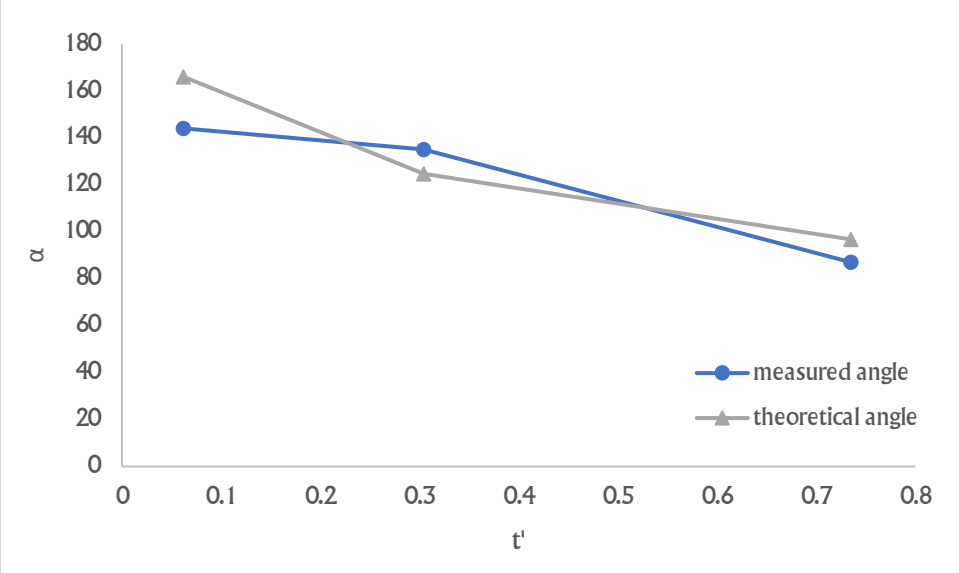

Figure 4.67 the relationship between t' and **α**

In this group, when the initial angle, β are 30°, 45°, 60°, respectively, the corresponding measured angle, α are 87°, 135°, 144°, respectively, and the corresponding theoretical angle, α_t are 97°, 125°, 166°, respectively.

The second group

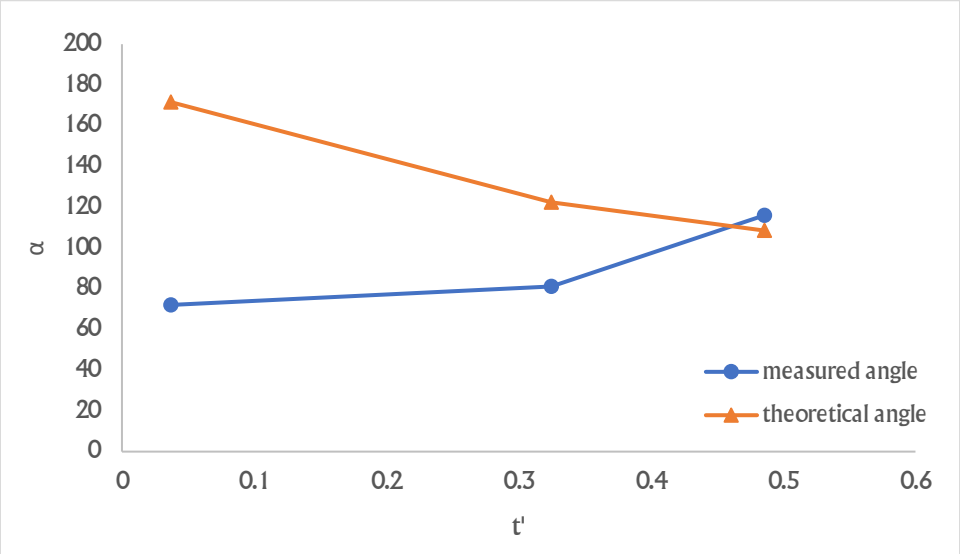

Figure 4.68 the relationship between t' and **α**

In this group, when the initial angle, β are 30°, 45°, 60°, respectively, the corresponding measured angle, α are 116°, 81°, 72°, respectively, and the corresponding theoretical angle, α_t are 109°, 122°, 171°, respectively.

The third group

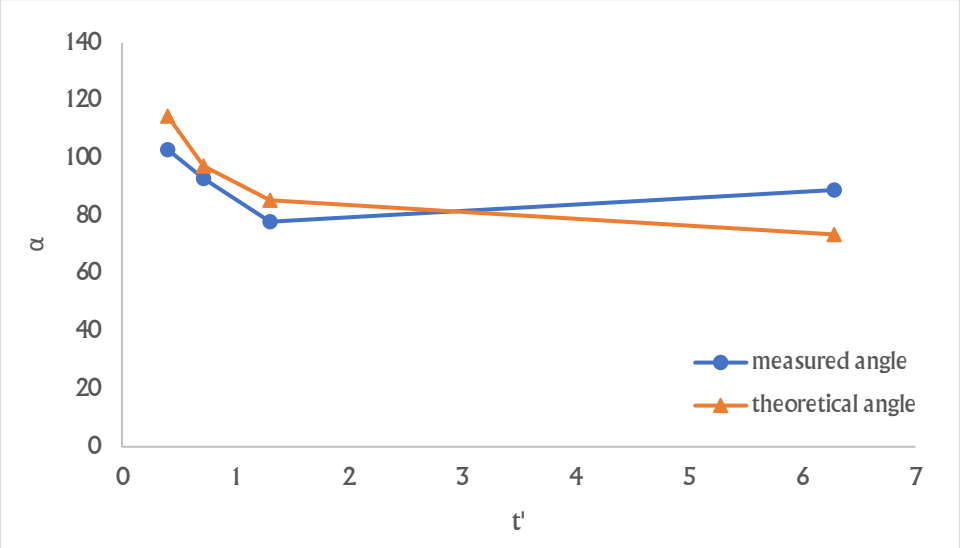

Figure 4.69 the relationship between t' and **α**

In this group, when the initial angle, β are 0°, 30°, 45°, 60°, respectively, the corresponding measured angle, α are 89°, 78°, 93°, 103°, respectively, and the corresponding theoretical angle, α_t are 74°, 85°, 97°, 115°, respectively.

For the tests above, the results of the first group and the third group are consistent with the theoretical solution and the result of the second group did not go well with the theoretical solution. This may be caused by the different water content, the ratio between the mass of water and the mass of clay. The average water content of each group is shown in Table.4.1 below.

Table 4.1 average water content of different groups

	first group(Fig.4.67)	second group(Fig.4.68)	third group(Fig.4.69)
average water content (%)	10.43	12.48	9.51

The result shown in Table.4.1 indicates the average water content of the three groups of samples with a toe crack, shown in Fig.4.67, 4.68, and 4.69, seems to influence the results. Fig4.67 and 4.69 show the results for samples that have similar low water content. The theoretical (elastic) and experimental results agree well. However, Fig.4.68 shows that the experimental result and theoretical (elastic) did not match well. The reason seems to be the higher water content of the samples (w=12.48%) that make the samples more plastic and not elastic as assumed by the theoretical analysis.

5.0 CONCLUSION

This study focus on the formation and propagation of secondary cracks from openings and notches in simulated slopes. To accomplish this, novel laboratory tests as well as Linear Elastic Fracture Mechanics theory are used. From the results, the following conclusions can be reached:

1. In Kaolinite clay samples with hollow opening, the shape of the opening significantly influences the maximum stress around the opening boundary. In uniaxial compression test, the sample is more sustainable when its ellipse is the same major axis but with a higher H/W; when H/W of the ellipse opening increases, the angle of the secondary crack decreases; when opening is circular, the secondary cracks developing from the opening tend to be parallel, but when the opening is triangular, the secondary cracks that develop tend to be symmetric. In direct shear test, the results also show that a sample can better withstand shear stress when the opening has a higher H/W and indicate the same secondary cracks development trend as in uniaxial compression test.

2. In Kaolinite clay samples with a notch, the initial angle of the notch has a significant influence in the direction of the secondary crack propagation. In the direct shear test, the sample shows that the initial angle of the notch has no obvious influence on the maximum stress around the tips. However, when the initial angle of the notch increases, the angle of the secondary crack increases as well.

3. The maximum tangential stress criterion from Linear Elastic Fracture Mechanics (LEFM) predicted the results very well. It explains the type of stress that caused the secondary crack propagation of the traditional problems as well as the extended situation. Furthermore, it predicts the direction of the secondary crack propagation under mixed-mode type of loading. This proves the usefulness of LEFM theory in solving geotechnical engineering problems.

4. In this study, the samples of the experiments are in a relatively small dimension and simple condition. In the future study, samples with mixed materials and larger dimension can be applied in the laboratory experiment.

5. The water content is main factor in laboratory experiment. However, in this paper it is not discussed comprehensively due to the limited number of samples. In the future study, the same model can be done with different of water content and then analyze in groups investigating if the maximum tangential stress criterion still apply when the water content is relatively high.

BIBLIOGRAPHY

[1] Eurosion, 2004. Living with coastal erosion in Europe: sediment and space for sustainability. Results from the Eurosion Study. 40 pages

[2] Castedo, R., Murphy, W., Lawrence, J., & Paredes, C. (2012). Geomorphology A new process – response coastal recession model of soft rock cliffs. Geomorphology, 177–178, 128–143. https://doi.org/10.1016/j.geomorph.2012.07.020

[3] Collins, B. D., & Sitar, N. (2008). Processes of coastal bluff erosion in weakly lithified sands, 97, 483–501. https://doi.org/10.1016/j.geomorph.2007.09.004

[4] Río, L. Del, & Gracia, F. J. (2009). Geomorphology Erosion risk assessment of active coastal cliffs in temperate environments. Geomorphology, 112(1–2), 82–95. https://doi.org/10.1016/j.geomorph.2009.05.009

[5] Brooks, S. M., Spencer, T., & Boreham, S. (2012). Geomorphology Deriving mechanisms and thresholds for cliff retreat in soft-rock cliffs under changing climates: Rapidly retreating cliffs of the Suffolk coast , UK. Geomorphology, 153–154, 48–60. https://doi.org/10.1016/j.geomorph.2012.02.007

[6] Castedo, R., Fernández, M., Trenhaile, A. S., & Paredes, C. (2013). Modeling cyclic recession of cohesive clay coasts : Effects of wave erosion and bluff stability. Marine Geology, 335, 162–176. https://doi.org/10.1016/j.margeo.2012.11.001

[7] Lutton, R. J. FRACTURES AND FAILURE MECHANICS IN LOESS AND APPLICATIONS TO ROCK MECHANICS. No. AEWES-RR-S-69-1. ARMY ENGINEER WATERWAYS EXPERIMENT STATION VICKSBURG MISS, 1969.

[8] Hutchinson, John Neville. *Cliffs and shores in cohesive materials: geotechnical and engineering geological aspects*. publisher not identified, 1986.

[9] Hutchinson, J. N. "General report: morphological and geotechnical parameters of landslides in relation to geology and hydrogeology: Proc 5th International Symposium on Landslides, Lausanne, 10–15 July 1988V1, P3–35. Publ Rotterdam: AA Balkema, 1988." *International Journal of Rock Mechanics and Mining Sciences & Geomechanics Abstracts*. Vol. 26. No. 2. Pergamon, 1989.

[10] Arnaldo, L., Camones, M., Vargas, A., Peluci, R., Figueiredo, D., & Quadros, R. (2013). Application of the discrete element method for modeling of rock crack propagation and coalescence in the step-path failure mechanism. Engineering Geology, 153, 80–94. https://doi.org/10.1016/j.enggeo.2012.11.013

[11] Jiang, M., Jiang, T., Crosta, G. B., Shi, Z., Chen, H., & Zhang, N. (2015). Modeling failure of jointed rock slope with two main joint sets using a novel DEM bond contact model. Engineering Geology, 193, 79–96. https://doi.org/10.1016/j.enggeo.2015.04.013

[12] Gu, D., & Huang, D. (2016). A complex rock topple-rock slide failure of an anaclinal rock slope in the Wu Gorge , Yangtze River , China. Engineering Geology, 208, 165–180. https://doi.org/10.1016/j.enggeo.2016.04.037

[13] Li, L. C., Tang, C. A., Zhu, W. C., & Liang, Z. Z. (2009). Computers and Geotechnics Numerical analysis of slope stability based on the gravity increase method. Computers and Geotechnics, 36(7), 1246–1258. https://doi.org/10.1016/j.compgeo.2009.06.004

[14] Zhang, K., Cao, P., & Meng, J. (2015). Modeling the Progressive Failure of Jointed Rock Slope Using Fracture Mechanics and the Strength Reduction Method, 771–785. https://doi.org/10.1007/s00603-014-0605-x

[15] Ke, C., Kuo, C., Hsu, S., Liu, S., & Chen, C. (2012). Two-Dimensional Fracture Mechanics Analysis Using a Single-Domain Boundary Element Method, 2012. https://doi.org/10.1155/2012/581493

[16] Mohr, T. (2005). Numerical analysis of a landslide in soils with strain-softening behaviour, (8), 585–596.

[17] Li, Y., Peng, J., Zhang, F., & Qiu, Z. (2016). Cracking behavior and mechanism of sandstone containing a pre-cut hole under combined static and dynamic loading. Engineering Geology, 213, 64–73. https://doi.org/10.1016/j.enggeo.2016.08.006

[18] Vallejo, Luis E. "The brittle and ductile behavior of a material containing a crack under mixed-mode loading." The 28th US Symposium on Rock Mechanics (USRMS). American Rock Mechanics Association, 1987.

[19] Vallejo, Luis E. "Application of fracture mechanics to soils: an overview." Fracture Mechanics Applied to Geotechnical Engineering: ASCE, 1994.

[20] Lisjak, A., Garitte, B., Grasselli, G., Müller, H. R., & Vietor, T. (2015). The excavation of a circular tunnel in a bedded argillaceous rock (Opalinus Clay): Short-term rock mass response and FDEM numerical analysis. Tunnelling and Underground Space Technology Incorporating Trenchless Technology Research, 45, 227–248. https://doi.org/10.1016/j.tust.2014.09.014

[21] Lisjak, A., Grasselli, G., & Vietor, T. (2014). International Journal of Rock Mechanics & Mining Sciences Continuum – discontinuum analysis of failure mechanisms around unsupported circular excavations in anisotropic clay shales. International Journal of Rock Mechanics and Mining Sciences, 65, 96–115. https://doi.org/10.1016/j.ijrmms.2013.10.006

[22] Labiouse, V., & Vietor, T. (2014). Laboratory and In Situ Simulation Tests of the Excavation Damaged Zone Around Galleries in Opalinus Clay, (123), 57–70. https://doi.org/10.1007/s00603-013-0389-4

[23] Vallejo, Luis E. "The Influence of Open and Closed Toe Notches on the Stability of Rock and Soil Slopes." Integrating Innovations of Rock Mechanics: Proceedings of the 8th South American Congress on Rock Mechanics, 15–18 November 2015, Buenos Aires, Argentina. IOS Press, 2015.

[24] Griffith, A. A. "The theory of rupture." Proceedings of the 1st Int. Congress on Applied Mechanics, Delft. 1924.

[25] Irwin, George R. "Analysis of stresses and strains near the end of a crack traversing a plate." Spie Milestone series MS 137.167-170 (1997): 16.

[26] Irwin, G. R., J. A. Kies, and H. L. Smith. "Fracture strengths relative to onset and arrest of crack propagation." Proc. ASTM. Vol. 58. 1958.

[27] Rice, James R. "A path independent integral and the approximate analysis of strain concentration by notches and cracks." ASME, 1968.

[28] Anderson, T. L. Fracture Mechanics -- Fundamentals and Applications. 2nd ed., Boca Raton CRC, 1994

[29] Mach, K. J., Nelson, D. V, & Denny, M. W. (2007). Techniques for predicting the lifetimes of wave-swept macroalgae : a primer on fracture mechanics and crack growth, 2213 – 2230. https://doi.org/10.1242/jeb.001560

[30] Kirsch, G. "Theory of Elasticity and Application in Strength of Materials." Z. des Ver. Dtsch. Ing 42.29 (1898): 797-807.

[31] Brown, Edwin T., and Barry HG Brady. Rock mechanics: for underground mining. George Allen, 1985.

[32] Poulos, Harry George, and Edward Hughesdon Davis. Elastic solutions for soil and rock mechanics. John Wiley, 1974.

[33] Jaeger, John Conrad, Neville GW Cook, and Robert Zimmerman. Fundamentals of rock mechanics. John Wiley & Sons, 2009.

[34] Heok, E., and J. W. Bray. "Rock slope engineering." The Institution of Mining and Metallurgy, London (1977): 127-149.

[35] Erdogan, Fazil, and G. C. Sih. "On the crack extension in plates under plane loading and transverse shear." Journal of basic engineering 85.4 (1963): 519-527.

[36] Vallejo, Luis E. "Application of fracture mechanics to soils: an overview." Fracture Mechanics Applied to Geotechnical Engineering:. ASCE, 1994.

[37] Ingraffea, Anthony R., and Francois E. Heuze. "Finite element models for rock fracture mechanics." International Journal for Numerical and Analytical Methods in Geomechanics 4.1 (1980): 25-43.

[38] Lisjak, A., Grasselli, G., & Vietor, T. (2014). International Journal of Rock Mechanics & Mining Sciences Continuum – discontinuum analysis of failure mechanisms around unsupported circular excavations in anisotropic clay shales. International Journal of Rock Mechanics and Mining Sciences, 65, 96–115. https://doi.org/10.1016/j.ijrmms.2013.10.006